COMPUTATIONAL AND EXPERIMENTAL STUDIES ON THE DAMAGE RESPONSE OF FERRITIC AND AUSTENITIC STEELS UNDER EXTREME CONDITIONS

By

Sarita

(Enrolment No. PHYS01201604002)

Bhabha Atomic Research Centre, Mumbai

A thesis submitted to the

Board of Studies in Physical Sciences
In partial fulfillment of requirements
for the Degree of

DOCTOR OF PHILOSOPHY

of

HOMI BHABHA NATIONAL INSTITUTE

December, 2020

Homi Bhabha National Institute

Recommendations of the Viva Voce Committee

As members of the Viva Voce Committee, we certify that we have read the dissertation prepared by *Sarita* entitled " *Computational and experimental studies on the damage response of ferritic and austenitic steels under extreme conditions* " and recommend that it may be accepted as fulfilling the thesis requirement for the award of Degree of Doctor of Philosophy.

Chairman – Prof. Raghvendra Tewari	**Date:** 14/04/21
Guide / Convener–Prof. Niharendu Choudhury	**Date:** Niharendu Choudhury 14/04/21
Co-guide - Prof. Aniruddha Biswas	**Date:** Aniruddha Biswas 14/4/21
Examiner - Prof. Aftab Alam	**Date: 14/04/21** Alam..
Member 1- Prof. Debasis Sen	**Date:** 14.04.2021 Debasis Sen
Member 2- Prof. Ashok Arya	**Date:** 14/04/2021
Member 3- Prof. Paramita Mukherjee	**Date:** 14/04/21 P. Mukherjee

Final approval and acceptance of this thesis is contingent upon the candidate's submission of the final copies of the thesis to HBNI.

I/We hereby certify that I/we have read this thesis prepared under my/our direction and recommend that it may be accepted as fulfilling the thesis requirement.

Date: 14/04/21

Place: Mumbai

Aniruddha Biswas

Signature
Co-guide (if any)

Niharendu Choudhury

Signature
Guide

STATEMENT BY AUTHOR

This dissertation has been submitted in partial fulfillment of requirements for an advanced degree at Homi Bhabha National Institute (HBNI) and is deposited in the Library to be made available to borrowers under rules of the HBNI.

Brief quotations from this dissertation are allowable without special permission, provided that accurate acknowledgement of source is made. Requests for permission for extended quotation from or reproduction of this manuscript in whole or in part may be granted by the Competent Authority of HBNI when in his or her judgment the proposed use of the material is in the interests of scholarship. In all other instances, however, permission must be obtained from the author.

Sarita.

Sarita

DECLARATION

I, hereby declare that the investigation presented in the thesis has been carried out by me. The work is original and has not been submitted earlier as a whole or in part for a degree / diploma at this or any other Institution / University.

Sarita.

Sarita

List of Publications arising from the thesis

Journal

1. "Revisiting temporal evolution of Cu-rich precipitates in Fe-Cu alloy: Correlative small angle neutron scattering and atom-probe tomography studies", ***Sarita Ahlawat*****,** S.K. Sarkar, D. Sen, and A. Biswas; *Microscopy and Microanalysis* ***2019****, (25), 840-848*

2. "First-Principle Investigations of Electronic Structures and Interactions of Foreign Interstitial Atoms (C, N, B, O)and Intrinsic Point Defects in Body- and Face-Centered Cubic Iron Lattice: A Comparative Analysis", ***Sarita Ahlawat*****,** K. Srinivasu, A. Biswas and N. Choudhury; *Computational Material Science* ***2019****, (170), 109167*

3. "Distortion energy-electronic energy compensation determines the nature of solute interactions with irradiation induced vacancies in ferritic steel", ***Sarita Ahlawat***, K. Srinivasu, A. Biswas and N. Choudhury; *Physical Chemistry Chemical Physics* ***2021,*** *(23), 8689-8704*

4. "Ion-induced structural transformation in SS316 austenitic stainless steel under heavy ion irradiations", ***Sarita Ahlawat***, Velaga Srihari, Nandini Garg, Debdulal Kabiraj, Manju Bala, Sonu Hooda, Niharendu Choudhury and Aniruddha Biswas; **Under review in** ***Journal of Material Science***

Conferences

1. "Heavy ion irradiation study in SS316", ***Sarita Ahlawat***, Velaga Srihari, Nandini Garg, Debdulal Kabiraj, Manju Bala, Sonu Hooda, Niharendu Choudhury and Aniruddha Biswas; presented at conference, "Advances in refractory and reactive metals and alloys", BARC, Mumbai (27-29 January, **2016**) (Poster presentation)

2. " Correlative SANS and APT study of Cu evolution in thermally aged binary Fe-Cu alloy", ***Sarita Ahlawat***, S.K. Sarkar, D. Sen, and A. Biswas; oral presentation at conference, "International Conference on Electron Microscopy and XXXV Annual Meeting of the Electron Microscope Society of India", Mahabalipuram (17-19 July, **2017**) (Oral presentation)

3. "SANS study in heavy ion irradiated SS316", ***Sarita Ahlawat***, Velaga Srihari, Nandini Garg, Debdulal Kabiraj, Manju Bala, Sonu Hooda, Niharendu Choudhury and Aniruddha Biswas; presented at conference, "Solid state physics symposium", BARC, Mumbai (26-30 December, **2017**) (Poster presentation)

4. "XRD study in heavy ion irradiated SS316", ***Sarita Ahlawat***, Velaga Srihari, Nandini Garg, Debdulal Kabiraj, Manju Bala, Sonu Hooda, Niharendu Choudhury and Aniruddha Biswas; presented at conference," National seminar on crystallography", BARC, Mumbai (19-22, June, **2019**) (Poster presentation)

5. "First principle calculation of point defect interaction in body- and face-centered cubic iron", ***Sarita Ahlawat***, K. Srinivasu, A. Biswas and N. Choudhury; presented at conference," Computational chemistry symposium", BARC, Mumbai (7-9, November, **2019**) (Poster presentation)

6. "Evolution of irradiation induced defects in heavy ion irradiated austenitic SS316 steel", ***Sarita Ahlawat***, Velaga Srihari, Nandini Garg, Debdulal Kabiraj, Manju Bala, Sonu Hooda, Niharendu Choudhury and Aniruddha Biswas; Oral presentation at conference, "12th Asia Pacific Microscopy conference ", Hyderabad (03-07 Feb., **2020**) (Oral presentation)

Sarita.

Sarita

Dedicated

To my family….

Acknowledgements

First and foremost, I would like to express my special thanks to my supervisors Dr. Niharendu Choudhury and Dr. Aniruddha Biswas for their sincere guidance, motivation, care, patience and continuous support during my Ph.D. work. I really enjoyed the research freedom under your guidance which helped me to learn the different aspects of research and this will definitely go beyond the academic work.

I would like to express my sincere gratitude to my doctoral committee members: Dr. Raghvendra Tewari, Dr. Debasis Sen, Dr. Paramita Mukherjee and Dr. Ashok Arya for their valuable inputs in improving the quality of my work. I express my heartfelt thanks to Dr. P.D. Babu for carrying out magnetization studies. Once again special thanks to Dr. Debasis Sen for his help in carrying out small angle scattering experiments and data analysis. I would like to acknowledge the use of super-computing facility at Bhabha Atomic Research Center, Mumbai, Pelletron facility at IUAC Delhi and APT facility in IISC Bangalore.

I have benefitted immensely from many fruitful discussions with my friends Rohini, Sudip, Deodatta, Meenu, Piyali, Shefali, Yogesh, Sukhdeep, Ritu, Rajni, Nisha, Rekha, Rajesh, Baltej, Channprit, Pushpa, Raman, Jyoti and others who directly or indirectly helped me achieving my goals. I would like to thank Santosh Ji and other workshop staff for their help during experimental work.

All of the above, I am extremely grateful to my family, who have been supportive of my carrier choices and have always encouraged me through tough time. Without their constant love, support and faith, this venture could not have been successful. Last but not least, I would like to express a sincere thanks to my husband Parveen who, always cheer me up and stands by me. He has been always a constant source of unconditional love, support and inspiration to me. Thank you for accompanying me in this wonderful journey.

Contents

List of Figures

Figure 4.6. Displays APT reconstructed iso-concentration surfaces of Cu in (a) as-solutionized (b) 1 h (c) 3 h (d) 5 h (e) 8 h (f) 25 h (g) 50 h (h) 100 h . Only Cu atoms are displayed here in blue color. The CRPs are delineated by 10 at. % Cu iso-concentration surfaces.

Figure 4.7. Displays APT reconstructed iso-concentration surfaces of Cu in as-solutionized, 5 h, 25 h. Only Cu atoms are displayed here in blue color. The CRPs are delineated by 10 at. % Cu iso-concentration surfaces. This depicts direct evidence of morphological transition from spherical to ellipsoid shape with aging.

Figure 4.8. Depicts temporal evolution of number density of precipitates from APT analysis. Temporal exponent of number density is given by slope of linear fit which is displayed in figure.

Figure 4.9. Depicts temporal evolution of equivalent spherical radius of precipitates from SANS analysis (spherical model and ellipsoid model) and APT analysis.

Figure 4.10. Variation of ratio between interfacial energy and strain energy with aging duration and inset shows the change in slope of interfacial to strain energy ratio.

Figure 5.1. **(a)** Initial configuration for migration of a SA (Cu/Ni atom) from its initial position (blue circle at the corner) to the nearest vacancy (shown as circle at the body center) and the migration path as shown by an arrow in bcc-Fe lattice. **(b)** Final configuration for the same migration **(c)** Migration energies for jump of a Cu and a Ni atom from the initial to final configuration as shown in **(a)** and **(b)** respectively.

Figure 5.2. Binding energies of SA-SA and V-SA pairs as a function of the distance in bcc-Fe (a) Cu-Cu and V-Cu (b) Ni-Ni and V-Ni (c) Cu-Ni (d) represents the different investigated configurations for the studied complex.

Figure 5.3. Schematic representation of the investigated configurations for V-X_n (X=Cu/Ni) clusters. (Here, gold color atoms are Fe atoms; red color atoms are solute atoms)

Figure 5.4. **(a)** Decomposition of total binding energy of V-Cu_n complex into distortion and electronic binding energy **(b)** Decomposition of electronic binding energy into the contributions of different bonds in V-Cu_n complex.

Figure 5.5. The differential charge density distribution (in eV/Å^3) for vacancy with solute atoms in V-Cu_n complex in bcc-Fe lattice. The charge distributions of Cu and their nearest neighbor Fe-atoms are shown here.

List of Tables

Chapter 8

Summary and Future Direction

In this dissertation work, the effect of temperature and irradiation on the microstructure and phase transformation of two important classes of nuclear structural materials is investigated using APT, SANS, XRD, magnetization measurements and first principle calculations. The materials under investigation include (i) binary model alloy for RPV steel (Fe-1.4 at.% Cu); and (ii) SS316 austenitic steel. Further, microstructural changes like solute segregation that are commonly encountered on exposure to high temperature and irradiation are governed largely by the solute interaction behaviour; hence it is important to understand the interaction among different solute atoms in steel. Therefore, first principle calculations are performed to study the fine interaction among the different solute atoms present in both ferritic and austenitic steels. The current thesis presents a combination of both these aspects namely, the microsturctural response under irradiation and temperature, fine interaction among solute atoms and radiation induced crystal structure transformation in steels. The principal results are summarized below.

8.1 Summary

(1) Temporal evolution of Cu-precipitates in binary Fe- 1.4 at.% Cu model alloy for RPV steel is studied using APT, SANS, Vickers micro-hardness and magnetization experiments. For this study, we have aged Fe- 1.4 at.% Cu alloy at 500^{o}C for different aging time up to 100h. The hardness increases with aging time till 8h and starts decreasing afterwards. Further, the effect of thermal aging on magnetization is also investigated and its behavior mimics the reciprocal behaviour of that of the micro-hardness. APT provides direct evidence of formation of Cu-rich

precipitates on thermal aging. Further, morphological transformation of Cu-rich precipitates from spherical to ellipsoid is also observed by APT, which is attributed to 9R-3R structural transformation. The definitive indication of this morphological transformation is also detected in SANS signal for the first time. The power law exponent of temporal evolution of precipitates size is in agreement with the standard Lifshitz-Slyzov-Wagner model. This temporal evolution implies that the system enters the coarsening regime after 8h of aging. This corroborates well with the observed evolution of micro-hardness and magnetization with aging. In addition, it is observed that Cu content within the Cu-rich precipitates increases with aging time. Further, the quantitative results from APT and SANS are in agreement with each other.

(2) Understanding the basic phenomena involved in the formation of Cu-rich precipitates in Fe-Cu model alloy for RPV steel, is of great interest. Therefore, the first principle calculations are utilized to investigate the interaction behavior of Cu atoms in bcc-Fe lattice and also to study the effect of the presence of Ni atoms on Cu precipitation. The formation enthalpy results suggested that both the solute atoms are energetically stable at substitutional position in bcc Fe-lattice. The interaction among Cu-Cu atoms is found to be attractive in nature, whereas it is repulsive in case of Ni-Ni atoms. Further, the fine interaction behavior of solute atoms with vacancies is also investigated and it is observed that presence of vacancies tends to bind Cu atoms strongly as compared to Ni atoms in bcc-Fe lattice. The origin of the interaction behaviour among vacancy and solute atom complexes is further explained in detail with the help of electronic structure and the distortion of crystalline lattice. Further, the migration energy barrier is calculated for both Cu and Ni atoms, and is found to be smaller for Cu atoms as compared to Ni atoms in bcc-Fe lattice. Interestingly, our migration energy results explained clearly the experimental evidence of core

shell precipitate formation of Cu and Ni in bcc-Fe. This study provides a good rationalization of the experimental results on solute (Cu/Ni) clustering behavior in irradiated RPV steels.

(3) The phase transformation behavior and microstructural evolution of SS316 austenitic steel irradiated using two different ions Ag and Au with three different fluencies ($1x10^{13}$, $5x10^{13}$ and $1x10^{14}$ ions/cm^2) are studied. Irradiation damage in terms of DPA is calculated using SRIM /TRIM software and it is observed that Au ions produce more damage than Ag ions. Reverse martensitic transformation is observed in case of both the ion irradiations, which is confirmed by XRD and magnetization measurements. Additionally, forward martensitic transformation is also observed, but only in case of Au ion irradiation of higher fluence. Nature of phase transformation is found to be dependent on the damage level as well as on the identity of the ions. Moreover, microstructural evolution in irradiated SS316 is studied using APT and SANS techniques. From scattering data, it is observed that the inhomogeneities present in the irradiated specimens are of nanometer length scale and their dimension increases with fluence.

(4) A detailed comparative analysis of point defect interaction with small solute atoms (C/N/B/O) in both bcc and fcc-Fe lattice is investigated utilizing first principle calculations. It is observed that B atom is energetically stable at substitutional position in bcc-Fe lattice and at octahedral interstitial position in fcc-Fe lattice, whereas all other solute atoms are stable at octahedral site in both Fe-lattices. The stability of all solute atoms is discussed from the perspective of their chemical nature as well as the geometrical factor. Further, the interaction behavior of B atom in two lattices is found to be completely different, whereas other solute atoms have similar behavior in both lattices. It is found that B atom tends to bind other solute atoms (SAs) in bcc-Fe lattice, whereas it repels in fcc-Fe lattice. Furthermore, strong resemblance is observed between B atom and vacancy regarding their nature of interaction with

other point defects in bcc-Fe lattice. The trapping ability of vacancy in bcc-Fe is found to be stronger than in fcc-Fe lattice. In case of two solute atoms interaction in presence of a vacancy, it is found that two C atoms form a covalent bond in bcc-Fe, but not in fcc-Fe. In this study we observed that in bcc-Fe, a vacancy can bind 3 to 4 SAs irrespective of their identity and in fcc-Fe system it can stabilize upto 2 to 5 SAs. Therefore, it is concluded that the introduction of a vacancy in bcc or fcc-Fe system stabilizes the configurations by relieving the excess strain of the matrix. The nature of bonding and charge delocalization has been analyzed in detail in all the cases using differential charge density plots.

8.2 Future Direction

Steels are most important structural materials for industrial applications. The present thesis has emphasized on the microstructural evolution and phase transformation in RPV steels and austenitic steel with effect of thermal aging and irradiation. In addition to the observed results in this thesis, possible future studies that can be of research interest are listed below:

- Intermediate morphological transformation of Cu-rich precipitates from spherical to ellipsoid is observed with effect of thermal aging. This study can be extended to investigate this intermediate morphology in detail with effect of thermal aging as well as irradiation.
- The effect of Ni on Cu precipitation is discussed using first principle calculations in this thesis. It is of interest to see the effect of other alloying elements like silicon/manganese along with Ni on Cu precipitation in order to obtain exact interaction behavior of RPV steel.

- The effect of incoming ion identity and damage level on phase transformation of ion irradiated steel, need further careful investigations.
- A comparative analysis of the irradiation induced point defect interaction with heavy elements present in both ferritic and austenitic steel may be explored using first principle calculations.

Abstract

Iron based alloys are most important structural materials for industrial applications. Both, ferritic and austenitic steels both are primarily used as structural materials for different components in nuclear reactors. Both these materials are subjected to high irradiation and high temperature during reactor operation. Consequently, the long term stability of these structural materials is a critical issue both for the present as well as future generations of nuclear reactors.

The present study focuses on investigating damages and microstructural changes produced in ferritic and austenitic steels induced by high temperature and irradiation. Since, proper understanding of radiation-induced microstructural evolution/changes requires coordinated experimental and theoretical studies, in the present work, we have utilized both experimental and theoretical techniques. In the present study, various characterization techniques such as atom probe tomography (APT), small angle neutron scattering (SANS), magnetization measurements, Vicker's hardness and x-ray diffraction (XRD) are used for the experimental investigations. Apart from that, the first principle density functional theory (DFT) calculations have also been used to understand atomistic and electronic origin of experimentally observed Cu precipitation in ferritic and austenitic steels.

The effect of thermal aging on Cu-rich precipitates (CRPs) in binary Fe- 1.4 at% Cu alloy, which is used as model alloy for RPV steel to understand the Cu precipitation behaviour, is investigated using correlative APT and SANS techniques. The APT analysis has not only shown that the CRPs have been formed in the irradiated steels, but also clearly revealed that the CRPs undergo morphological transformation from spherical to ellipsoid with a significant change in its aspect ratio as a function of aging time. The SANS analysis has successfully detected the signature of

this morphological transformation in the scattering data, something that has been accomplished for the first time. To understand the reason behind such precipitate or cluster formation by different solute atoms in the Fe-matrix, we have used first-principle DFT calculations. The attractive interactions in cases of Cu-Cu and V-Cu complexes, as predicted by the DFT calculations, are likely to be the main cause of formation of Cu-clusters in steel. It has also been demonstrated that the presence of a vacancy, which is produced in a large number in an irradiated sample, can increase the Cu-Cu attraction and therefore favors Cu cluster formation in steels. One of the novelties of this investigation lies in its analysis on the origin of the binding energy (BE) of vacancy-solute complexes by decomposing the BE into electronic and distortion energy contributions. Having studied Cu precipitation behavior in model RPV alloys both experimentally and theoretically, further investigations on the evolution of crystal structure and microstructure in heavy ion irradiated SS316 have also been reported in the present thesis. Both, the damage level as well as the identity of ions are found to affect the nature of radiation-induced phase transformation in this steel. Apart from heavy atoms likes Cu, Ni, Cr, Mn etc., smaller atoms like B, C, N and O are also present in the steel either as additives or as impurities and their interaction with radiation-induced defects may also lead to structural degradation of the steels. In order to gain fundamental knowledge about a solute interaction with vacancy (V) and another solute atom (SA) and related electronic structure aspects, first-principle DFT calculations have been used. The distance dependent BE of all SA-SA and V-SA combinations along with differential charge densities and density of states depict repulsive interactions except for B atoms in bcc-Fe systems, whereas all these interactions are repulsive in fcc-Fe systems. It is also shown that the “solute atom trapping” ability of a vacancy in a bcc-Fe system is stronger than that in a fcc-Fe system.

Chapter 1

Introduction

1.1 Background

At present, India has 22 nuclear reactors in operation with a total installed capacity of 6780 MW. These include different types of reactors namely, two Boiling Water Reactors (BWR), eighteen Pressurized Heavy Water Reactors (PHWR) and two Pressurized Water Reactors (VVER). The operating conditions of reactors include high temperature range (200-400^{o}C) and high irradiation dose (can reach ~50dpa). Moreover, the proposed generation IV reactors need to operate at even harsher conditions of still higher temperatures (500-1000^{o}C) and higher level of irradiation doses (~100dpa) [1-7]. Therefore, it is challenging to choose appropriate material for different structural components of nuclear reactors that need to withstand these harsh conditions during its life time of the order of 25-30 years. A comparison of the operating conditions for proposed generation IV reactors like Very High Temperature Reactor (VHTR), Gas Fast Reactor (GFR), Super Critical Water Reactor (SCWR), Molten Salt Reactor (MSR), Lead Fast Reactor (LFR), Sodium Fast Reactor (SFR) and fusion reactors [7] is shown in Figure 1.1. High energy neutrons present inside the reactors interact with the structural materials used in the core components of the reactors, and create atomistic defects like vacancies, interstitials and their complexes. Moreover, these point defects often undergo complex interactions leading to significant microstructural changes by forming various structural defects like voids [8], helium bubbles [9], clusters and/or precipitates [10], and segregation of impurity/alloying elements to high energy sites such as grain boundaries, dislocations etc. [11]. Further, quite similar effects on materials microstructure have also been observed as a result of exposure to high temperature.

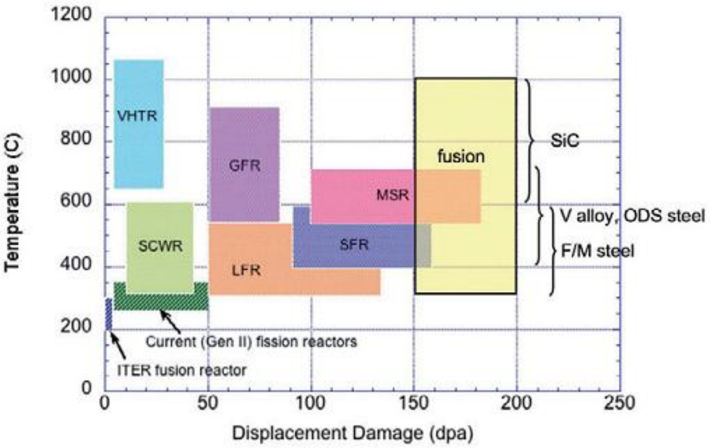

Figure 1.1 depicts the overview of temperature and irradiation doses regimes for structural materials in current reactors (gen II), proposed reactors (gen IV) and fusion reactors [7].

It is well established that the mechanical properties of a material is directly correlated with its microstructure. Therefore, microstructural changes induced by irradiation or high temperature may lead to degradation of macroscopic properties of the structural materials like hardening, increase in ductile to brittle transition temperature, decrease in fracture toughness etc [12] and thus limits the lifetime of reactor. As a result, radiation damage has been a subject of intensive research during the past decades [11]. The effect of radiation damage on materials can be studied using experimental techniques as well as simulation methods. The experimental studies of irradiated materials are often expensive and time consuming. Furthermore, it is difficult to obtain an unambiguous understanding of the radiation-induced microstructural evolution phenomena only with experiments. On the other hand, empirical interaction potential based computer simulations have been extensively used to investigate the radiation damage behaviour in materials in recent years, since irradiation conditions (e.g. temperature, irradiation imparted energy) can be easily controlled during simulation studies. In fact, computer simulations complement the experiments in generating some phenomenological models that can explicitly explain the materials behaviour as a function of radiation dose, temperature etc. However, accuracy of the computer simulation results heavily depends on the chosen interaction potential or force-field. A better understanding of the interactions among the constituent elements in a material, specifically when the material is metallic in nature, can be achieved through quantum mechanical electronic structure calculations. However, there is a caveat that wave function based quantum mechanical calculations require significant computational time, and at times, depending on the system size, computational time may become prohibitively high. However, computational demand associated with density based density functional theory (DFT) based electronic structure calculation is comparatively less and can be used successfully to problems relating to periodic solids very easily. Therefore, experimental methods in conjugation with DFT based electronic structure calculations can be easily used for proper understanding of the radiation-induced microstructural evolution processes.

1.2 Motivation

The long-term stability of nuclear structural materials is the key component for safe operation and life time management of a nuclear power plant. Therefore, understanding the effect of irradiation and temperature on nuclear structural materials is crucial for variety of technological applications. A diverse range of structural materials are used for different components in nuclear reactors as shown in Figure 1.2 [7]. It can be seen from Figure 1.2 that steel is widely used structural material in core components of nuclear reactor. These materials are selected based on the properties such as mechanical strength, ductility, stability, neutron absorbing characteristics etc. With effect of radiation damage, these materials can also undergo microstructural changes that can degrade the mechanical properties such as [13]: (i) low temperature hardening due to formation of dislocation loops, precipitates and cavities; (ii) loss of toughness; (iii) loss of ductility; (iv) radiation-induced creep etc. Therefore, from the application point of view, investigations pertaining to the effect of irradiation and temperature on microstructural properties of steels are of utmost importance.

In this thesis, our interest is mainly confined to the investigation of temperature- and radiation-induced microstructural evolution of ferritic steel and austenitic steel out of the available variety of structural materials. We have utilized both experimental and theoretical methods to get a clear understanding of the fundamental mechanisms involved during microstructural changes in these materials.

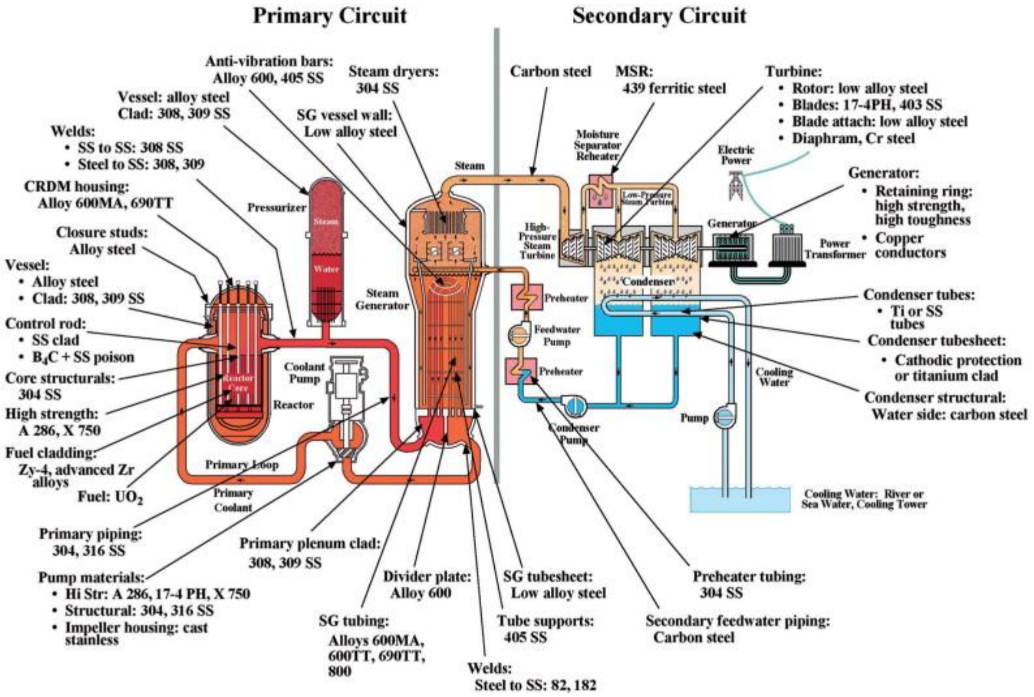

Figure 1.2 Schematic representation of different components utilizing various structural materials in pressurized water reactor [7].

1.3 Objective of this research

The work described in the present thesis deals with understanding the fundamental origin of microstructural changes relating to damages in ferritic and austenitic steels induced by high temperature and irradiation. Since, proper understanding of radiation-induced microstructural evolution/changes requires coordinated effort using experimental and theoretical methods, the results presented in this thesis are obtained by utilizing both experimental and theoretical techniques. The objectives of the present thesis are as follows:

- Understanding the temporal evolution of Cu-precipitates in Fe- 1.4 at% Cu model alloy to simulate the same phenomena in RPV steel and its correlation with alloy strength using state-of-the art experimental techniques.

- Exploring the microscopic origin of Cu-precipitates formation in the Fe-Cu model alloy, which represents RPV steel, by using first-principle density functional theory based calculations. The effect of the presence of Ni-atoms on Cu precipitation behaviour in this model alloy has also been examined.

- Investigating the effect of heavy ion irradiation on phase transformation and microstructural evolution in SS316 austenitic stainless steel using various experimental techniques.

- Studying the interactions of point defects with small solute atoms (C, N, B, O) in both bcc and fcc iron lattices using first-principle density functional theory based calculations.

1.4 Layout of the thesis

The thesis is organized into eight chapters. An overall introduction to the subject along with the motivation behind the work has been already discussed in **chapter 1**. This section discusses major results of each chapter in the thesis. The structure of the thesis is as follows:

Chapter 2 presents a detailed review of the literature related to the thesis work. The discussion begins with the fundamental phenomena related to radiation damage in materials, followed by explanation of Norgett, Robinson and Torrens (NRT) formula and estimation of extent of damage in terms of displacement per atom (DPA). This is followed by the brief descriptions of different radiation-induced microstructural changes in steels. Further, literature on Fe-Cu alloy is discussed mentioning the history of this alloy, crystal structure of the Cu precipitates, precipitate morphology, precipitate kinetics, and already available results from first-principle density functional theory (DFT) calculations on the Fe-Cu alloys. This chapter also includes history, radiation-induced phase transformation and microstructural evolution in SS316 austenitic steel along with the related discussion on the first-principle DFT calculations.

Chapter 3 elaborates the experimental techniques that have been employed for sample preparation and sample characterization, along with the details about the simulation methods. This chapter is divided into two parts. The first part of this chapter discusses about the experimental techniques, and it starts with alloy preparation methods and heat treatments. The experimental methodologies for atom probe tomography (APT) technique and small angle scattering are discussed in detail. The Vicker's micro-hardness measurement, utilized to study the mechanical properties of the binary Fe-Cu model alloy, is also discussed. Experimental X-ray diffraction (XRD) technique, which is used to study the structural characterization of the samples, is described next. The second part of this chapter discusses electronic structure calculation methods with the related discussions on Schrodinger equation, Hohenberg-Kohn theorems with proofs and the Kohn Sham DFT approach.

Next four chapters that constitute the body of the thesis represent detailed accounts of experimental as well as computational works in regard to Fe-Cu binary alloy (model alloy for RPV steel) and austenitic steel.

Chapter 4 describes the effect of thermal aging on Cu-rich precipitation (CRPs) in binary Fe-1.4 at% Cu alloy which is used as a model alloy for RPV steel. A correlative small angle neutron scattering (SANS) and atom probe tomography (APT) study of temporal evolution of CRPs is presented here. APT analysis has clearly shown that the CRPs undergo morphological transformation from spherical to ellipsoid with a significant change in the aspect ratio, an effect known to be associated with the 9R-3R structural transition of the precipitates [14]. The SANS analysis could successfully detect the signature of this morphological transformation in the scattering data, something that has been accomplished for the first time. The characteristics of the precipitates, such as, the size and the number density are determined using both APT and SANS techniques and the results obtained from these two experimental techniques are in very good agreement with each other. The power law exponents of temporal evolution of the size and the number density of the precipitates obtained from the present study closely follow Lifshitz-Slyzov-Wagner model.

In order to understand the microscopic and electronic origin of CRPs formation in bcc-Fe system, first-principle DFT calculations have been used and the results are described in detail in **Chapter 5.** The results relating to interaction behaviour of the solute atoms (Cu, Ni) with radiation-induced point defects (vacancies and di-vacancies) in bcc-Fe system are presented. The attractive interactions in cases of Cu-Cu and V-Cu complexes, as predicted by the DFT calculations, are likely to be the main cause for the formation of Cu-clusters in steel. One of the novelties of this investigation is the analysis of the origin of the binding energy (BE) in vacancy-solute complexes by decomposing the BE into electronic and distortion energy contributions. It is observed that a fine balance between these two often opposing energy contributions determines the vacancy-solute complex stability. We have observed that the BE of different sized stable clusters of Cu_n-Ni_m (for *n* and *m* upto 5) are attractive in nature, which implies that the formation of Cu_n-Ni_m clusters are energetically favorable. On the other hand, the calculated lower migration barrier for the diffusion of Cu atoms as compared to that of Ni atoms in the bcc-Fe lattice suggests sluggish Ni diffusion than Cu diffusion, the fact, which may help to explain the experimental observation of formation of CRPs surrounded by Ni atoms in the irradiated RPV steel. Further, our results indicate that the presence of both mono- and di-vacancies induces attraction, and hence accelerates aggregation of solute atoms in the Fe lattice. Therefore, presence of radiation-induced defects enhances the aggregation propensity of Cu/Ni solute atoms in bcc-Fe lattice.

In **Chapter 6,** the evolution of crystal structure and microstructure in heavy ion irradiated SS316 steel is presented. Two different ions Ag and Au are used for irradiation with three different fluences and the damage produced by Au ions is found to be higher than that by Ag ions. Phase transformation behaviour under irradiation is studied using XRD and magnetization measurements. The XRD study showed that the martensite phase fraction decreases with fluence as compared to the as-received sample in case of Ag ion irradiation. This implies the existence of reverse martensitic transformation (MT) under Ag ion irradiation. For Au ion irradiation, at lower fluence, the martensite phase fraction decreases as compared to the as-received sample, indicating the presence of reverse MT here as well. Afterwards, martensite phase fraction is found to increase with fluence, which unambiguously implies forward MT. Interestingly, the magnetization variations for Ag and Au follow exactly the same trend as a function of fluence as the one followed by their respective martensite phase fractions. Both, the damage level as well as the identity of ions are found to affect the nature of radiation-induced phase transformation in this steel. Further, APT and SANS techniques are utilized to study the radiation-induced microstructural evolution. SANS analysis has detected nanometric scatterer in the irradiated samples that are likely to correspond to the radiation-induced defects. Their dimensions increase with increasing fluence.

Although interactions among heavier elements like Cu and Ni in presence and/or absence of vacancies in bcc-Fe lattice have been studied in detail and presented in Chapter 5**,** understanding the interactions among smaller elements like B, C, N and O is also of utmost importance in gauging the structural integrity of steels. Therefore, **Chapter 7** of the thesis presents the comprehensive set of first-principle DFT calculation results for different complexes formed by small solute atoms (SA) e.g. C, N, B and O in bcc- and fcc-Fe lattices. A systematic comparison is established among the four solutes by investigating Fe-SA, SA-SA and V-SA interactions in both Fe-lattices. We have found that the energetically favourable configurational site for B atom is substitutional site in bcc-Fe lattice, while it is octahedral interstitial site in the fcc-Fe. This leads to the diverse interaction behaviour of B atom with point defects in both Fe-lattices. In order to characterize the interaction among point defects, we have calculated the distance dependent BE of all solutes with vacancies and with one another SA. Our calculations have showed the repulsive interaction between all solutes in bcc-Fe except the B atom, while in fcc-Fe, all four solute atoms indicate repulsion among each other. The energetically stable B atom is observed to bind the interstitial point defects strongly in bcc-Fe lattice, while it is not the case in fcc-Fe lattice. Furthermore, strong resemblance is observed between B atom and vacancy regarding their nature of interaction with other point defects in bcc-Fe lattice. In contrast, the interaction behaviour is completely different in these two Fe lattice. It is also observed that vacancy always exhibits a strong attraction with all four solutes in both Fe-lattices. Although vacancy always exhibits strong attraction with SA in both the Fe-lattices, the trapping ability of the vacancy in bcc-Fe is found to be stronger than that in fcc-Fe. Further insights into electronic structure and interaction of the point defects in the two Fe lattices have been obtained from the density of states and differential charge density calculations.

Chapter 8 is the concluding chapter of the thesis. Here all the results are summarized and future outlook of the work is suggested. This thesis reports the results of the effect of high temperature and irradiation on the damage response of ferritic and austenitic steels, respectively. A combined approach of experimental techniques and quantum mechanical calculations has been adopted for investigating the microstructural evolution, which shows CRPs formation in RPV steel, the origin of CRPs using DFT calculations, martensitic and reverse martensitic phase transformations in austenitic steel and its microstructure evolution under heavy ions irradiation. Further study on microstructural evolution and other damage related properties in austenitic steels under Ag and Au ion irradiations and theoretical studies to gain deeper insight into the attractive BE in various V-Cu_n and V-Ni_n clusters by decomposing it into electronic and strain contributions are underway. The future outlook of the work is also discussed here.

References

[1] V. Bhatnagar, M. Deffrennes, M. Hugon, P. Manolatos, K. Ptackova, G. Van Goethem, and S. Webster, Nuclear Engineering and Design **241**, 3376 (2011).

[2] E. E. Bloom, S. J. Zinkle, and F. W. Wiffen, Journal of Nuclear Materials **329-333**, 12 (2004).

[3] C. Fazio, A. Alamo, A. Almazouzi, S. De Grandis, D. Gomez-Briceno, J. Henry, L. Malerba, and M. Rieth, Journal of Nuclear Materials **392**, 316 (2009).

[4] C. Fazio, D. G. Briceno, M. Rieth, A. Gessi, J. Henry, and L. Malerba, Nuclear Engineering and Design **241**, 3514 (2011).

[5] K. L. Murty and I. Charit, Journal of Nuclear Materials **383**, 189 (2008).

[6] P. Yvon and F. Carré, Journal of Nuclear Materials **385**, 217 (2009).

[7] S. J. Zinkle and J. T. Busby, Materials Today **12**, 12 (2009).

[8] E. A. Little, Journal of Nuclear Materials **87**, 11 (1979).

[9] P. D. Edmondson, C. M. Parish, Y. Zhang, A. Hallén, and M. K. Miller, Journal of Nuclear Materials **434**, 210 (2013).

[10] P. R. Okamoto, S. D. Harkness, and J. J. Laidler, Trans Amer Nucl Soc, 70 (1973).

[11] G. S. Was, (Springer, 2007).

[12] R. J. Kurtz *et al.*, Journal of Nuclear Materials **386-388**, 411 (2009).

[13] G. R. Odette, M. J. Alinger, and B. D. Wirth, Annual Review of Materials Research **38**, 471 (2008).

[14] P. Othen, M. Jenkins, and G. Smith, Philosophical Magazine A **70**, 1 (1994).

Chapter 2

Literature survey

2.1 Irradiation damage in materials

Irradiation damage involves the transfer of energy from the incident energetic particles, such as electron, neutron and ions to the target material, and resultant redistribution of the target atoms [1-2]. Target atoms suffer displacement from their lattice site, resulting in formation of interstitials and vacancies in the target lattice [1]. The displacement of atoms is associated with both elastic and inelastic interactions of the incident particle with the target material [3]. The extent of generated defects are dependent on the type and energy of the incoming particle [4]. It is well known that the irradiation by both heavy ions and neutron can generate cascade in the material whereas electron radiation generates point defects only [1,4]. Therefore, heavy ions are better equipped than electrons to emulate neutron damage in the materials. The radiation damage event is typically composed of the following distinct processes [1]

1. The interaction of energetic incoming particle with the target lattice atom
2. The primary knock on atom (PKA) is generated when the energy transfer from the incoming particle to the target atom is more than its displacement energy
3. Target lattice atom is displaced from its lattice site
4. This displaced atom further creates more knock on atoms while passing through the lattice and generates displacement cascade

The basic defects generated during irradiation damage are point defects [1]. Several types of point defects generated during irradiation are classified as vacancy, interstitial and substitutional.

Most of the generated point defects recombine and annihilate each other. Further, subsequent events involve the migration and agglomeration of these point defects that lead to the formation of volumetric defects like voids and cavities. It is worthwhile to note that the entire radiation damage event occurs in a very short period of time of about 10^{-11} sec.

The radiation damage in material is expressed in units of displacement per atom (DPA) that primarily depends on the total number of atomic displacements occurring in the material [5-8]. This unit has been established as a fundamental measure of the level of irradiation exposure in materials. To estimate DPA, Norgett, Robinson and Torrens (NRT) [9-10] developed one of the most widely used models, which is a modified version of the existing Kinchin-Peace model [11]. NRT model accounts for both elastic collision and electronic stopping power, and is generally accepted as the international standard for quantifying DPA in irradiated materials. According to Kinchin-Pease model, the number of displaced atoms (N_d) by PKA with an energy T is given as [1,9,11]:

$$N_d = \left\{ \begin{array}{cc} 0 & for\ T < E_d \\ 1 & for\ E_d < T < 2E_d \\ \dfrac{T}{2E_d} & for\ T > 2E_d \end{array} \right\}$$

Here E_d is the displacement threshold energy which is the minimum energy required to displace a lattice atom. The functional dependence of the displaced atom on PKA energy is shown in Figure 2.2. The threshold energy for iron (Fe) is around 40 eV [12].

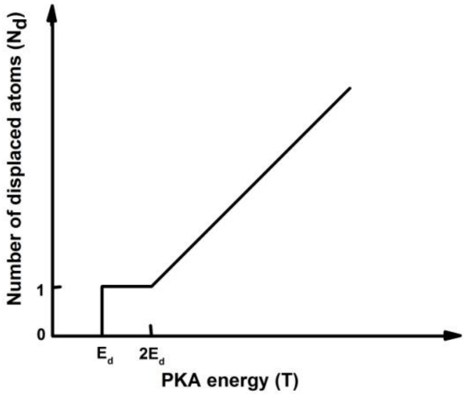

Figure 2.2 Represents the number of displaced atom as a function of PKA energy according to Kinchin-Pease model [1].

The average number of displacements produced by the incident ion can be calculated by using the displacement threshold energy value as an input in SRIM/TRIM program [13] , which in turn is used to determine the radiation damage in terms of DPA. SRIM/TRIM simulation program [13] is the most commonly used for calculating the range and stopping power of ions in solids. Here SRIM stands for Stopping and Range of Ions in Matter and TRIM stands for Transport of Ions in Matter. This program is mainly based on Monte Carlo simulation method namely, the binary collision approximation (BCA) code [14]. The detailed fundamental physics of this software is described in reference [14]. SRIM has some disadvantages like inability to account for the sample temperature and surface topography. An additional drawback is its inability to account for both the elastic and the inelastic collisions in the same run. However, in spite of these drawbacks, it remains the most accurate and efficient method for evaluating the behaviour of the incident ions in solids.

The radiation damage in terms of DPA can be estimated using the NRT formula, which is given as:

$dpa = \frac{0.8}{2E_d} * \left(\frac{dE}{dX}\right)_n * 10^8 * \frac{\varphi}{N}$ ………….. (2.1)

Here, E_d is threshold displacement energy; φ is fluence in ion/cm^2; N is atomic number density of target (atoms/cm^3); $\left(\frac{dE}{dX}\right)_n$ is linear energy transfer to the target material in nuclear process obtained from SRIM software.

2.2 Radiation-induced microstructure

Microstructural evolution as a consequence of radiation-induced damage in materials is investigated extensively over the years and a significant knowledgebase is available in the literature. The damage in the microstructure depends on the material as well as the irradiation conditions. The population of the microstructural defects is strongly dependent on the energy and the type of the incident particle, irradiation temperature, and accumulated doses. The typical radiation-induced microstructural damages in austenitic steel [15-22] and reactor pressure vessel (RPV) steel [23-28] are black dots, frank loops, cavities (bubbles/voids) and solute segregation or precipitation as shown in Figure 2.4. Radiation-induced formation of metal carbides is also reported. The nature of radiation-induced segregation and clustering/precipitation[1] depends entirely on the material composition and the irradiation environment. The work reported in this thesis is mainly confined to the detailed study of solute-matrix interaction and solute segregation in Fe-1.4%Cu alloy (model alloy for RPV steel) and SS316 austenitic steel.

---

[1] 'Cluster' is a small aggregation of solutes without any definite crystal structure, precipitate is large enough to have its own crystal structure.

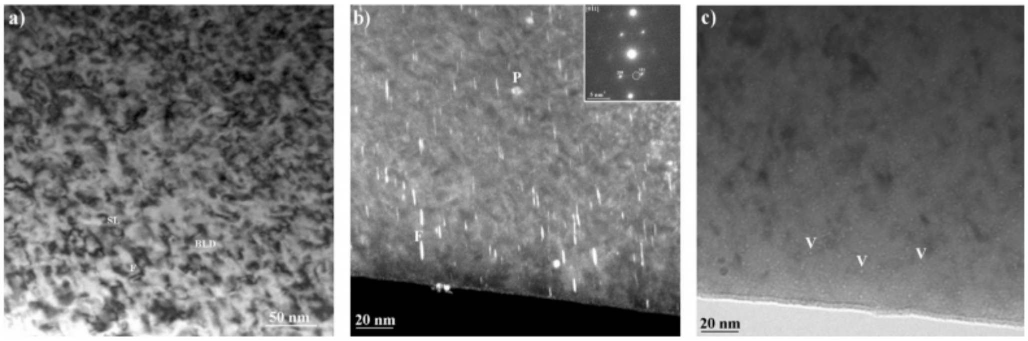

Figure 2.4 (a) Bright field image of SS316 containing black dots (BLD), frank loops (F) and small dots (SL). (b) Relrod image of frank loops (F) and Ni_3Si precipitates (P). (c) Out of focus image to visualize cavities (V). [29]

2.3 Previous work on binary Fe-Cu model alloy for RPV steel

2.3.1 History

2.3.1.1 Irradiation damage in RPV steel

Reactor Pressure Vessel (RPV) is the most important structural part of a PWR-type nuclear reactor as discussed in chapter 1. On irradiation, two different kinds of nano-meter sized solute clusters, Cu-rich and NiMnSi-rich, are observed in RPV steel, depending on the composition of the welds [30-35]. Cu-rich clusters also contain elements like Ni, Mn and Si, but in much smaller amount as compared to NiMnSi-rich clusters. The composition of these clusters is dependent primarily on the composition of the weld, e.g., NiMnSi-rich clusters are usually detected in case of low-Cu welds (<0.1%) [36], whereas Cu-rich clusters are observed in case of high-Cu welds. Both types of clusters are found to nucleate at dislocations as well as in the dislocation-free regions of the matrix [37-39]. In general, these radiation-induced solute clusters are way too small in size and devoid of any crystal structure [40].

In irradiated RPV steel, the formation of both Cu-rich [41-47] and NiMnSi-rich [30,45,48-49] clusters are studied extensively. In late 1960s, a relatively high Cu content (upto 0.4 wt%) in the RPV steel recorded many cases of significant deterioration of the mechanical properties and exposed the elevated risk of embrittlement of RPV steels under neutron irradiation [50]. It was found out to be due to the formation of Cu-rich clusters during irradiation [51-54]. After obtaining this insight, it became a usual practice to use RPV steel welds containing very low Cu content. However, the formation of Cu-rich clusters in RPV steels is reported at typical operating temperature of 290^{o}C even in case of Cu content as low as ~ 0.05-0.09 wt%. [46,55]. It is further observed that the Cu-rich clusters continue to form until 0.05 wt% Cu is left in the matrix [56]. In addition, it is reported that the presence of Cu-rich clusters accelerates the formation of NiMnSi-rich clusters in irradiated RPV steel [57-58]. Interestingly, Cu-rich clusters are also reported to form core-shell structure with Cu atoms in the core, encompassed by the shell of Ni and Mn atoms [48,59-60]. Therefore, Cu-rich clusters continue to remain critically important and relevant for the RPV steel.

2.3.1.2 Thermal aging of RPV steel

Thermal aging can also cause embrittlement of RPV steels. In fact, the formation of Cu-rich clusters in RPV steel is observed with both in case of thermal aging as well as under irradiation. The formation of Cu-rich clusters occurs primarily because of the limited solubility of Cu in bcc Fe at lower temperature [45,61]. It can be seen from the binary Fe-Cu phase diagram (Figure 2.5) that the maximum solubility limit of Cu in bcc-Fe is 1.9 wt% at around 850^{o}C and it becomes much smaller at lower temperature. Therefore, the supersaturated solid solution leads to the formation of Cu-rich clusters in RPV steel at the reactor operating temperature. Thermally aged RPV steel is well known to contain larger precipitates that have definite crystal structures [62], therefore from now onwards we will use the term precipitates instead of clusters in case of the thermally aged samples.

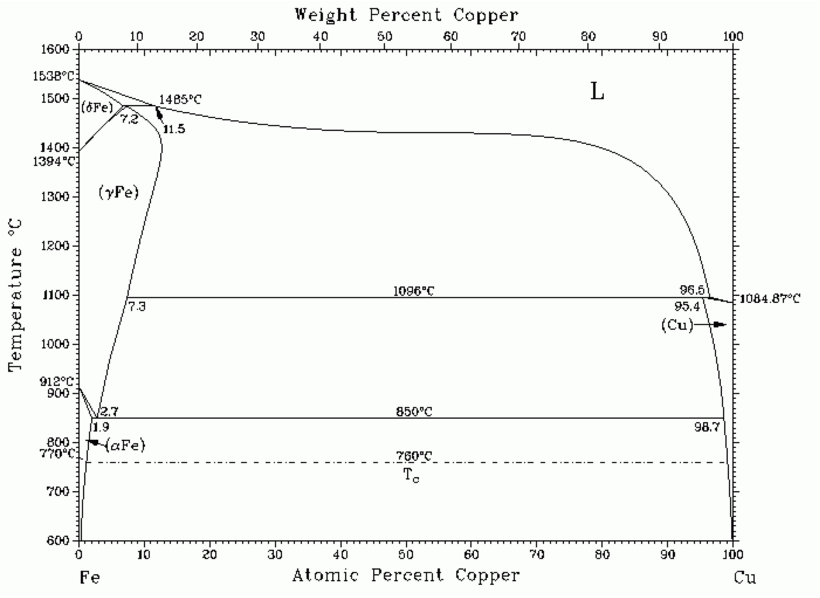

Figure 2.5 Binary Fe-Cu phase diagram [63].

2.3.1.2 Fe-Cu alloy

In order to fully understand the nature of the defects and get a better insight, less complex model alloys are frequently utilized in simulating the radiation-induced defects that are commonly encountered in the RPV steels of. Amongst the commonly available model alloys, Fe-Cu binary alloys are popularly used to simulate the formation of radiation-induced Cu-rich precipitates (CRPs) in RPV steels [64-67]. Several different methods can be employed to generate the ultrafine CRPs in both Fe-Cu model alloys and RPV steels [68-70]. Thermal aging is the one of the simpler methods to obtain CRPs in Fe-Cu alloy [71], which utilizes the negligible solubility of Cu in Fe at low temperature (0.03% at. at 773K [72]). As a result, CRPs in thermally aged Fe-Cu model alloy have been investigated extensively, both experimentally [68,71] and theoretically [73-74]. Different aspects of this precipitation process have been examined by researchers using various experimental techniques such as field ion microscopy (FIM) ([71,75]), atom probe tomography (APT) ([33,70,76-78]), high resolution transmission electron microscopy (HRTEM) ([79-80]), magnetization measurements ([81-83]), vicker's hardness measurement ([68,84]), and small angle neutron scattering (SANS) ([68,79]).

The literature regarding the crystal structure, morphology, kinetics and first principle calculations of the CRPs is briefly reviewed in the subsequent sections.

2.3.2 Precipitate crystal structure

A variety of techniques, such as, transmission electron microscopy (TEM) [80,85], x-ray diffraction (XRD) [86] and extended x-ray absorption fine-structure (EXAFS) [86-87] have been used to study the crystal structure of CRPs. These studies have confirmed that initially the CRPs are much smaller in size, have body-centre cubic (bcc) crystal structure and are coherent with the matrix. They eventually grow to larger size, transform to face-centre cubic (fcc) structure and turn incoherent. An EXAFS study in thermally aged Fe-1.3 wt% Cu and Fe-1.28wt% Cu-1.43wt% Ni alloys by Pizzini *et al.* [87] provided the first direct experimental evidence of CRPs having bcc structure during the early stages of precipitation. However, in the very first report [62] on CRPs in Fe-Cu alloy, this early stage was not detected by electron diffraction studies. This is due to the fact that the coherent CRPs have very similar lattice parameter as that of the matrix. The author reported that the CRPs become fcc after aging for 24 h at 700^{o}C and also noted that the close packed direction of bcc-Fe matrix and fcc-Cu precipitates is parallel i.e. $[111]_{bcc-Fe} \,||\, [110]_{fcc-Cu}$. The CRPs reportedly maintain Kurdjumov-Sachs orientation relationship with the Fe-matrix [62]. Othen *et al.* [80,85] have studied the structural transformation of CRPs in thermally aged Fe-1.3wt% Cu and Fe-1.28wt%Cu-1.43wt% Ni alloys at 550^{o}C using HRTEM. The authors reported that the CRPs did not undergo direct bcc to fcc transformation in these alloys. They followed a rather complex transformation sequence, i.e., bcc to twinned 9R to twinned 3R to fcc with increasing precipitate size. An EXAFS investigation [67] also provided the evidence of 9R structure in binary Fe-Cu, ternary Fe-Cu-Ni and Fe-Cu-Mn alloys. Further, more recent HRTEM investigation [88], EXAFS investigation [86], molecular dynamics simulations [89] and atomistic simulations [73,90] have also provided evidence of these intermediate structural transformations that the CRPs undergo before finally turning into fcc from its original bcc structure.

2.3.3 Precipitate morphology

The precipitate morphology has been studied mainly using APT and TEM. Early work by Hornbogen *et al.* [62] investigated the effect of aging temperature on the formation of CRPs in Fe-1.08 at% Cu binary alloy using TEM. The author reported the smallest CRPs with diameter 9 nm after 15 min of aging at 600^{o}C and also noted that their size increased with aging time. Further, the morphological transformation of CRPs from spherical to rod-like was also observed after 24h of aging at 700^{o}C presumably associated with the reduction in strain energy. Speich and Oriani *et al.* [91] also confirmed the presence of rod-shaped CRPs with major dimension around 500nm that were aligned to bcc-Fe matrix according to Kurdjumov-Sachs orientation relationship in Fe-Cu alloy using TEM. Kolli *et al.* [70] studied the precipitation in thermally aged high strength low-carbon Fe-Cu based steel using APT. The authors reported that the precipitates were spherical for smaller aging time and became rod-like after aging for 1024h at 500^{o}C (Figure 2.6(a-c)). Interestingly, the authors noted, that the precipitate having rod-like morphology contained mostly Cu atoms in the core and were partially surrounded by Ni, Mn and Al atoms. Monzen *et al.* [92] also reported rod-like morphology of CRPs in Fe-1.5wt% Cu thermally aged for 120h at 700°C. A few other researchers also reported the rod-like morphology of CRPs and Kurdjumov-Sachs orientation relationship [66,92-93].

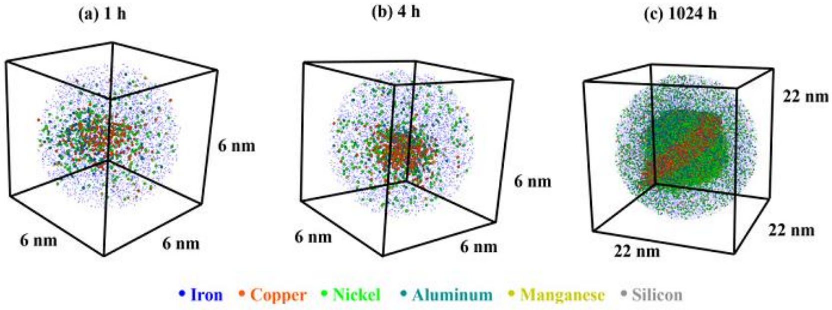

Figure 2.6 APT reconstruction of precipitates due to thermal aging for (a) 1h (b) 4h (c) 1024h [70].

An additional intermediate morphological transformation from spherical to ellipsoidal shape was first reported by Othen *et al.* [85] who showed that the 9R-3R structural transition was responsible for this intermediate morphological change and it occurred when the precipitates grew larger than 17 nm in diameter. Osamura *et al.* [94] also reported presence of ellipsoid precipitates of 26 nm equivalent spherical diameter in Fe-1.41 at% Cu-0.27 at% Ni-0.25 at% Mn quaternary alloy after aging for 30h at 823K (Figure 2.8). A more recent study by Kolli *et al.* [95] where presence of ellipsoid CRPs was noticed in Fe-Cu based steel, appears to be the only other report.

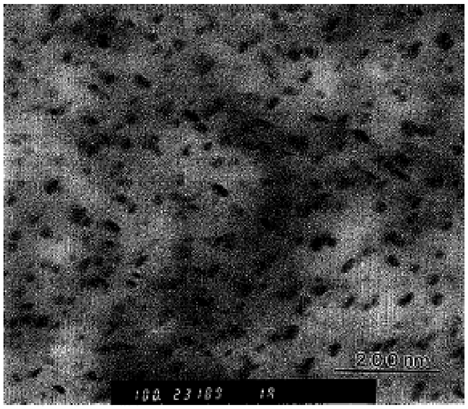

Figure 2.8 TEM micrograph of specimen aged at 823K for 30h showing ellipsoidal CRPs [94].

2.3.4 Precipitate Kinetics

The nucleation, growth and coarsening of CRPs are investigated earlier in a few reports [70,91-93]. Goodman *et al.* [71] reported that the precipitates' critical nucleus had a diameter of 0.66nm that contained only 13 atoms in Fe-1.4 at% Cu binary alloy. More recent study by Nagano *et al.* [96] found the critical radius between 0.3nm to 0.35nm for Fe-1.5 at% Cu alloy, which is similar to earlier results obtained by Goodman *et al.* [71]. Further, first principle calculation by Seko *et al.* [97] have reported the critical number of atoms equal to 13 in binary Fe-Cu with pure Cu core assumption. The study of Osamura *et al.* [94] observed that the addition of Ni and Mn elements enhanced the precipitation kinetics as compared to binary Fe-Cu alloy. This observation is consistent with a few other studies [97-98] as well.

Oriani *et al.* [91] studied the coarsening of precipitates in Fe-Cu binary alloys thermally aged at different temperatures and reported that the mean radius obeyed $t^{1/3}$ power law, which is consistent with the prediction of Lifshitz-Slyzov-Wagner (LSW) model [99] for coarsening. A Monte Carlo simulation study by Soisson *et al.* [100] on Fe-1.34 at% Cu binary alloy aged at 300°C and 500°C also reported $t^{1/3}$ dependence for mean radius. Further, a study by Monzen *et al.* [92-93] observed the mean radius power law of $t^{1/3}$ for thermally aged Fe-1.5 wt% Cu binary alloy at different temperatures 600°C and 700°C. Recent investigations by Kolli *et al.* [70] presented the temporal evolution of mean radius and number density of precipitates in thermally aged low-carbon Fe-Cu based steel at 500°C. The authors reported that initially the temporal dependency of radius was $t^{0.16}$ for aging time 1 to 64h and became $t^{0.34}$ for 64 to 1024h of aging, which implies that system enters coarsening region after 64h of aging. Further, the temporal dependence of the number density $t^{-0.63}$ in coarsening region is also reported by Kolli *et al.* [70], which is not consistent with the coarsening model power law exponent prediction (-1) [101] and indicates slower rate of coarsening in the system [70].

2.3.5. First principle calculation

It is well known that the radiation-induced point defects in steel matrix ultimately lead to increase in the diffusion of solute atoms (e.g. Cu and Ni) by an order of magnitude [102]. Further, the physical phenomena like diffusion, precipitation etc. in the material during irradiation is generally known to be controlled by interaction strength among radiation-induced point defects and solute atoms. Unfortunately, the experimental data [103-104] on these fine interactions among the point defects are scarce, as they are difficult to obtain experimentally, except for those obtained using thermodynamic models. However, with the advent of supercomputing facilities with more and more computational power over the last decade, these issues have attracted attentions of computational researchers and efforts have been made to understand the rationale behind solute clustering or segregation using complementary computational techniques such as Density Functional Theory (DFT) and other electronic structure calculation methods. Recently, the DFT calculation, because of its lower computational cost, has been extensively used to get insight into such fine interactions of different elements with various point defects such as interstitials and vacancies [105-107] from the electronic and atomic points of view.

The interactions between different solute atoms (Cu/Ni) and point defects in bcc-Fe lattice have been studied using DFT in recent years [108-113]. Domain *et al.* [109] performed the detailed study of interaction among vacancy and Cu atoms in bcc-Fe, but limited their study to Cu atoms only. Further, Vincent *et al.* [108] reported the positive binding energy (indicating attractive interaction) in case of Cu-Cu interactions and also demonstrated that the diffusion of Cu and Ni via vacancy mechanism was more efficient. The previous studies did not explore the origin of these interactions and also limited their binding energy investigation up to 4 nearest neighbors only. Medvedeva *et al.* [112] performed the interaction among Cu-Cu and Cu-Co complexes in bcc-Fe lattice and reported that the Co segregation slowed down the growth of Cu precipitates. In addition, Song *et al.* [113] reported that the formation of Cu precipitation was possible only from lattice with Fe spin polarization but not without spin polarization.

2.4 Previous work on SS316 as nuclear structural material

2.4.1 History

Austenitic stainless steel (ASS) has an attractive combination of good corrosion resistance and excellent mechanical properties and is widely used as structural materials in nuclear reactors [114-116]. In particular, ASS is mainly used in internal structure of pressurized water reactor (PWR). As the internal structure is located close to the reactor core, it is exposed to high neutron dose. Such exposure to high radiation dose results in deterioration of mechanical properties of materials and thus, limits the service conditions and lifetime of the components [117-118]. It is well established that microstructural response of ASS is strongly dependent on the irradiation environment [119-122]. In fact, degradation of property ASS such as hardening [123-124], loss of corrosion resistance [125] and cracking of the bolts of internal structure [126], are directly connected to the radiation-induced changes in the microstructures of ASS. Harries *et al.* [127] presented a comprehensive review of the irradiation effects on mechanical properties of SS316. The authors demonstrated that the effect of neutron irradiation on the mechanical properties of ASS can be directly correlated with the radiation-induced microstructure. Therefore, it is important to investigate ASS microstructure.

Earlier studies have shown that neutron irradiation in ASS causes adverse microstructural changes like formation of voids [128-129], interstitial dislocation loop [130-131], Ni_3Si phase [19-20], precipitates or solute clusters [132-133], carbides [134], and also changes in the crystal structure [135]. Further, Bruemmer *et al.* [136] have shown that the types of radiation-induced defects produced in ASS are primarily dependent on the operating temperature and irradiation doses in reactor (shown in Figure 2.10). Many researchers have explored the response of SS316 at low as well as at high irradiation doses [122,128,136-137]. Radiation-induced phase stability is also an important point of concern in nuclear structural materials and it is already established that radiation can have significant effect on the crystal structure of ASS [138-139].

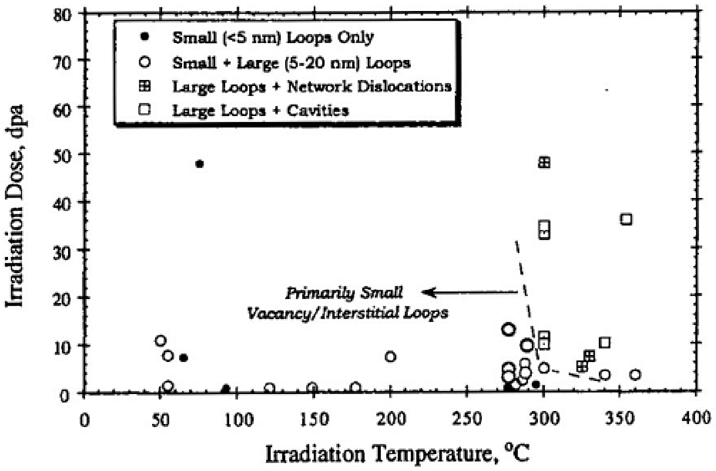

Figure 2.10 Schematic representation of the neutron radiation-induced defects in the ASS as a function of temperature and irradiation dose [136].

In 1960s and 1970s, heavy ion irradiation became quite popular for simulating the neutron irradiation damage [140-141]. One of the reasons is the ease involved in handling of the ion irradiated samples as compared to its neutron irradiated counterparts. In order to understand the basic phenomenon behind the damage process, it requires studies involving wide range of conditions, which is not feasible with neutron irradiation experiments. However, ion irradiation allows the variation in radiation parameters easily. Therefore, in the last few years, irradiation with different ions has been extensively used to understand the fundamental processes of microstructural evolution and structural transformation under irradiation in SS316 [138-139,142-145].

Over the years, various experimental techniques such as atom probe tomography (APT) [146-147], high resolution transmission electron microscopy (HRTEM) [143,147], nano-indentation measurement [143], magnetization measurements [144-145], x-ray diffraction (XRD) [144-145,148], grazing incidence x-ray diffraction (GIXRD) [138,149] and atomic force microscopy (AFM) [138] have been utilized to investigate radiation damage in ASS. The literature regarding radiation-induced microstructure and crystal structure transformation in ASS is briefly reviewed in the following subsections.

2.4.2 Radiation-induced microstructural evolution

Techniques like APT [116,147,150] and TEM [143,146] have been used widely to investigate radiation-induced microstructure in ASS. According to earlier reports, features evolved in microstructure during irradiation are interstitial dislocation loops [151], voids [129,152], precipitates or clusters [153], Ni_3Si phase [19-20] and carbides [154]. Radiguet *et al.* [146] investigated the effect of 160KeV Fe ion irradiation on SS316 microstructure using APT. The authors observed the radiation-induced Cr depletion and Ni, Si segregation at grain boundaries in irradiated SS316. This change in the chemical composition of grain boundary under the effect of irradiation is consistent with a few other reports as well [155-156].

A study by Etienne *et al.* [147] used laser-assisted APT and reported Frank loops, cavities and precipitates in SS316 under neutron irradiation of an estimated dose of 12dpa . The authors noted the presence of Ni-Si rich clusters (Figure 2.12) with the sgregation of P and Mo at the interfaces of these precipitates. Further, Toyama *et al.* [114] also observed the Ni-Si rich clusters in neuton irradiated ASS at a dose of 24dpa at 300°C. The presence of radiation-induced Ni-Si rich clusters in ASS is consistent with many other reports [29,116].

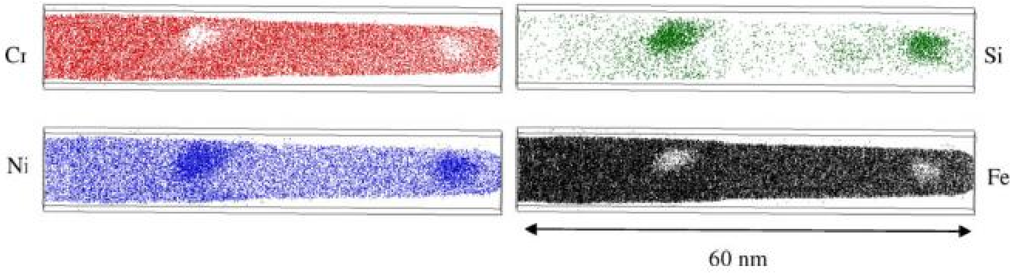

Figure 2.12 Atom map presenting Ni-Si rich clusters in neutron irradiated SS316 [147].

2.4.3 Radiation-induced crystal structural transformation

Radiation-induced structural transformation in ASS was extensively studied using XRD [144-145,148], GIXRD [138,149] and magnetization measurements [144-145]. Hayashi *et al* [139] reported partial transformation of austenite to martensite in SS316 under 40 KeV He ion irradiation utilizing conversion electron Mossbauer spectroscopy. The amount of austenite was found to decrease with increasing He irradiation dose, indicating occurrence of forward martensitic transformation (i.e. austenite to martensite transformation). Recent study by Dudognon *et al.* [138] investigated the effect of Cr, Ar, N, Xe, Mo, Ag and Pb ions irradiation in SS316. The authors observed lattice expansion, structural transformation and amorphization in ASS with increase in radiation damage as shown in Figure 2.13(a). The authors also reported that the structural transformation depended only on the damage level, irrespective of the identity of the ions. Forward martensitic transformation in ASS was also observed by Wang *et al.* [157] by TEM in case of 3MeV gold ion irradiation. A more recent study by Morozov *et al.* [144] also reported the forward martensitic transformation on attainment of deuterium concentration (C=0.5). Further, Huang *et al.* [143] studied the effect of xenon ion irradiation on structural transformation of SS316 and reported lattice expansion with increase in dpa as shown in Figure 2.13(b).

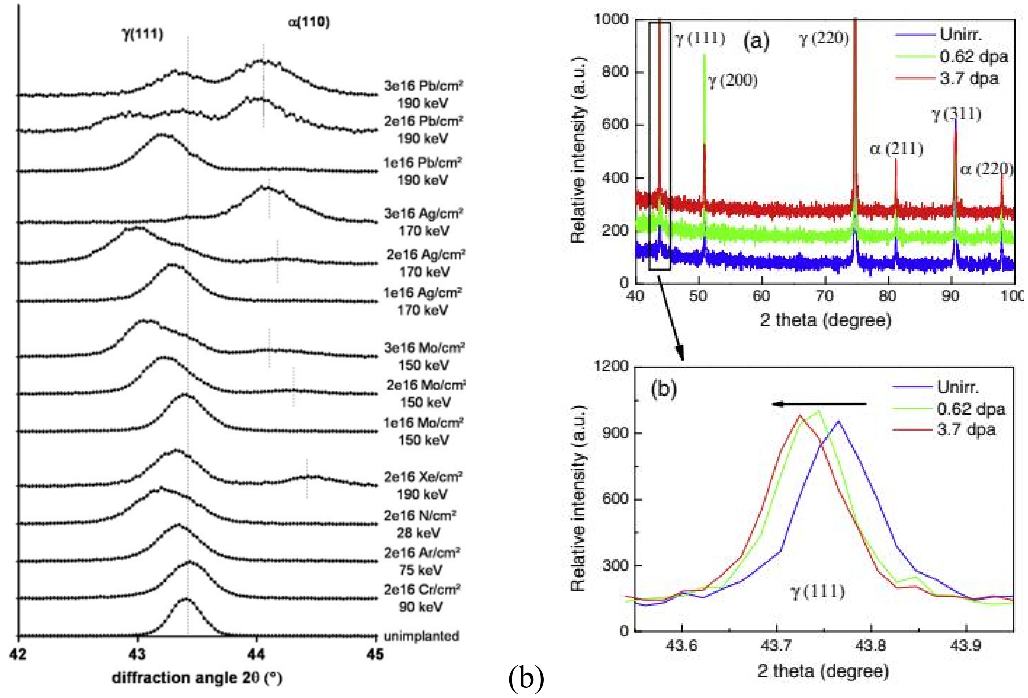

(a) (b)

Figure 2.13 (a) XRD plots for un-irradiated and irradiated samples with different ions and fluencies showing martensitic transformation [138]. (b) XRD pattern of SS316 before and after irradiation showing lattice expansion with increase in damage [143].

It is quite clear that the forward martensitic transformation in ASS under irradiation is well recognized in the literature, whereas, there is only one report of radiation-induced reverse martensitic transformation (martensite to austenite transformation) in ASS is available in the lireature, which is by Vardiman *et al.* [158]. They have studied the effect of Ni, N and Ne ion implantation in SS304, which contained stress induced martensite in the as-received condition. They reported that the martensite present in SS304 transformed to austenite by implantation of austenite stabilizing elements i.e. Ni and N ions, whereas Ne implantation had no effects. It is also noted that this structural transformation is confined to the ion implanted layer only. At this juncture, it is important to emphasize that the type of radiation-induced structural transformation in ASS is highly dependent on the irradiation conditions.

2.5 First principle calculations of small solute atom interaction in ferritic and austenitic steel

Steels are multi-component alloys that combine iron and carbon along with other light and heavy elements. The light elements like carbon (C), nitrogen (N), boron (B) and oxygen (O) are commonly present in steels either as impurities or as alloying elements. The presence of tiny amounts of these light elements as solute species in steels has a huge impact on the microstructure and the mechanical properties of steel. In both ferritic and austenitic steels, neutron irradiation not only produces point defects such as vacancies and interstitials but also enhances their diffusion. It is well known that the diffusion of vacancies leads to vacancy clusters and also promote the vacancy mediated diffusion of foreign interstitial atoms (FIAs), which we refer to here simply as solute atoms (SAs). This phenomenon leads to the precipitation of SAs, which in turn is responsible for the drastic alteration of mechanical properties of material. The precipitation process is generally known to be controlled by the solute-solute and solute-vacancy interaction strength. Therefore, the investigation of interaction among SAs and point defects in bcc-Fe as well as in fcc-Fe is necessary for the systematic analysis of structure and formation kinetics of the various point defects, which can transform into the precipitates of metastable or stable phases in the matrix.

DFT calculations are used to study the basic atomic phenomena involved in the fine interaction of light elements with various other defects such as interstitials, vacancies, dislocations and grain boundaries [105-106,159-162]. A large number of studies have been devoted to understand these interactions in Fe-based materials using DFT calculations [105-106,111,163-171] in recent years. There have been several works focusing on the interaction between elements such as carbon (C) [105-106,164,172], nitrogen (N) [105-106,164], oxygen (O) [164,170,173], boron (B) [163,174-176] and hydrogen (H) [177-180] in bcc-Fe matrix. According to the previous studies, C, N and O are energetically more stable at the octahedral interstitial sites in bcc-Fe whereas there are controversies over the stable position of B in this lattice. In bcc-Fe, B is identified as substitutional solute with small energy difference to the octahedral interstitial site in the study of Fors *et al.* [174] and it is confirmed by DFT study of Baik *et al.* [175] as well. However, He *et al.* [165] reported stable site for B as octahedral interstitial site in both bcc-Fe and fcc-Fe lattices. Domain *et al.* [105] have performed a detailed study of C and N interaction with vacancies, but their investigations were limited to bcc-Fe. Further, Ohnuma *et al.* [106] carried out the DFT calculations for interaction between vacancy-solute complexes in bcc-Fe and reported that VC_3 and VN_2 are most stable complexes.

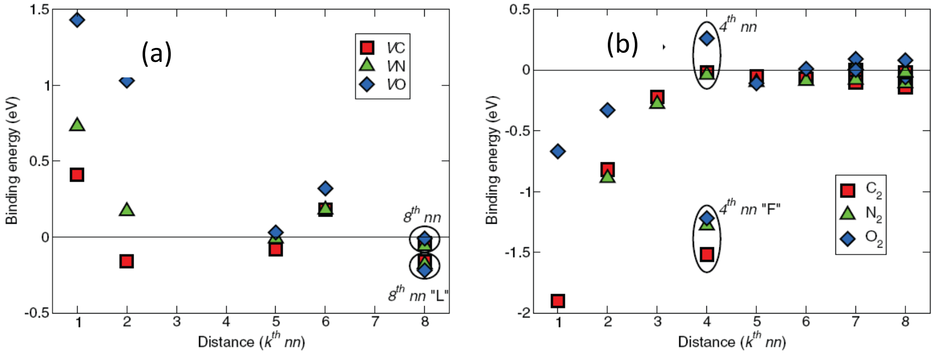

Figure 2.14 Binding energy as a function of distance among (a) vacancy and solute atoms (b) two solute atoms [164].

Moreover, Bialon *et al.* [163] investigated the interaction of B atom with other solutes and its migration barriers for substitutional and interstitial mechanisms in bcc-Fe. The interaction behaviour of C, N, O and their interaction with vacancies in bcc-Fe was discussed by Barouh *et al.* [164]. The authors reported that the vacancy tends to bind SAs whereas, repulsive interaction is observed among two SAs (Figure 2.14). Their study has highlighted that the voronoi volume is the decisive factor for the configurational preferences of solute elements over atomic size of the SAs. Whereas, Baik *et al.* [175] concluded that the stability of B is decided by the geometrical factor rather than the nature of the chemical bonding.

Despite the numerous reports on SAs interaction in bcc-Fe, only a few reports are available for fcc-Fe in the literature, and many of them are primarily limited to the solute dissolution, diffusion and their influence on staking fault energies [165,181-186]. He *et al.* [165] studied interaction among C and B with vacancies in both bcc and fcc-Fe lattice and observed that vacancy trapping ability was stronger in bcc-Fe as compared to fcc-Fe. The repulsion between C atoms in fcc-Fe lattice was observed by Ponomareva *et al.* [184]. The interaction of C and N with vacancy in fcc-Fe was also studied by Slane *et al*. [187] and Fei Ye *et al*. [185], respectively.

References

[1] G. S. Was, (Springer, 2007).

[2] O. Woo, C. Judge, H. Nordin, D. Finlayson, and C. Andrei, Microscopy and Microanalysis **17**, 1852 (2011).

[3] R. Schäublin, Z. Yao, P. Spätig, and M. Victoria, Materials Science and Engineering: A **400-401**, 251 (2005).

[4] Y. N. Osetsky, A. Serra, M. Victoria, S. I. Golubov, and V. Priego, Philosophical Magazine A **79**, 2285 (1999).

[5] L. M. Howe and J. F. McGurn, Applied Physics Letters **4**, 99 (1964).

[6] N. Baluc, C. Bailat, Y. Dai, M. I. Luppo, R. Schaublin, and M. Victoria, MRS Proceedings **540**, 539, 539 (1998).

[7] R. Schäublin *, Z. Yao, N. Baluc, and M. Victoria, Philosophical Magazine **85**, 769 (2005).

[8] S. J. Zinkle and L. L. Snead, Journal of Nuclear Materials **225**, 123 (1995).

[9] Z. Yao, M. J. Caturla, and R. Schäublin, Journal of Nuclear Materials **367-370**, 298 (2007).

[10] M. J. Norgett, M. T. Robinson, and I. M. Torrens, Nuclear Engineering and Design **33**, 50 (1975).

[11] G. H. Kinchin and R. S. Pease, Reports on Progress in Physics **18**, 1 (1955).

[12] M. H.-M. a. M. J. Caturla, (Woodhead Publishing, Cambridge, 2010).

[13] J. F. Ziegler, M. D. Ziegler, and J. P. Biersack, Nuclear Instruments and Methods in Physics Research Section B: Beam Interactions with Materials and Atoms **268**, 1818 (2010).

[14] J. P. B. a. M. D. Z. J.F. Ziegler, edited by I. I. Press2008).

[15] N. Yoshida, Journal of Nuclear Materials **174**, 220 (1990).

[16] N. Hashimoto, S. J. Zinkle, A. F. Rowcliffe, J. P. Robertson, and S. Jitsukawa, Journal of Nuclear Materials **283-287**, 528 (2000).

[17] J. Gan and G. S. Was, Journal of Nuclear Materials **297**, 161 (2001).

[18] T. S. Byun, K. Farrell, E. H. Lee, J. D. Hunn, and L. K. Mansur, Journal of Nuclear Materials **298**, 269 (2001).

[19] D. J. Edwards, E. P. Simonen, and S. M. Bruemmer, Journal of Nuclear Materials **317**, 13 (2003).

[20] D. J. Edwards, E. P. Simonen, F. A. Garner, L. R. Greenwood, B. M. Oliver, and S. M. Bruemmer, Journal of Nuclear Materials **317**, 32 (2003).

[21] S. J. Zinkle and Y. Matsukawa, Journal of Nuclear Materials **329-333**, 88 (2004).

[22] M. Victoria, N. Baluc, C. Bailat, Y. Dai, M. I. Luppo, R. Schắublin, and B. N. Singh, Journal of Nuclear Materials **276**, 114 (2000).

[23] M. Hernández-Mayoral and D. Gómez-Briceño, Journal of Nuclear Materials **399**, 146 (2010).

[24] J. Kočík, E. Keilová, J. Čížek, and I. Procházka, Journal of Nuclear Materials **303**, 52 (2002).

[25] R. Chaouadi and R. Gérard, Journal of Nuclear Materials **345**, 65 (2005).

[26] M. Lambrecht, L. Malerba, and A. Almazouzi, Journal of Nuclear Materials **378**, 282 (2008).

[27] D. J. Bacon and Y. N. Osetsky, Materials Science and Engineering: A **400-401**, 353 (2005).

[28] C. Bouchet, B. Tanguy, J. Besson, and S. Bugat, Computational Materials Science **32**, 294 (2005).

[29] W. Van Renterghem, M. J. KonstantinoviÄ‡, and M. Vankeerberghen, Journal of Nuclear Materials **452**, 158.

[30] G. R. Odette, MRS Proceedings **373**, 137, 137 (1994).

[31] G. R. Odette and B. D. Wirth, Journal of Nuclear Materials **251**, 157 (1997).

[32] J. M. Hyde and C. A. English, MRS Online Proceedings Library Archive **650** (2000).

[33] P. Pareige, J. Van Duysen, and P. Auger, Applied surface science **67**, 342 (1993).

[34] P. Auger, P. Pareige, S. Welzel, and J. Van Duysen, Journal of Nuclear Materials **280**, 331 (2000).

[35] A. Wagner, A. Ulbricht, F. Bergner, and E. Altstadt, Nuclear Instruments and Methods in Physics Research Section B: Beam Interactions with Materials and Atoms **280**, 98 (2012).

[36] K. Lindgren, *Effects of Irradiation and Thermal Ageing on the Nanoscale Chemistry of Steel Welds* (Department of Physics, Chalmers University of Technology, 2018).

[37] M. K. Miller and K. F. Russell, Journal of Nuclear Materials **371**, 145 (2007).

[38] M. Miller, R. Nanstad, M. Sokolov, and K. Russell, Journal of Nuclear Materials **351**, 216 (2006).

[39] P. Pareige, B. Radiguet, A. Suvorov, M. Kozodaev, E. Krasikov, O. Zabusov, and J. Massoud, Surface and Interface Analysis: An International Journal devoted to the development and application of techniques for the analysis of surfaces, interfaces and thin films **36**, 581 (2004).

[40] K. Lindgren, Chalmers University of Technology, 2018.

[41] E. FORTNER, S. GRANT, and J. HAWTHORNE, WELD J **49**, 453 (1970).

[42] U. Potapovs and J. R. Hawthorne, Nuclear Applications **6**, 27 (1969).

[43] F. A. Smidt and H. E. Watson, Metallurgical Transactions **3**, 2065 (1972).

[44] G. Odette and G. Lucas, ASTM STP **909**, 206 (1986).

[45] G. Odette and G. Lucas, Radiation effects and defects in solids **144**, 189 (1998).

[46] E. D. Eason, G. R. Odette, R. K. Nanstad, and T. Yamamoto, ORNL/TM-2006/530, Oak Ridge National Laboratory (2007).

[47] P. D. Styman, Oxford University, UK, 2013.

[48] G. R. Odette and R. K. Nanstad, Jom **61**, 17 (2009).

[49] R. Ngayam-Happy, C. Becquart, C. Domain, and L. Malerba, Journal of Nuclear Materials **426**, 198 (2012).

[50] M. A. S. S. R. O. P. D. S. Randy K. Nanstad, *Neutron and Thermal Embrittlement of RPV Steels: An Overview*
International Review of Nuclear Reactor Pressure Vessel Surveillance Programs (ASTM International, West Conshohocken, PA, 2018).

[51] U. Potapovs and J. R. Hawthorne, Nuclear Applications **6**, 27 (1969).

[52] F. Smidt and H. Watson, Metallurgical Transactions **3**, 2065 (1972).

[53] G. R. Odette, Scripta Metallurgica **17**, 1183 (1983).

[54] J. Zelenty, Materials Science and Technology **31**, 981 (2015).

[55] S. Fisher and J. Buswell, International Journal of Pressure Vessels and Piping **27**, 91 (1987).

[56] M. Miller, P. Pareige, and M. Burke, Materials Characterization **44**, 235 (2000).

[57] P. B. Wells, T. Yamamoto, B. Miller, T. Milot, J. Cole, Y. Wu, and G. R. Odette, Acta Materialia **80**, 205 (2014).

[58] M. K. Miller, K. A. Powers, R. K. Nanstad, and P. Efsing, Journal of Nuclear Materials **437**, 107 (2013).

[59] C. Liu, G. Odette, B. Wirth, and G. Lucas, Materials Science and Engineering: A **238**, 202 (1997).

[60] S. C. Glade *, B. D. Wirth, G. R. Odette, P. Asoka-Kumar, P. A. Sterne, and R. H. Howell, Philosophical Magazine **85**, 629 (2005).

[61] E. Meslin, B. Radiguet, P. Pareige, and A. Barbu, Journal of Nuclear Materials **399**, 137 (2010).

[62] E. Hornbogen, Transactions of the Metallurgical Society of AIME **218**, 1064 (1960).

[63] Q. Chen and Z. Jin, Metallurgical and Materials Transactions A **26**, 417 (1995).

[64] S. R. Goodman, S. S. Brenner, and J. R. Low, Metallurgical Transactions **4**, 2363 (1973).

[65] G. M. Worrall, J. T. Buswell, C. A. English, M. G. Hetherington, and G. D. W. Smith, Journal of Nuclear Materials **148**, 107 (1987).

[66] M. Charleux, F. Livet, F. Bley, F. Louchet, and Y. Bréchet, Philosophical Magazine A **73**, 883 (1996).

[67] F. Maury, N. Lorenzelli, M. H. Mathon, C. H. d. Novion, and P. Lagarde, Journal of Physics: Condensed Matter **6**, 569 (1994).

[68] S. M. He, N. H. van Dijk, M. Paladugu, H. Schut, J. Kohlbrecher, F. D. Tichelaar, and S. van der Zwaag, Physical Review B **82**, 174111 (2010).

[69] T. Onitsuka, M. Takenaka, E. Kuramoto, Y. Nagai, and M. Hasegawa, Physical Review B **65**, 012204 (2001).

[70] R. Prakash Kolli and D. N. Seidman, Acta Materialia **56**, 2073 (2008).

[71] S. R. Goodman, S. S. Brenner, and J. R. Low, Metallurgical Transactions **4**, 2371 (1973).

[72] G. Salje and M. Feller-Kniepmeier, Journal of Applied Physics **48**, 1833 (1977).

[73] Y. Le Bouar, Acta Materialia **49**, 2661 (2001).

[74] J.-H. Shim, Y. W. Cho, S. C. Kwon, W. W. Kim, and B. D. Wirth, Applied Physics Letters **90**, 021906 (2007).

[75] M. K. Miller, K. F. Russell, P. Pareige, M. J. Starink, and R. C. Thomson, Materials Science and Engineering: A **250**, 49 (1998).

[76] P. Auger, P. Pareige, M. Akamatsu, and D. Blavette, Journal of Nuclear Materials **225**, 225 (1995).

[77] S. Shu, N. Almirall, P. B. Wells, T. Yamamoto, G. R. Odette, and D. D. Morgan, Acta Materialia **157**, 72 (2018).

[78] P. D. Styman, J. M. Hyde, A. Morley, K. Wilford, N. Riddle, and G. D. W. Smith, Materials Science and Engineering: A **736**, 111 (2018).

[79] A. Deschamps, M. Militzer, and W. J. Poole, ISIJ International **41**, 196 (2001).

[80] P. J. Othen, M. L. Jenkins, G. D. W. Smith, and W. J. Phythian, Philosophical Magazine Letters **64**, 383 (1991).

[81] H. Hauser, R. Grössinger, F. Keplinger, and M. Schönhart, Journal of Magnetism and Magnetic Materials **320**, e983 (2008).

[82] D. G. Park, K. S. Ryu, S. Kobayashi, S. Takahashi, and Y. M. Cheong, Journal of Applied Physics **107**, 09A330 (2010).

[83] L. P. Vandenbossche, M. J. Konstantinović, A. Almazouzi, and L. R. Dupré, Journal of Physics D: Applied Physics **40**, 4114 (2007).

[84] L. Cao, S. Wu, and B. Liu, Materials & Design **47**, 551 (2013).

[85] P. Othen, M. Jenkins, and G. Smith, Philosophical Magazine A **70**, 1 (1994).

[86] S. Cammelli, C. Degueldre, A. Cervellino, S. Abolhassani, G. Kuri, J. Bertsch, D. Lützenkirchen-Hecht, and R. Frahm, Nuclear Instruments and Methods in Physics Research Section B: Beam Interactions with Materials and Atoms **268**, 632 (2010).

[87] S. Pizzini, K. J. Roberts, W. J. Phythian, C. A. English, and G. N. Greaves, Philosophical Magazine Letters **61**, 223 (1990).

[88] R. Monzen, M. L. Jenkins, and A. P. Sutton, Philosophical Magazine A **80**, 711 (2000).

[89] J. J. Blackstock and G. J. Ackland, Philosophical Magazine A **81**, 2127 (2001).

[90] M. Ludwig, D. Farkas, D. Pedraza, and S. Schmauder, Modelling and Simulation in Materials Science and Engineering **6**, 19 (1999).

[91] R. Oriani and G. Speich, TRANS METALL SOC AIME **233**, 623 (1965).

[92] R. Monzen, K. Takada, and K. Matsuda, Zeitschrift für Metallkunde **94**, 1241 (2003).

[93] R. Monzen, K. Takada, and C. Watanabe, ISIJ International **44**, 442 (2004).

[94] K. Osamura, H. Okuda, K. Asano, M. Furusaka, K. Kishida, F. Kurosawa, and R. Uemori, ISIJ International **34**, 346 (1994).

[95] R. P. Kolli and D. N. Seidman, Microscopy and Microanalysis **20**, 1727 (2014).

[96] T. Nagano and M. Enomoto, Scripta materialia **55**, 223 (2006).

[97] A. Seko, S. R. Nishitani, I. Tanaka, H. Adachi, and E. F. Fujita, Calphad **28**, 173 (2004).

[98] C. Zhang and M. Enomoto, Acta Materialia **54**, 4183 (2006).

[99] I. M. Lifshitz and V. V. Slyozov, Journal of Physics and Chemistry of Solids **19**, 35 (1961).

[100] F. Soisson, A. Barbu, and G. Martin, Acta Materialia **44**, 3789 (1996).

[101] A. Umantsev and G. B. Olson, Scripta Metallurgica et Materialia **29**, 1135 (1993).

[102] D. A. P. a. K. E. Easterling, (Springer, 1992).

[103] J. Chojcan, Journal of Alloys and Compounds **264**, 50 (1998).

[104] J. Chojcan, physica status solidi (b) **219**, 375 (2000).

[105] C. Domain, C. S. Becquart, and J. Foct, Physical Review B **69**, 144112 (2004).

[106] T. Ohnuma, N. Soneda, and M. Iwasawa, Acta Materialia **57**, 5947 (2009).

[107] S. Ahlawat, K. Srinivasu, A. Biswas, and N. Choudhury, Computational Materials Science **170**, 109167 (2019).

[108] E. Vincent, C. S. Becquart, and C. Domain, Nuclear Instruments and Methods in Physics Research Section B: Beam Interactions with Materials and Atoms **228**, 137 (2005).

[109] C. Domain and C. S. Becquart, Physical Review B **65**, 024103 (2001).

[110] E. Vincent, C. S. Becquart, and C. Domain, Journal of Nuclear Materials **359**, 227 (2006).

[111] P. Olsson, T. P. C. Klaver, and C. Domain, Physical Review B **81**, 054102 (2010).

[112] N. I. Medvedeva, A. S. Murthy, V. L. Richards, D. C. Van Aken, and J. E. Medvedeva, Journal of Materials Science **48**, 1377 (2013).

[113] W.-x. Song and S.-j. Zhao, Physical Chemistry Chemical Physics **16**, 7222 (2014).

[114] T. Toyama, Y. Nozawa, W. Van Renterghem, Y. Matsukawa, M. Hatakeyama, Y. Nagai, A. Al Mazouzi, and S. Van Dyck, Journal of Nuclear Materials **418**, 62 (2011).

[115] D. Stork *et al.*, Fusion Engineering and Design **89**, 1586 (2014).

[116] A. Etienne, B. Radiguet, N. J. Cunningham, G. R. Odette, R. Valiev, and P. Pareige, Ultramicroscopy **111**, 659 (2011).

[117] D. Kiener, P. Hosemann, S. A. Maloy, and A. M. Minor, Nat Mater **10**, 608 (2011).

[118] J. T. B. Zinkle S.J., materials Today **12**, 12 (2009).

[119] H. R. Brager and F. A. Garner, Journal of Nuclear Materials **108-109**, 347 (1982).

[120] P. J. Maziasz and D. N. Braski, Journal of Nuclear Materials **122**, 311 (1984).

[121] P. J. Maziasz, Journal of Nuclear Materials **122**, 472 (1984).

[122] S. Zinkle, P. Maziasz, and R. Stoller, Journal of Nuclear Materials **206**, 266 (1993).

[123] M. L. Grossbeck, K. Ehrlich, and C. Wassilew, Journal of Nuclear Materials **174**, 264 (1990).

[124] G. R. Odette and G. E. Lucas, Journal of Nuclear Materials **179-181**, 572 (1991).

[125] G. E. Lucas, Journal of Nuclear Materials **206**, 287 (1993).

[126] T. R. Allen and G. S. Was, Acta Materialia **46**, 3679 (1998).

[127] D. Harries, Journal of Nuclear Materials **82**, 2 (1979).

[128] P. J. Maziasz, Journal of Nuclear Materials **205**, 118 (1993).

[129] S. J. Zinkle, P. J. Maziasz, and R. E. Stoller, Journal of Nuclear Materials **206**, 266 (1993).

[130] C. Pokor, Y. Brechet, P. Dubuisson, J. P. Massoud, and A. Barbu, Journal of Nuclear Materials **326**, 19 (2004).

[131] A. Etienne, M. Hernández-Mayoral, C. Genevois, B. Radiguet, and P. Pareige, Journal of Nuclear Materials **400**, 56 (2010).

[132] E. A. Kenik and K. Hojou, Journal of Nuclear Materials **191-194**, 1331 (1992).

[133] S. Watanabe, J. Satou, N. Sakaguchi, H. Takahashi, and C. Namba, Journal of Nuclear Materials **239**, 200 (1996).

[134] N. Hashimoto, E. Wakai, and J. P. Robertson, Journal of Nuclear Materials **273**, 95 (1999).

[135] K. K. Kadyrzhanov and O. Maksimkin, Journal of Astm International **1** (2004).

[136] S. M. Bruemmer, E. P. Simonen, P. M. Scott, P. L. Andresen, G. S. Was, and J. L. Nelson, Journal of Nuclear Materials **274**, 299 (1999).

[137] A. F. Rowcliffe, S. J. Zinkle, J. F. Stubbins, D. J. Edwards, and D. J. Alexander, Journal of Nuclear Materials **258-263**, 183 (1998).

[138] J. Dudognon, M. Vayer, A. Pineau, and R. Erre, Surface and Interface Analysis: An International Journal devoted to the development and application of techniques for the analysis of surfaces, interfaces and thin films **40**, 772 (2008).

[139] N. Hayashi, I. Sakamoto, and T. Takahashi, Journal of Nuclear Materials **128**, 756 (1984).

[140] C. Abromeit, Journal of Nuclear Materials **216**, 78 (1994).

[141] D. Mazey, Journal of Nuclear Materials **174**, 196 (1990).

[142] J. Dudognon, M. Vayer, A. Pineau, and R. Erre, Surface and Coatings Technology **203**, 180 (2008).

[143] H. F. Huang, J. J. Li, D. H. Li, R. D. Liu, G. H. Lei, Q. Huang, and L. Yan, Journal of Nuclear Materials **454**, 168 (2014).

[144] O. Morozov, V. Zhurba, I. Neklyudov, O. Mats, A. Rud, N. Chernyak, and V. Progolaieva, Nanoscale Research Letters **10**, 154 (2015).

[145] H. Sanda, M. Takai, S. Namba, A. Chayahara, and M. Satou, Applied Physics A **50**, 573 (1990).

[146] B. Radiguet, A. Etienne, P. Pareige, X. Sauvage, and R. Valiev, Journal of Materials Science **43**, 7338 (2008).

[147] A. Etienne, B. Radiguet, P. Pareige, J. P. Massoud, and C. Pokor, Journal of Nuclear Materials **382**, 64 (2008).

[148] I. Sakamoto, N. Hayashi, B. Furubayashi, and H. Tanoue, Journal of applied physics **68**, 4508 (1990).

[149] J. Dudognon, M. Vayer, A. Pineau, and R. Erre, Surface and Coatings Technology **202**, 5048 (2008).

[150] A. Etienne, B. Radiguet, N. J. Cunningham, G. R. Odette, and P. Pareige, Journal of Nuclear Materials **406**, 244 (2010).

[151] C. Pokor, Y. Brechet, P. Dubuisson, J.-P. Massoud, and A. Barbu, Journal of Nuclear Materials **326**, 19 (2004).

[152] P. Maziasz, Journal of Nuclear Materials **205**, 118 (1993).

[153] E. Kenik and K. Hojou, Journal of Nuclear Materials **191**, 1331 (1992).

[154] N. Hashimoto, E. Wakai, and J. Robertson, Journal of Nuclear Materials **273**, 95 (1999).

[155] S. Watanabe, J. Satou, N. Sakaguchi, H. Takahashi, and C. Namba, Journal of Nuclear Materials **239**, 200 (1996).

[156] T. R. Allen and G. Was, Acta Materialia **46**, 3679 (1998).

[157] Q. Wang, H. Ogiso, S. Nakano, J. Akedo, and H. Ishikawa, Nuclear Instruments and Methods in Physics Research Section B: Beam Interactions with Materials and Atoms **206**, 118 (2003).

[158] R. Vardiman and I. Singer, Materials Letters **2**, 150 (1983).

[159] J. D. Kamminga, T. P. C. Klaver, K. Nakata, B. J. Thijsse, and G. C. A. M. Janssen, Journal of Computer-Aided Materials Design **10**, 1 (2003).

[160] D. Simonovic, C. K. Ande, A. I. Duff, F. Syahputra, and M. H. F. Sluiter, Physical Review B **81**, 054116 (2010).

[161] M. H. F. Sluiter, Proc. 3rd Int. Symp. on Steel Science, 29 (2012).

[162] M. Souissi, Y. Chen, M. H. F. Sluiter, and H. Numakura, Computational Materials Science **124**, 249 (2016).

[163] A. F. Bialon, T. Hammerschmidt, and R. Drautz, Physical Review B **87**, 104109 (2013).

[164] C. Barouh, T. Schuler, C.-C. Fu, and M. Nastar, Physical Review B **90**, 054112 (2014).

[165] T. He, Y. Jiang, R. Zhou, and J. Feng, RSC Advances **6**, 45250 (2016).

[166] O. I. Gorbatov, A. H. Delandar, Y. N. Gornostyrev, A. V. Ruban, and P. A. Korzhavyi, Journal of Nuclear Materials **475**, 140 (2016).

[167] A. V. Ruban, P. A. Korzhavyi, and B. Johansson, Physical Review B **77**, 094436 (2008).

[168] O. I. Gorbatov, I. K. Razumov, Y. N. Gornostyrev, V. I. Razumovskiy, P. A. Korzhavyi, and A. V. Ruban, Physical Review B **88**, 174113 (2013).

[169] C. J. Först, J. Slycke, K. J. Van Vliet, and S. Yip, Physical Review Letters **96**, 175501 (2006).

[170] Y. Jiang, J. R. Smith, and G. R. Odette, Physical Review B **79**, 064103 (2009).

[171] A. T. Paxton and C. Elsässer, Physical Review B **87**, 224110 (2013).

[172] D. Terentyev, K. Heinola, A. Bakaev, and E. E. Zhurkin, Scripta Materialia **86**, 9 (2014).

[173] C. L. Fu, M. Krčmar, G. S. Painter, and X.-Q. Chen, Physical Review Letters **99**, 225502 (2007).

[174] D. H. R. Fors and G. Wahnström, Physical Review B **77**, 132102 (2008).

[175] S. S. Baik, B. I. Min, S. K. Kwon, and Y. M. Koo, Physical Review B **81**, 144101 (2010).

[176] L.-H. Li, W.-L. Wang, L. Hu, and B.-B. Wei, Intermetallics **46**, 211 (2014).

[177] R. Nazarov, T. Hickel, and J. Neugebauer, Physical Review B **82**, 224104 (2010).

[178] D. Di Stefano, R. Nazarov, T. Hickel, J. Neugebauer, M. Mrovec, and C. Elsässer, Physical Review B **93**, 184108 (2016).

[179] D. Tanguy, Y. Wang, and D. Connétable, Acta Materialia **78**, 135 (2014).

[180] A. T. Paxton and I. H. Katzarov, Acta Materialia **103**, 71 (2016).

[181] A. Abbasi, A. Dick, T. Hickel, and J. Neugebauer, Acta Materialia **59**, 3041 (2011).

[182] D. J. Hepburn, D. Ferguson, S. Gardner, and G. J. Ackland, Physical Review B **88**, 024115 (2013).

[183] D. E. Jiang and E. A. Carter, Physical Review B **67**, 214103 (2003).

[184] A. V. Ponomareva, Y. N. Gornostyrev, and I. A. Abrikosov, Journal of Experimental and Theoretical Physics **120**, 716 (2015).

[185] F. Ye, K. Tong, Y. K. Wang, Z. Li, and F. Zhou, Computational Materials Science **149**, 65 (2018).

[186] S. Kibey, J. B. Liu, M. J. Curtis, D. D. Johnson, and H. Sehitoglu, Acta Materialia **54**, 2991 (2006).

[187] J. A. Slane, C. Wolverton, and R. Gibala, Metallurgical and Materials Transactions A **35**, 2239 (2004).

Chapter 3

Characterization Techniques and Theoretical Methods

This chapter provides brief introduction of experimental techniques and theoretical methods that are employed in this thesis work. This thesis chapter is divided into two sections: first section describes the details of experimental techniques; second section covers the details of first principle method for electronic structure calculation, which is studied under the framework of density functional theory. Mainly two complementary experimental techniques i.e. atom probe tomography (APT) and small angle neutron scattering (SANS) are utilized to understand the precipitate evolution in terms of their number density, size and morphology. Basic principles of a few other techniques like micro-hardness, x-ray diffraction, differential scanning calorimetry and sample preparation methods are also discussed.

3.1 Alloy preparation and heat treatment

Fe - 1.4 at% Cu binary alloy is prepared by vacuum arc melting under high purity argon atmosphere using high purity (99.99%) alloying elements. The alloy ingot is re-melted 4-5 times in order to ascertain chemical homogeneity. The ingot is hot-rolled in multiple passes at 1173 K to reduce the thickness to 1.5 mm. The hot-rolled strips are then solutionized at 1273 K for 30 min followed by water quenching. Seven different samples are cut from the solutionized hot-rolled strip and these samples are sealed in quartz tube under helium gas pressure of about 100 torr. The samples are subjected to the thermal aging process at 773 K for the following durations: 1, 3, 5, 8, 25, 50 and 100 h. This heat treatment is followed by ice quenching in order to retain the high temperature phase at room temperature.

3.2. Atom probe tomography (APT)

The basic principle of APT is the controlled removal of surface atoms. APT provides three-dimensional (3D) atomic arrangement and chemical composition of materials at atomic scale. APT produces 3D image of internal structures by combining time-of-flight mass spectrometer with position sensitive detectors. APT data includes 3D position and identity of individual atoms in the analyzed volume that contains millions of atoms. The detailed information about APT is given in references [1-2].

3.2.1 Basic Principle of APT

APT principle is based on the process of field evaporation. The field-induced removal of atom from its own lattices is known as field evaporation. Field evaporation involves the combination of ionization and desorption of atoms from the sample surface, which is subjected to an intense direct electric field. To field evaporate the atoms from sample surface, pulsed laser/high-voltage is also applied to sample along with the direct electric field. The field evaporation process starts with ionization of surface atoms and immediately after that surface ions evaporate. The APT sample is in needle shape with an apex diameter of the order of 100 nm. Moreover, the sample tip is kept at cryogenic temperatures in order to reduce the thermal vibration of atoms which can improve spatial resolution. The schematic diagram for APT is shown in Figure 3.1. The magnitude of electric field at sample tip can be estimated using following relation [2]

$$E = \frac{V}{KR}$$

Here, V is the applied voltage, R is the tip radius and K is known as the field factor which is a constant that accounts for tip shape. More details on K can be found in reference [2].

The chemical identity of the ion is detected by a time-of-flight mass spectrometer, by recording the time between the field evaporating pulse and the detection event for each detected ion. The information of the detected ion is given by its mass to charge state ratio and is calculated using the potential energy and the kinetic energy of the ion. The mass to charge state ratio is given as [2]:

$$\frac{m}{n} = M \approx 2eV \left(\frac{t_{flight}}{L}\right)^2 \quad \ldots\ldots\ldots\ldots\ldots.. \ (3.1)$$

where, m/n (=M) is the mass to charge state ratio of ions, V is the applied voltage , t_{flight} is the time of flight and L is the flight distance between the specimen and the detector and e is the electron charge.

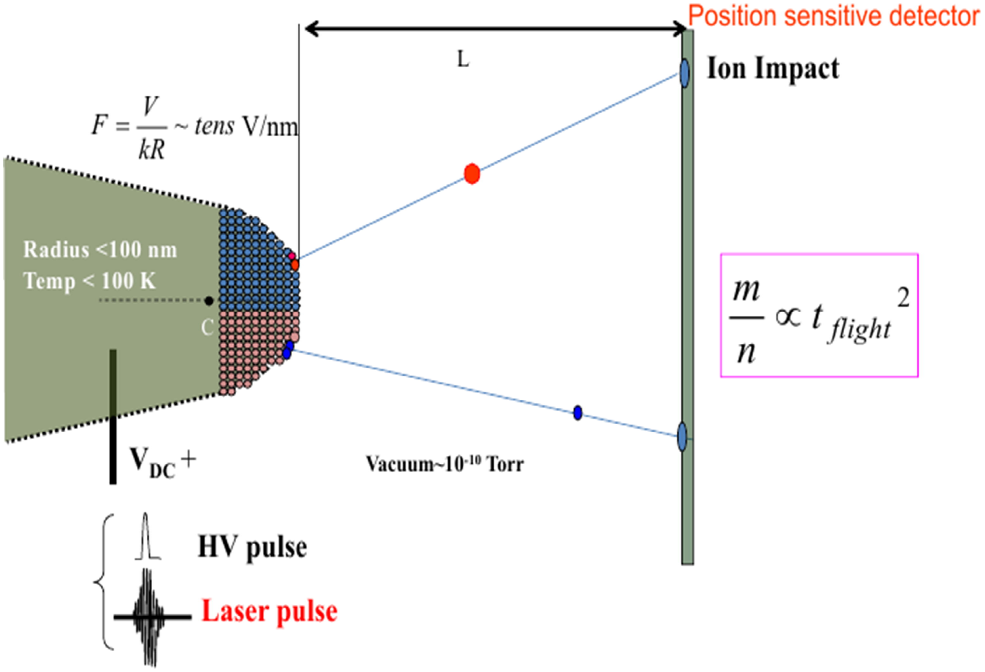

Figure 3.1 Schematic diagram of atom probe microscope.

Further, 3D position of the ions in the sample is reconstructed using their position on the position sensitive delay line detector. The choice of the reconstruction parameters is particularly important, as the incorrect parameters can lead to distorted and flawed reconstructions.

3.2.2 APT sample preparation

Field evaporation of ions is central to APT. But, extremely high field (10-60 V nm^{-1}) is required to accomplish the process of field evaporation. This kind of field strength can be achieved by making the samples in the shape of sharp needle with an end radius of the order of 50 to 100 nm. Therefore, the sample preparation is a very critical step for APT experiments. Generally, two different techniques are used for APT sample preparation and both are discussed briefly in the next sections.

3.2.2.1 Two-step electro-polishing method

Electro-polishing is the most convenient method to prepare needle-shaped samples for APT from electrically conducting materials. This makes it quite popular for metallic samples. It requires the starting material to be in the form of matchstick-shaped blanks (Figure 3.2), having 10mm length and about 0.3mm X 0.3mm width. The asymmetric cross-section of the specimen blank is one of the main reasons behind specimen preparation failure, therefore it must have nearly square cross-section for successful sample preparation. These blanks are normally prepared by cutting specimens with fine precision using rotating diamond saw or electrical discharge machining.

A two-step electro-polishing process is ideally employed i.e. rough polishing and fine polishing. The different electrolytes are used for different materials and a list of suitable electrolytes for various materials is available in reference [1]. Quite a few different types of electro-polishing experimental set ups are in use, and we have used a horizontal geometry set up (Figure 3.2(a)). In this process, the blank is connected to positive voltage and the counter electrode that is usually made of noble materials like platinum is connected to negative voltage. As the voltage applied between the sample and the electrode, current passes from anode to cathode. The electrochemical reaction at anode removes the material which is inside the electrolyte and this process gradually forms neck region in the blank (Figure 3.2(b)). After neck formation, fine polishing is recommended to achieve the final tip shape. The final shape of the sample with a tip radius 50 - 100 nm is shown in Figure 3.2(c).

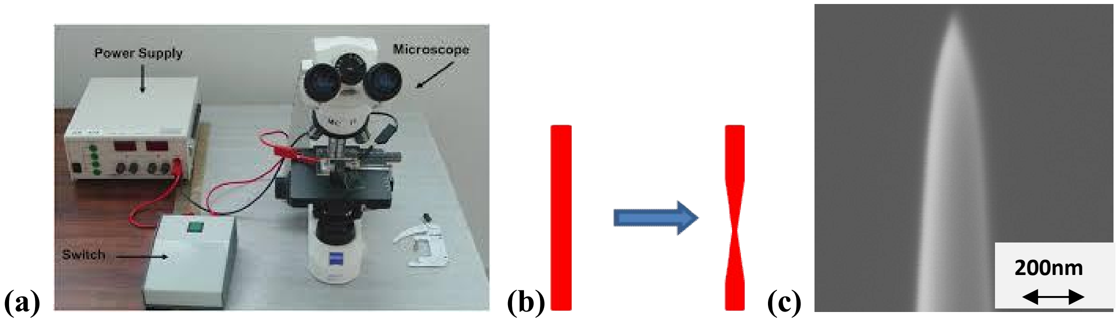

Figure 3.2 (a) Schematic diagram of experimental set-up for electro-polishing (b) blank with neck region and (c) standard shape of APT sample.

3.2.2.2 Focused ion beam (FIB) machining

The needle-shaped samples for APT can also be prepared using FIB; an instrument that usually combines an SEM with a beam of Ga^+ ions. This technique is mainly selected for site-specific sample preparation. Here, both the electron beam and the ion beam can be used for imaging and ion beam is primarily used for milling away the material. This specimen preparation method is discussed in detail in references [2-5]. Figure 3.3 represents the standard steps for APT sample preparation using an FIB. First of all, the region of interest is selected and then platinum (Pt) layer is deposited to protect the surface and mark the region to be extracted (Figure 3.3 (a)). After Pt deposition, the long edges of the selected area are cut using high ion beam current (Figure 3.3 (b)). The width of the cuts should be enough to avoid re-deposition of the milled material. One of the edges is cut to make that side free (Figure 3.3 (c)). Then, the micromanipulator is attached to the free end of lamella via Pt deposition (Figure 3.3 (d)) and now the other end of the lamella is cut using the ion beam (Figure 3.3 (d)). Then, the lamella is lifted out from bulk (Figure 3.3 (d)) and attached with different types of holders e.g. W or Si-post (Figure 3.3 (e)). The last step includes a series of annular milling operations with progressively smaller beam currents and smaller beam inner diameter, until the desired radius is achieved (Figure 3.3 (f)).

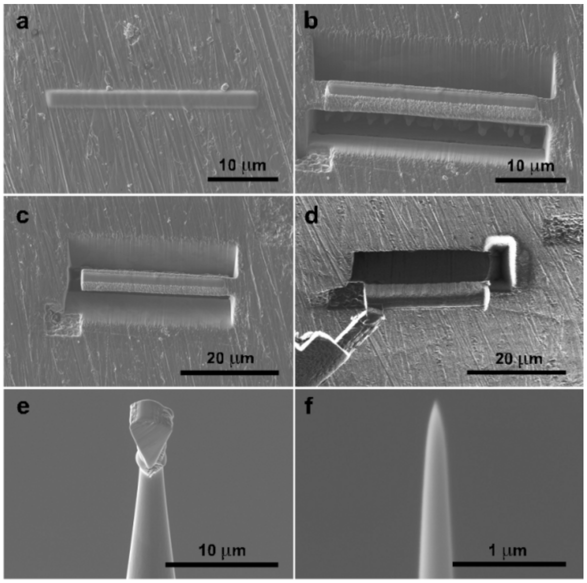

Figure 3.3 Represents standard APT sample preparation procedure using FIB [5]. (a) Platinum deposition on region of interest (b) Trenches cut on both side of platinum deposition (c) One side cut (d) Micromanipulator attached to lamella, cut on other side and lift-out (e) Lift-out is attached to Si-post (f) APT sample is ready after annular milling.

3.3. Small angle neutron scattering (SANS)

SANS is a powerful non-destructive technique used for investigating structures at mesoscopic length scale [6-9]. In this technique the elastic neutron scattering is studied at small scattering angles (0.1 to 10^{o}) close to the direct beam and this distinguishes it from Bragg diffraction which involves large angles. SANS provides the structural data averaged over macroscopic sample volume. Thus, SANS technique [10] having large field of view (FOV), provides excellent statistics, therefore, is more effective for better quantitative analysis of structure having diverse length scales. SANS technique has been found to be an important characterization technique to investigate the wide range of different materials like the precipitation mechanism studies in metallic system [11-12], pore size study in ceramics [13] etc. SANS basically provides statistically average information about morphology, size distribution and volume fraction of the inhomogenities present inside the bulk sample, which affect the macroscopic properties of the material.

3.3.1 Theory of small angle scattering (SAS)

The basic scattering experiment is represented schematically in Figure 3.5. SAS involves an incident monochromatic beam of radiation on the sample and the scattered radiation is measured as a function of the scattering angle, which contains the information about the scatterer present within the sample [14-15]. The incident and scattered radiation wave vectors are denoted by K_i and K_o, respectively. In case of elastic scattering, the magnitude of wave vectors is equal ($K_i = K_o = \frac{2\pi}{\lambda}$, λ is the wavelength of the radiation) and there is only change in the direction of the scattered radiation with respect to the incident radiation. From Figure 3.5, the phase difference between the scattered and the incident beam is $(K_o-K_i).\Delta r$, where $q = K_o-K_i$ is defined as the wave vector transfer. From the scattering geometry in Figure 3.5, the magnitude of q is given as

$$q = 2k\,Sin\theta \quad \text{(where } 2\theta \text{ is the scattering angle)}$$

Further, q can be written as, $q = \frac{4\pi}{\lambda} Sin\theta$

Therefore, q values varies from q=0 for 2θ=0 to a maximum value of $q = \frac{4\pi}{\lambda}$ for 2θ=180. In practice, both the extremities can never be achieved due to interference of the incident beam. It is to note that the wave vector is the Fourier transform of the real-space length scale. Therefore, access of lower q values is required to probe larger structures and vice-versa.

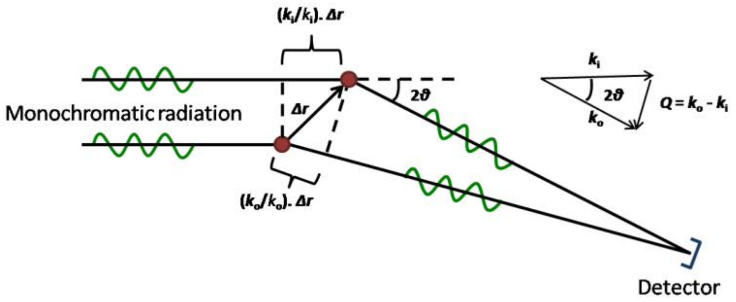

Figure 3.5 Represents schematic of scattering diagram.

3.4 Micro-hardness test

The Vickers micro-hardness measurement is carried out for the solutionized and all the aged samples in order to study the effect of thermal aging on the hardness of the alloy. These measurements have been performed using a Struers make Duramin 2 model micro-hardness instrument with pyramidal diamond indenter. The micro-hardness test is conducted on mirror polished surface under a load and dwell time of 100 gm and 15 s, respectively, for each measurement. The testing samples are prepared by standard metallographic process i.e. grinding and polishing. The Vickers hardness is measured in the units of Vickers hardness number (VHN), which is defined as the load divided by surface area of indentation. The final value of hardness for each sample is determined by averaging 15 different measurements and the standard deviation in data is calculated by measuring the deviation of measured data from the average value.

3.5 Differential Scanning Calorimetery (DSC)

DSC experiment is carried out to monitor the process of precipitation in the Fe-Cu alloy. Isochronous DSC experiment has been performed using a Mettler-Toledo make heat flux type differential scanning calorimeter instrument in argon atmosphere. In DSC, the difference in the heat flow between the sample and a reference is measured by varying temperature. A 2mm X

2mm solutionized sample with flat surface is used for the DSC experiment. An empty aluminium oxide pan is used as reference and sample is also sealed in identical aluminium oxide pan. A heating/cooling rate of 10 ^{o}C/min is used in the temperature range of 25^{o}C to 690^{o}C during the experiment. The presence of endothermic peak during heating cycle is associated with the formation of precipitation in the alloy.

3.6 X-ray diffraction (XRD)

XRD studies are carried out to investigate the effect of thermal aging and irradiation on the crystal structure of the samples. For thermally aged samples, XRD experiments are carried out on Bruker make diffractrometer in Bragg-Brentano geometry using Ni filter and Cu Kα radiation of wavelength 1.54 Ǻ. All the samples are polished to 1μm finish to ensure the flat surface. For irradiated SS316 samples, XRD experiments have been carried out in transmission mode at synchrotron beamline B1-11, Indus2 at RRCAT, Indore, India, using a wavelength of ⋏ = 0.8295 Ǻ. The XRD experiments on all the samples are carried out at room temperature.

3.7 DC Magnetization

The information about existence of magnetic phase transitions in the material is provided by dc magnetization measurements. In the present thesis work, the dc magnetization measurements are carried out to investigate the effect of thermal aging and irradiation on magnetization using vibrating sample magnetometer (VSM). Magnetization is measured using a commercial 9 T PPMS-VSM (make Quantum Design) as a function of applied magnetic filed upto 9 Tesla at room temperature.

3.8 First principle electronic structure calculations

3.8.2 Density Functional Theory (DFT)

DFT provides a clever way to solve the Schrodinger equation for a many-body system and is presently the most successful approach to compute the electronic structure of material. It is made possible by the existence of two ingeniously simple theorems given by Hohenberg and Kohn in 1964. This new approach to the many-body interacting system is based on the following two fundamental theorems of DFT [16-18]:

3.8.2.1 First Hohenberg-Kohn Theorem

This theorem states that "*the external potential* $V_{ext}(\vec{r})$ *of a ground state of an interacting many-electron system is a unique functional of electron density* ($\rho(\vec{r})$) *within a trivial additive constant*". In other words, this theorem states that total energy of the ground state of a many-electron system is uniquely determined by the electron density.

The proof of this theorem is a proof by contradiction and extremely simple. We start by considering two different external potentials V_{ext} and V'_{ext} but both give rise to the same electron density $\rho(\vec{r})$. These two different external potential create two different Hamiltonians corresponding to two different ground state wave functions and energies. Here, we assume that both wave functions give rise to same electron density. Schematically, it can be written as

$$V_{ext} \Rightarrow \hat{H} \Rightarrow \Psi \Rightarrow \quad \rho(\vec{r}) \quad \Leftarrow \Psi' \Leftarrow \hat{H}' \Leftarrow V'_{ext}$$

Therefore, Ψ and Ψ' are different and we can use Ψ' as trial wave function for $\hat{H}$. By virtue of variational principle, we can write

$$E_0 < \langle \Psi' \,|\, \hat{H} \,|\Psi' \rangle = \langle \Psi' \,|\, \hat{H}' \,|\Psi' \rangle + \langle \Psi' \,|\, \hat{H} - \hat{H}' |\, \Psi' \rangle$$

As two Hamiltonian operators differ only in external potential

$$E_0 < E'_0 + \langle \Psi' |\, \hat{T} + \hat{V}_{ee} + \hat{V}_{ext} - \hat{T} - \hat{V}_{ee} - \hat{V}'_{ext} \,|\Psi' \rangle$$

$$E_0 < E'_0 + \int \rho(\vec{r}) \; \{V_{ext} - V'_{ext}\} d\vec{r} \qquad \ldots\ldots (2.4)$$

Similarly, we can use Ψ as a trial wave function for $\widehat{H}'$, we can have

$$E_0' < E_0 - \int \rho(\vec{r})\ \{V_{ext} - V_{ext}'\} d\vec{r}\ \ \ldots\ldots (2.5)$$

After adding equation 2.4 and 2.5, we arrive at clear contradiction: $E_0 + E_0' < E_0' + E_0\ \ or\ 0 < 0$

From the above derivation, it is evident that there cannot be two different external potentials giving rise to the same ground state electron density.

Since the complete ground state energy is a functional of the ground state electron density. Therefore, it can be written as

$$E_0[\rho_0] = T[\rho_0] + E_{ee}[\rho_0] + E_{Ne}[\rho_0]$$

Here, the three terms on the right hand side of the above equation are kinetic energy term, potential energy due to electron-electron interaction and that due to nucleus-electron interaction. The first two terms are universally in nature in the sense that the functional forms of these two terms are system independent and the sum of these two terms are known as Hohenberg-Kohn energy functional $F_{HK}[\rho\,]$, viz.

$$E_0[\rho_0] = F_{HK}[\rho_0] + E_{Ne}[\rho_0]$$

Where, $F_{HK}[\rho\,] = T[\rho\,] + E_{ee}[\rho\,] = \langle\Psi|\hat{T} + \hat{V}_{ee}|\Psi\rangle$

The functional $F_{HK}[\rho]$ is the most important term in density functional theory. If it was known exactly, Schrodinger equation would have been solved exactly. Since it is a universal functional of ground state electron density, it is completely independent of the system, therefore, it applies equally well to the hydrogen atom as well as large molecules such as DNA [16].

3.8.2.2 Second Hohenberg-Kohn Theorem

From the first Hohenberg-Kohn theorem, ground state energy can be written as the functional of ground state electronic density. But, how to ensure that a certain electron density is really the ground state density that we are looking for? A formal prescription for this problem has been given through the second Hohenberg-Kohn theorem. This theorem states that "$F_{HK}[\rho]$ *functional that delivers the ground state energy of the system, delivers the lowest energy if and only if the input electron density is the true ground state density,* ρ_o". This implies that the energy obtained from the energy functional represents an upper bound to the true ground state energy E_0. Mathematically, it can be represented as

$$E_0 \leq E[\tilde{\rho}] = T[\tilde{\rho}] + E_{Ne}[\tilde{\rho}] + E_{ee}[\tilde{\rho}]$$

$\tilde{\rho}$ is any trial electronic density which satisfies the necessary boundary condition such as

$$\tilde{\rho}(\vec{r}) \geq 0 \; and \int \tilde{\rho}(\vec{r}) \, d\vec{r} = N$$

The proof for this is very simple and is based on the variational principle. We recall that any trial density $\tilde{\rho}(\vec{r})$ defines its own Hamiltonian $\tilde{\hat{H}}$ and hence its own wave function $\tilde{\Psi}$. This wave function can now be taken as trial wave function for the Hamiltonian generated from the true external potential V_{ext}. Then we arrive at

$$\langle\tilde{\Psi}|\hat{H}|\tilde{\Psi}\rangle = E[\tilde{\rho}] \geq \langle\Psi_0|\hat{H}|\Psi_0\rangle = E_0[\rho_0]$$

$$E[\tilde{\rho}] \geq E_0[\rho_0]$$

This is the desired result. The quantities ρ_0, Ψ_0 and E_0 in the above equation denote electron density, wave function and total energy of ground state respectively.

3.8.2.3 The Kohn-Sham Approach

The first and second theorem of Hohenberg-Kohn tells us that the total energy of a system can be written in terms of electron density and true ground state electron density can be obtained by using variational principle. These theorems are purely formal and they do not provide any information about the actual form of the functional.

Kohn-Sham in 1965 [16] suggested a method for finding this unknown universal functional. The well known Kohn-Sham approach to DFT, allows an exact description of the interacting many-electron system in terms of an effective non-interacting system. Kohn and Sham introduced the concept of a non-interacting reference system (for which exact form of the kinetic energy is known) built from a set of orbitals (i.e. one electron functions) such that the major part of the kinetic energy can be computed to good accuracy. The remainder of the electronic kinetic energy is merged with the non-classical contributions arising from the electron-electron interactions that is also unknown, but usually quite small. By this method, as much information as possible is computed exactly, leaving aside only a small part of the total energy to be determined by an approximate functional. From Hohenberg-Kohn theorem, we have the following expression [16]

$$E = F[\rho] + \int \rho(\vec{r}) V_{Ne} \, d\vec{r}$$

where the universal functional F(ρ) contains the individual contributions of the kinetic energy, the classical coulomb interaction, the non-classical portion due to self-interaction correction and, exchange and electron correlation effects,

$$F[\rho(\vec{r})] = T[\rho(\vec{r})] + J[\rho(\vec{r})] + E_{ncl}[\rho(\vec{r})]$$

Of these, only J[ρ] is known, while the explicit forms of the other two functionals remain unknown.

The Kohn-Sham orbitals in complete analogy to Hartree-Fock equations, are determined by [16]

$$\hat{f}^{ks} \varphi_i = \varepsilon_i \varphi_i$$

Here, one electron Kohn-Sham operator is defined as: $\hat{f}^{ks} = -\frac{1}{2}\nabla^2 + V_s(\vec{r})$

The connection of this artificial system to the one we are actually interested in is established by choosing the effective potential V_s such that the density resulting from the summation of the moduli of the squared orbitals $\{\phi_i\}$ exactly equals the ground state density of the real system of interacting electrons [16],

$$\rho_s(\vec{r}) = \sum_{i}^{N} \sum_{s} |\varphi_i(\vec{r}, s)|^2 = \rho_0(\vec{r})$$

Certainly, the kinetic energy of non-interacting system is not equal to the true kinetic energy of the interacting system, even if the system share the same density, i.e. $T_s \neq T$. Kohn and Sham accounted for that by the following separation of the functional F(ρ)

$$E[\rho(\vec{r})] = T_s[\rho] + J[\rho] + E_{XC}[\rho] + E_{Ne}[\rho]$$

$$E[\rho(\vec{r})] = F[\rho(\vec{r})] + E_{Ne}[\rho]$$

$$F[\rho(\vec{r})] = T_s[\rho(\vec{r})] + J[\rho(\vec{r})] + E_{XC}[\rho(\vec{r})]$$

Where E_{xc} is exchange-correlation energy and defined as

$$E_{XC}[\rho] = (T(\rho) - T_s[\rho]) + (E_{ee}[\rho] - J[\rho]) = T_c[\rho] + E_{ncl}[\rho]$$

The exchange-correlation energy functional E_{xc} contains everything that is unknown. Further, E_{xc} contains the non-classical effects of self-interaction correction, exchange and correlation, which are contribution to the potential energy of the system, and a portion belonging to the kinetic energy also.

The next difficulty is how we can define effective potential such that it really provides us with a Slater determinant which is characterized by exactly the same density as our real system. For this, the energy of real interacting system can be written as [16]

$$\begin{aligned} E[\rho(\vec{r})] &= T_s[\rho] + J[\rho] + E_{XC}[\rho] + E_{Ne}[\rho] \\ &= T_s[\rho] + \frac{1}{2}\int\int \frac{\rho(\vec{r}_1)\rho(\vec{r}_2)}{r_{12}}\, d\vec{r}_1 d\vec{r}_2 + E_{XC}[\rho] + \int V_{Ne}\, \rho(\vec{r}) d\vec{r} \\ &= -\frac{1}{2}\sum_{i}^{N} \langle\varphi_i|\nabla^2|\varphi_i\rangle + \frac{1}{2}\sum_{i}^{N}\sum_{j}^{N}\int\int |\varphi_i(\vec{r}_1)|^2 \frac{1}{r_{12}} \left|\varphi_j(\vec{r}_2)\right|^2 d\vec{r}_1 d\vec{r}_2 + \\ &\quad + E_{XC}[\rho(\vec{r})] - \sum_{i}^{N}\int \sum_{A}^{M} \frac{Z_A}{r_{1A}} |\varphi_i(\vec{r}_1)|^2\, d\vec{r}_1 \end{aligned}$$

The only unknown term here is E_{xc}. The resulting equations after applying the variational principle and optimize $\{\phi_i\}$ to deliver minimum energy under the usual constraint $<\phi_i|\phi_j> = \delta_{ij}$, are represented as [16]

$$\left(-\frac{1}{2}\nabla^2 + \left[\int \frac{\rho(\vec{r}_2)}{r_{12}} d\vec{r}_2 + V_{XC}(\vec{r}_1) - \sum_A^M \frac{Z_A}{r_{1A}}\right]\right)\varphi_i = \left(-\frac{1}{2}\nabla^2 + V_{eff}(\vec{r}_1)\right)\varphi_i = \varepsilon_i\varphi_i$$

Comparing this equation with the one-particle equations from the non-interacting reference system, we see that

$$V_s(\vec{r}) \equiv V_{eff}(\vec{r}) = \int \frac{\rho(\vec{r}_2)}{r_{12}} d\vec{r}_2 + V_{XC}(\vec{r}_1) - \sum_A^M \frac{Z_A}{r_{1A}}$$

Therefore, once we know the various contributions then we have a grip on the potential V_s which we need to put into one-particle equations, which in turn determine the orbitals and hence the ground state density and the ground state energy. It should be noted that V_{eff} depends on the density through the coulomb term. Here V_{xc} is defined as $V_{XC} \equiv \frac{\delta E_{XC}}{\delta\rho}$

It is important to understand that if the exact forms of E_{xc} and V_{xc} were known, the Kohn-Sham approach would lead to the exact energy. The Kohn-Sham equation does not contain any approximation and in principle is an exact theory. The approximation only comes when we have to choose an explicit form of the unknown functional for the exchange-correlation energy E_{xc} and the corresponding potential V_{xc}. The fundamental goal of modern density functional theory is therefore to find out a better approximation for these two quantities. A variety of approximations have been used to obtain the exchange-correlation energy and the most widely used approximations are the local-density approximation (LDA) [19-20] and generalized gradient approximation (GGA) [21-22]. In the present work, we have used Vienna Ab-initio simulation package (VASP) [23] with GGA and PAW-PBE potentials [24-25].

References

[1] M. K. Miller, edited by K. A. PlenumNew York, 2000.

[2] M. P. M. B. Gault, J.M. Cairney and R. Ringer, edited by S. S. i. M. Science (Springer, New York, 2012).

[3] K. Thompson, D. Lawrence, D. J. Larson, J. D. Olson, T. F. Kelly, and B. Gorman, Ultramicroscopy **107**, 131 (2007).

[4] D. J. Larson, D. T. Foord, A. K. Petford-Long, H. Liew, M. G. Blamire, A. Cerezo, and G. D. W. Smith, Ultramicroscopy **79**, 287 (1999).

[5] K. Lindgren, Chalmers University of Technology, 2018.

[6] R. P. R. Brosali, *Soft Matter Characterization* (Springer, Netherlands, 2008), p. 723.

[7] D. I. Svergun and M. H. J. Koch, Reports on Progress in Physics **66**, 1735 (2003).

[8] S.-H. Chen and T.-L. Lin, in *Methods in Experimental Physics*, edited by D. L. Price, and K. Sköld (Academic Press, 1987), pp. 489.

[9] S. A. Rice, Journal of Polymer Science **19**, 594 (1956).

[10] G. F. A. Guinier, B.C. Walker, L.K. Yudowith, Wiley, New York (1955).

[11] A. Biswas, D. Sen, S. K. Sarkar, Sarita, S. Mazumder, and D. N. Seidman, Acta Materialia **116**, 219 (2016).

[12] A. Guinier, J. Phys. Radium **3**, 124 (1942).

[13] S. Mazumder, D. Sen, S. K. Roy, M. Hainbuchner, M. Baron, and H. Rauch, Journal of Physics: Condensed Matter **13**, 5089 (2001).

[14] V. T. L. Cipelletti, D. J. Pine, edited by J. W. Sons2016).

[15] G. Platz, Berichte der Bunsengesellschaft für physikalische Chemie **96**, 839 (1992).

[16] M. C. H. Wolfram Koch, (Wiley-VCH, 2001).

[17] R. G. P. a. Y. Weitao, *Density-Functional Theory of Atoms and Molecules* (Oxford University Press, New york, 1989).

[18] R. Prasad, (Boca Raton: CRC Press, 2013).

[19] W. Kohn and L. J. Sham, Physical Review **140**, A1133 (1965).

[20] K. Capelle, Brazilian Journal of Physics **36**, 1318 (2006).

[21] J. P. Perdew, J. A. Chevary, S. H. Vosko, K. A. Jackson, M. R. Pederson, D. J. Singh, and C. Fiolhais, Physical Review B **46**, 6671 (1992).

[22] A. García, C. Elsässer, J. Zhu, S. G. Louie, and M. L. Cohen, Physical Review B **46**, 9829 (1992).

[23] G. Kresse and J. Furthmüller, Computational Materials Science **6**, 15 (1996).

[24] G. Kresse and D. Joubert, Physical Review B **59**, 1758 (1999).

[25] J. P. Perdew, K. Burke, and M. Ernzerhof, Physical Review Letters **77**, 3865 (1996).

Chapter 4

Temporal Evolution of Cu-rich Precipitates in Fe-Cu Alloy

In this chapter, the temporal evolution of Cu-rich precipitates (CRPs) during thermal aging of Fe-Cu binary alloy has been investigated by complementary techniques of atom probe tomography (APT) and small angle neutron scattering (SANS). The CRPs have undergone a distinct morphological transformation from spherical to ellipsoidal during aging, which is detected by both the APT and the SANS analyses. A detailed quantitative evaluation of the precipitation process has been performed utilizing the strengths of both these techniques.

4.1 Introduction

Cu precipitation in thermally aged Fe-Cu model alloy has been investigated extensively, both experimentally [1-2] and theoretically [3-4]. However, it may be noted that, among all the different experimental techniques, small angle scattering technique is particularly unique in its ability to provide statistically-averaged analysis over a wide range of length scales (typically 1-1000 nm), making it very effective for such precipitation analysis in metallic system [5-6]. This chapter focuses on temporal evolution of CRPs in Fe-Cu system using SANS technique, but in conjunction with APT.

It is now well accepted that, CRPs show bcc structure at the initial stage [7]. They undergo structural transitions from bcc to fcc, with the following sequence: bcc → 9R → 3R → fcc [7-9] which is already discussed in section 2.4.2 of chapter 2. As for the morphology of the CRPs, early stages of precipitation is known to display spherical morphology which finally transforms to rod-shaped or cylindrical one (when the precipitate diameter > 30nm) presumably due to strain energy effect [10-11]. Othen *et al.* [7] reported the presence of intermediate morphological transformation of CRPs from spherical to ellipsoidal shape. However, very little further work on this intermediate ellipsoid CRPs is available in the archival literature as discussed in section 2.4.3 of chapter 2. Interestingly, the small angle scattering studies on CRPs in Fe-Cu alloys largely ignore this morphological change in their analyses [12-14]. Since small angle scattering is a model dependent technique, the choice of appropriate model becomes primarily important for extracting accurate precipitate characteristics. It is also important to detect and identify the signs of this morphological change in the small angle scattering data, which, to the best of the authors' knowledge, is absent in the literature.

This chapter presents a combined SANS and APT study of temporal evolution of the dimension, number density and morphology of CRPs in Fe-Cu alloy, when aged at 773 K for different durations. Our APT results clearly show the intermediate morphological transition of CRPs from sphere to oblate ellipsoid with increasing aging time. Scattering analysis, on the other hand, has been able to reveal quantitative evolution for this shape transition for the first time in this system. Unlike the previous SANS studies of Fe-Cu alloys, the morphological transition has been incorporated as evidence by APT, while modelling the SANS data. In addition, the experimentally observed temporal dependence of mean radius and number density corroborates fairly well with the LSW model.

4.2 Experimental details

Fe-1.4 at. % Cu binary alloy has been prepared and the detailed information on alloy preparation method and heat treatments are given in section 3.1 of chapter 3. Detailed characterization of these alloys has been carried out using x-ray diffraction (XRD), differential scanning calorimetry (DSC), DC magnetization measurements, atom probe tomography (APT), small angle neutron scattering (SANS) and Vicker's microhardness. The details of all the experimental techniques are given in chapter 3.

APT specimens are machined from the bulk samples to the dimension: 0.3mm x 0.3mm x 8 mm and subsequently electropolished in two stages using 10 vol % perchloric acid in methanol and 2 vol % perchloric acid in butoxyethanol, respectively (as per section 3.2.2.1). APT experiments are carried out at a sample temperature of 30 K under ultrahigh vacuum ~ 1.5 E -10 mbar, using a CAMECA FlexTAP instrument. Ultraviolet (UV) laser pulsing mode with laser energy ~ 20 nJ is utilized. Analysis of the tomographic data has been performed using TAP3D software. We have used shank angle method for APT reconstruction. SEM micrographs are utilized to calibrate the initial tip radius for APT analysis. Further, the composition is determined by cross interface computation method in TAP3D software. For this calculation, we have used the standard profile with distance class size of 5000 atoms. For the precipitate composition, we have determined the average of ten different points far away from the interface and calculated the standard deviation.

SANS experiments have been carried out at D22 SANS facility at the Institute Laue Langevin (ILL) Grenoble, France, using an incident neutron wavelength of $\lambda = 0.6$ nm. Scattering signal has been recorded as a function of the scattering vector q at room temperature, where $q = 4\pi\sin\theta/\lambda$, 2θ is the scattering angle and λ is the wavelength of the probe. The SANS measurements are performed with the following detector distances: 2 m and 10 m, in order to obtain the SANS signal over the desired range of scattering vectors.

4.3 SANS analysis details

It is essential to choose an appropriate model for accurate analysis of SANS data. Based on the existing literature [12-15], a spherical particle model is used to fit the SANS scattering profiles during analysis. The scattering intensity for non-interacting polydisperse precipitates can be expressed as [16]:

$$I(q) = N_p\ (\Delta\rho)^2 \int P(q,R) D(R) V^2(R) dR \quad \ldots\ldots\ldots\ldots..(4.1)$$

where, N_p is the number density of the precipitates, $\Delta\rho$ is the difference between scattering length densities of the precipitates and the matrix. V(R) and P(q,R) are volume and form factor of the precipitates having radius R, respectively. D(R) is the size distribution and D(R)dR is the probability that the radius of the precipitates is between R and R+dR. For a spherical precipitate, form factor P(q,R) is given by [17-18] :

$$P(q,R) = 9\left[\frac{\sin(qR) - qR\cos(qR)}{(qR)^3}\right]^2 \quad \ldots\ldots\ldots\ldots\ldots..\ (4.2)$$

The size distribution of the precipitates is assumed to be of log-normal type [19] :

$$D(R) = \frac{N}{R\sigma\sqrt{2\pi}} e^{-\frac{[ln(R/\mu)]^2}{2\sigma^2}} \quad \ldots\ldots\ldots\ldots..(4.3)$$

where, μ is the median radius, N is a normalization factor and σ is the polydispersity index. As mentioned before, all the scattering profiles corresponding to different aging times are fitted with this spherical particle model.

Further, the precipitate number density can be estimated from the scattering profile using the following relationship [20]:

$$N_p = \frac{k}{L_p^3} \quad \ldots\ldots\ldots\ldots\ldots\ (4.4)$$

where, k is $\sqrt{2}$ and L_p is the interparticle distance.

The total integrated scattered intensity is related to the volume fraction of the precipitates and is given by [6]:

$$Q = \int_0^\infty I(q)\, q^2 dq \ = \ 2\,\pi^2 (\Delta\rho)^2\ \phi\ (1-\phi) \quad \ldots\ldots\ldots\ldots\ldots\ (4.5)$$

where, ϕ is the volume fraction of the precipitates and Δρ is the scattering contrast. From eq.4.5, for small ϕ, Q is proportional to the volume fraction of the precipitates.

4.4 Results and Discussion

4.4.1 Microstructure, Thermal analysis and XRD analysis

Fe-1.4 at. % Cu alloy shows single-phase microstructure in as-solutionized condition as depicted in Figure 4.1. DSC result of as-solutionized sample is presented in Figure 4.2(a), where the sample is heated up to 923 K and cooled subsequently. The heating curve of the solutionized sample shows an exotherm that peaks at ~ 823 K corresponding to the precipitation process. The cooling curve, on the other hand, does not show any change in the heat flow, indicating completion of the precipitation process.

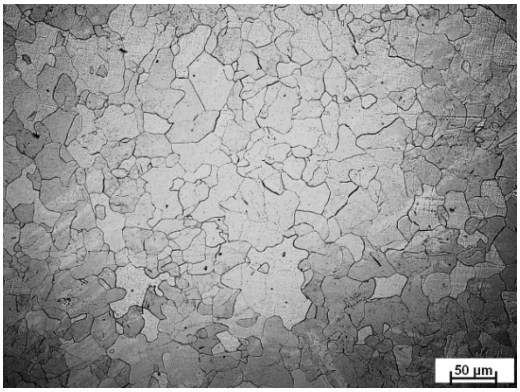

Figure 4.1. Optical micrograph of as-solutionized Fe-1.4 at. % Cu alloy.

4.4.2 Microhardness and magnetization measurements

The variation of micro-hardness with aging time for Fe-1.4 at. % Cu is depicted in Figure 4.2(b). It shows gradual increase in micro-hardness during initial aging followed by a steady decline on longer aging. Such decrease in micro-hardness on aging for longer duration is known to be associated with the coarsening of the CRPs [21]. Peak hardness is observed at 5 h of aging for this alloy. However, micro-hardness values for the aging durations 5 and 8 h are well within the respective error bars of each other. In all likelihood, coarsening of the CRPS in this alloy has started later than 8 h of aging.

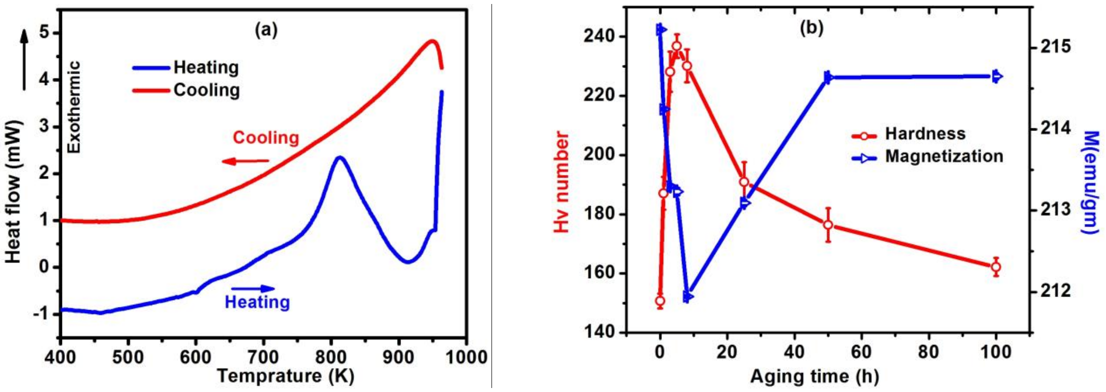

Figure 4.2. (a) DSC plot of as-solutionized Fe-1.4 at.% Cu showing the precipitation process. (b) Variation of micro-hardness and saturation magnetization on aging of Fe-1.4 at. % Cu with increasing aging duration.

The effect of aging time on saturation magnetization is displayed in Figure 4.2(b). Initially, the value of saturation magnetization decreases with aging, but rises steadily afterwards with longer aging time. The lowest magnetization is recorded after 8 h of aging time. Increase in magnetization when aged for durations longer than 8 h indicates initiation of the coarsening regime for the CRPs. Interestingly, the aging response of saturation magnetization (Figure 4.2(b)) of this alloy virtually mimics the reciprocal behaviour of the aging response of its micro-hardness (Figure 4.2(b)). Needless to mention, this change in mechanical and magnetic property with aging is directly related with the precipitate characteristics like its dimension, morphology and number density [22].

4.4.3 SANS analysis using spherical model

Representative scattering profiles are displayed in Figure 4.3. Results obtained from the analysis are tabulated in Table 4.1. The time evolution of mean radius of the precipitate is presented in Figure 4.4(a) and the corresponding size distribution is shown in the inset of Figure 4.4(a).

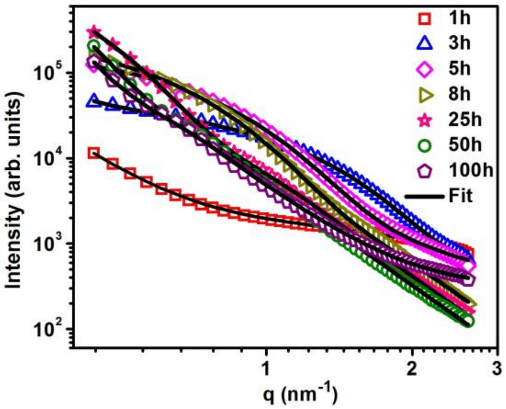

Figure 4.3. Represents SANS profile of Fe-1.4 at.% Cu alloy aged at 773 K for different time durations. Solid lines represent the corresponding spherical (1 h to 8 h) and ellipsoid (25 h onwards) model fits to the data.

The temporal dependency of mean radius for the aging durations from 1 to 8 h is found to be $t^{0.7(0.05)}$; it becomes $t^{0.34(0.1)}$ for the aging durations of 25 h and longer. This temporal dependency of mean radius after 25 h of aging appears to correspond to coarsening of the precipitates. The mean radius kinetics very nearly obey $t^{1/3}$ power law predicted by LSW [23] model for coarsening. It may be noted that this result corroborates well with hardness and magnetization results (Figure 4.2(b)), both of which indicate initiation of coarsening at 25 h of aging.

The precipitate number density is calculated using eq. 4.4 and its variation with aging duration is shown in inset of Figure 4.4(b). Number density is found to be high during initial stages of aging, however it declines rapidly with further aging. As for the number density, we observe a temporal dependency of $t^{-1.2(0.1)}$, which is slightly larger than the value of –1 predicted by LSW model [24], indicating a faster rate of coarsening.

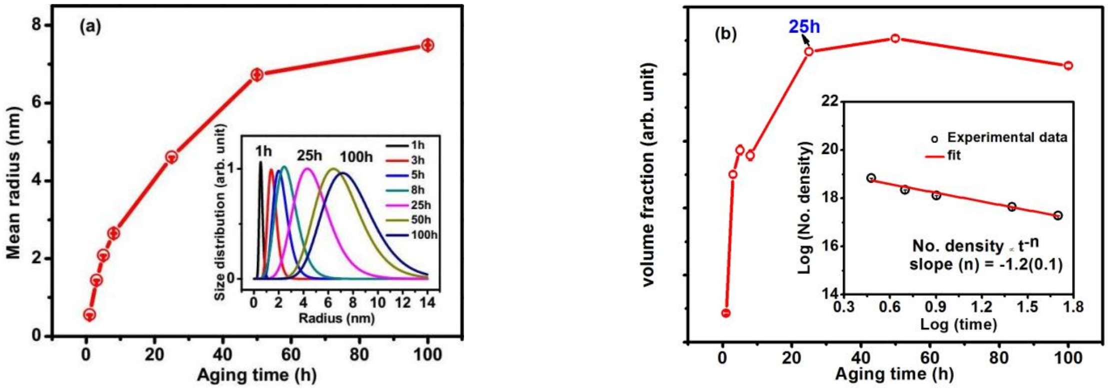

Figure 4.4. (a) Temporal variation of mean radius of CRPs; inset represents the size distribution of CRPs. (b) Temporal variation of volume fraction of CRPs; inset shows the number density variation with aging. Temporal exponent of number density is given by slope of linear fit which is displayed in inset.

By using eq. 4.5, the qualitative value of volume fraction of the CRPs is calculated and is depicted in Figure 4.4(b). It is evident that the volume fraction increases progressively with increasing aging duration up to 25 h and, remains virtually constant afterwards. It implies that the coarsening regime starts at 25 h of aging, which is consistent with the previously determined time dependency of mean radius as well as the microhardness and magnetization results (Figure 4.2(b)). In order to get insight into the concurrent temporal evolution of microstructure and also, in view of the significant variation in the shape of the scattering profiles corresponding to different aging durations (Figure 4.3), area under each scattering curve is calculated and plotted in Figure 4.5. At first it shows an increase up to 8 h and afterwards, a sudden drop in the area is observed. To elucidate it further, the variation of model independent Guinier radius with aging time is calculated and plotted in inset of Figure 4.5. A sudden change in the slope of the radius profile is noticed clearly after 8 h of aging, which is a credible manifestation of an underlying phenomenon occurring at this point. This warrants further investigation and APT is an appropriate technique in this length-scale, as discussed in the next sub-section.

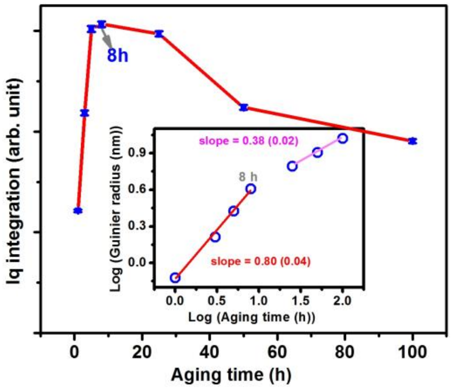

Figure 4.5. Displays variation of area under the scattering curves with aging time, which unambiguously shows a sudden variation after 8 h of aging; inset represents variation of model independent Guinier radius with aging time.

4.4.4 APT analysis

Figure 4.6(a) shows a representative atom map of a solutionized sample. Only Cu atoms (in blue) are displayed for clarity; they are found to be uniformly distributed throughout the analysis volume. As expected, uniform distribution is also noted for the Fe atoms in as-solutionized condition as well as in the aged samples. The bulk composition of the solutionized sample agrees well with the nominal composition of the alloy. The temporal evolution of the CRPs is seen in Figure 4.6(b-h) for all the aging durations, containing approximately 10 M atoms in each dataset. CRPs are delineated with 10 at. % Cu iso-concentration surfaces for all the aging durations. These figures illustrate that, the morphology of the CRPs is clearly spherical up to 8 h of aging. Morphological transformation of the CRPs with further aging is quite remarkable; 25 h onwards, they transform from spherical to oblate ellipsoidal ones (Figure 4.7).

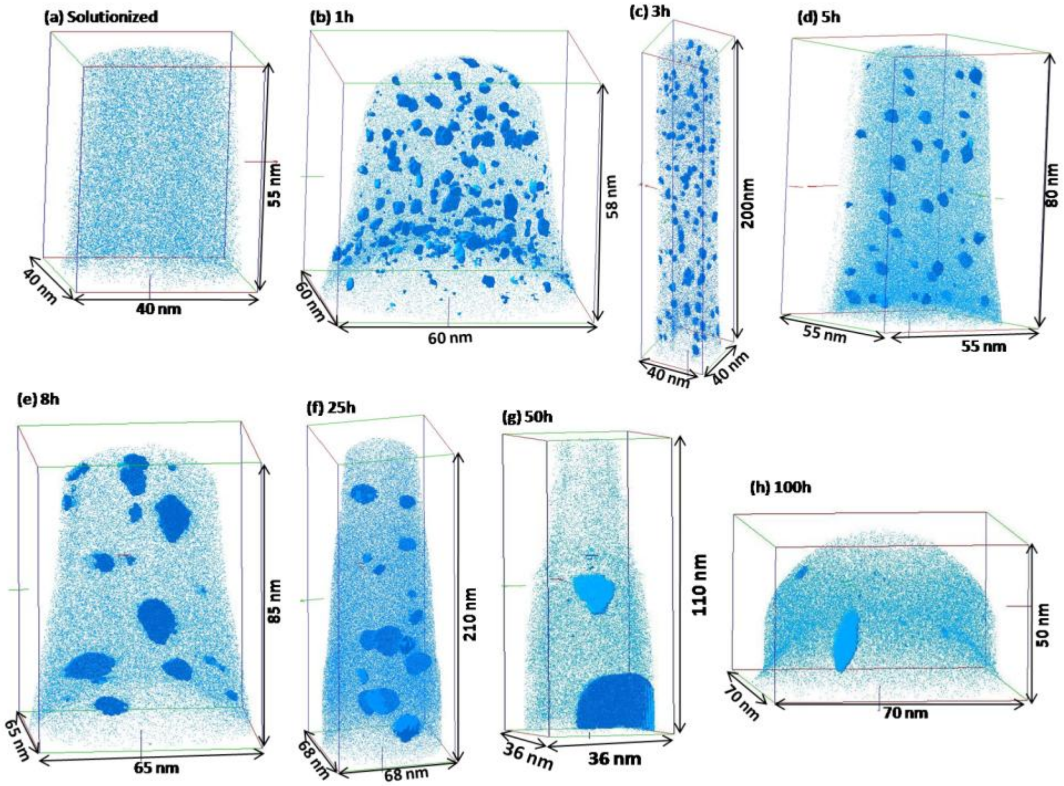

Figure 4.6. Displays APT reconstructed iso-concentration surfaces of Cu in (a) as-solutionized (b) 1 h (c) 3 h (d) 5 h (e) 8 h (f) 25 h (g) 50 h (h) 100 h . Only Cu atoms are displayed here in blue color. The CRPs are delineated by 10 at. % Cu iso-concentration surfaces.

Interestingly, this morphological transition at 25 h of aging appears to coincide with the initiation of their coarsening stage. At this juncture, it is worthy to mention that signature of this morphological transition clearly manifests itself in the scattering data as well. In all likelihood, this morphological transition is the reason behind the peculiar behaviour of (i) the plot of the area under the scattering curves (Figure 4.5); and (ii) the slope variation of Guinier radius (inset of Figure 4.5). The average size and chemical compositions of the CRPs are determined from the APT analysis for all the aging durations and are listed in Table 4.1. The number density of the CRPs calculated from the APT analysis shows progressive decline with aging time (Figure 4.8) and records a temporal dependency of $t^{-2(0.2)}$, which again indicates a faster rate of coarsening than the one predicted by the LSW model.

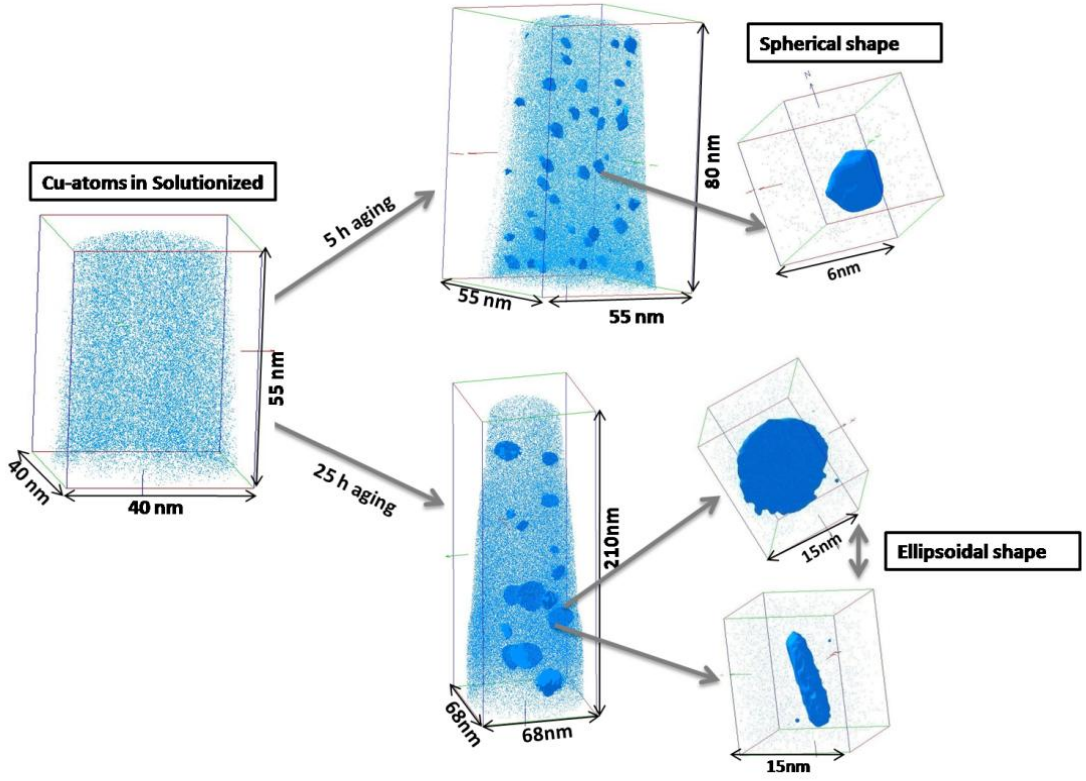

Figure 4.7. Displays APT reconstructed iso-concentration surfaces of Cu in as-solutionized, 5 h, 25 h. Only Cu atoms are displayed here in blue color. The CRPs are delineated by 10 at. % Cu iso-concentration surfaces. This depicts direct evidence of morphological transition from spherical to ellipsoid shape with aging.

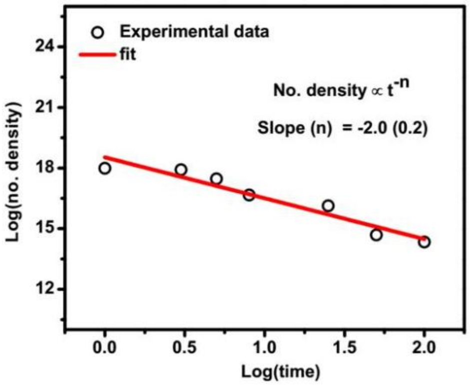

Figure 4.8. Depicts temporal evolution of number density of precipitates from APT analysis. Temporal exponent of number density is given by slope of linear fit which is displayed in figure.

4.4.5 SANS analysis using ellipsoidal model

As it is clear from the APT analysis that the precipitates morphology is oblate ellipsoid after 25 h of aging, SANS analysis is revisited and the data corresponding to the aging durations of 25 h and longer are fitted again using an oblate ellipsoid model. To the best of the authors' knowledge, this is the first such attempt to incorporate the morphological transition in SANS analysis of aging behaviour in Fe-Cu alloys. Parameters obtained after this analysis are also listed in Table 4.1. In addition, the equivalent sphere radius is calculated in order to get the temporal dependencies of radius and we observe a dependency of $t^{0.39(0.03)}$ for 25 h onwards, which is close to the LSW model [24] predictions. Figure 4.9 represents the equivalent spherical radius of precipitates with aging obtained by spherical particle model, ellipsoid particle model and APT analysis. It can be noted (Figure 4.9) that up to 8 h of aging precipitates dimension calculated by all three above-mentioned method is the same and afterwards, APT is found to agree with the ellipsoid model instead of spherical model.

Table 4.1. Temporal evolution of dimensions of Cu-precipitates and its compositional evolution extracted from APT and SANS analysis.

	SANS analysis (Spherical model)	**APT Analysis**				**SANS analysis (Ellipsoidal model)**	
	Diameter (nm)	**Cu content of CRPs (at.%)**	**Size (nm)**		**Shape**	**Size (nm)**	
			Major axis	**Minor axis**		**Major axis**	**Minor axis**
1	**1.1 ± 0.01**	**27.6 ±0.95**	**1.5 ± 0.3**	**1.5 ± 0.3**	**⇨ Sphere ⇦**	**1.1 ± 0.01**	**1.1 ± 0.01**
3	**2.9 ± 0.01**	**44.5 ±0.75**	**3 ± 0.6**	**3 ± 0.6**		**2.9 ± 0.01**	**2.9 ± 0.01**
5	**4.1 ± 0.01**	**69 ±1.01**	**4.5 ± 0.8**	**4.5 ± 0.8**		**4.1 ± 0.01**	**4.1 ± 0.01**
8	**6.8 ± 0.01**	**71.2 ±0.87**	**8.1 ± 0.7**	**8.1 ± 0.7**		**6.8 ± 0.01**	**6.8 ± 0.01**
25	**9.2 ± 0.01**	**73.1 ±2.5**	**12.9 ± 2.1**	**6.5 ± 1.2**	**⇨ Ellipsoid ⇦**	**13.2 ± 0.01**	**7.2 ± 0.01**
50	**13.5 ± 0.01**	**75.2 ±1.5**	**19**	**9.5**		**17.8 ± 0.01**	**10.3± 0.01**
100	**15.1 ± 0.01**	**78.8 ±0.68**	**24**	**11**		**23.5 ± 0.01**	**12.4± 0.01**

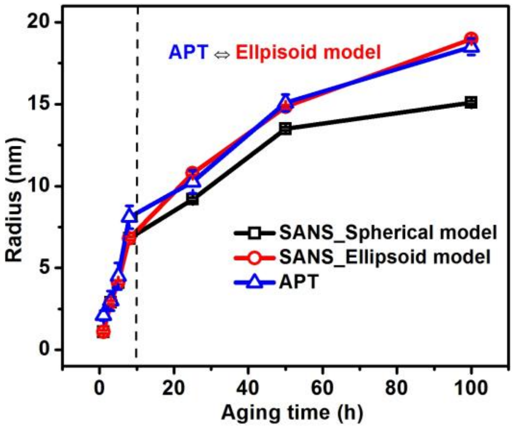

Figure 4.9. Depicts temporal evolution of equivalent spherical radius of precipitates from SANS analysis (spherical model and ellipsoid model) and APT analysis.

4.4.6 Discussion

Thermal aging of Fe-1.4 at. % Cu alloy at 773 K creates CRPs resulting in age-hardening which is clearly manifested in the (i) microhardness plot as well as in the (ii) magnetization plot (Figure 4.2(b)). Interestingly, the aging response of microhardness and saturation magnetization is virtually reciprocal of each other. Particularly striking is their response after approximately 8 h of aging: while the microhardness shows its maxima, the saturation magnetization records minima at the same point. It is well known that the interaction between dislocation motion and the strain field around the CRPs explains the change in microhardness with increasing aging time. The CRPs act as obstacles to dislocation motion, efficacy of which depends on the size and the number density of such obstacles. They offer more effective hindrance to dislocation motion below their critical size, above which the coherent bcc-Cu precipitates are known to undergo phase transformation to incoherent 9R structure due to structural instability [25]. At this stage of precipitation, number density of the CRPs (obstacles) is also reduced due to coarsening, resulting in the decrease in hardness for higher aging times. This behaviour of microhardness variation with aging time (Figure 4.2(b)) has also been observed in earlier reports [2,26].

On the other hand, variation of saturation magnetization in thermally aged Fe-Cu alloys indicates possible hindrance of magnetic domain wall motion by the CRPs. It is already known from literature that the magnetic domain wall interacts with local micro stress field present around the precipitates [27]. There has been molecular dynamics study [28] that shows that the micro stress field depends on the precipitate size and also on the coherency of the precipitates. In addition, for longer aging durations, the domain wall mobility impediment starts to decrease due to reduction in the precipitate number density. Quite evidently, the microstructure has a direct bearing on the aging response of both microhardness and saturation magnetization of the Fe-Cu samples.

Further, SANS experiments are carried out on as-solutionized as well as aged samples in order to obtain statistically-averaged information. At first, based on the existing literature, a polydisperse spherical particle model is used to fit the SANS scattering profiles. The temporal dependencies of mean radius and number density of the CRPs are consistent with the LSW model; both these results indicate presence of a coarsening regime after 25 h of aging. This is further supported by the constancy of volume fraction of the CRPs for aging for 25 h and longer (Figure 4.4(b)). However, one of the most striking features of this analysis is the appearance of a particularly unusual behaviour in the plots of area under the scattering curves (Figure 4.5) and the slope variation of Guinier radius (inset of Figure 4.5) after 8 h of aging. As mentioned earlier, this could be explained by the significant morphological change in the CRPs occurring during this aging duration. The APT analysis shows unambiguously this morphology transition of the CRPs from spherical to oblate ellipsoidal after 8 h of aging. Earlier, Othen *et al*. [7] attributed this morphological transformation to the 9R-3R invariant-plane-strain structural transformation caused by passage of partial dislocations. The shear associated with the partial dislocations reportedly caused the shape change of the precipitates. It is also observed from the atom maps that the number density of the CRPs starts decreasing at that point which is consistent with our hardness and magnetization results. It should be pointed out that the time power-law exponent of number density calculated using SANS is closer to LSW model than what we got from the APT analysis. This difference might have arisen because of the fact that unlike APT, SANS provides statistically-averaged information (inset of Figure 4.4(b) & Figure 4.8)).

In light of the additional findings, the scattering data corresponding to aging for 8 h and longer are fitted once again using ellipsoid model in order to obtain more accurate analysis of the precipitates. To the best of the authors' knowledge, incorporation of this morphological transition in SANS analysis of precipitation in Fe-Cu alloy, is the first such effort. It may also be noted that there has not been any studies in the literature that combines APT and SANS techniques in order to investigate the morphological transition of the precipitates in aged binary Fe-Cu alloys. In this connection, it is necessary to mention the report by Osamura *et al.* [12], who studied Fe-1.41Cu-0.27Ni-0.25Mn at. % quaternary alloy aged at 773 K and 823 K for up to 30 h. Based on TEM analysis, they reported presence of ellipsoid precipitates after aging for 30 h, but, still used spherical particle model in their SANS analysis, ostensibly for simplicity.

As for the shape of the precipitates, the equilibrium morphology is known to be controlled by the relative contribution of interfacial (E_{in}) and strain energy (E_s) [29] to the total system energy. The morphological transition during growth of a precipitate is observed when the shape that minimizes the interfacial energy is different from that which minimizes the strain energy. The ratio i.e. E_{in}/E_s is given as [30]:

$$\xi = \frac{E_{in}}{E_s} = \frac{\gamma_s S_p}{\lambda \varepsilon_0^2 V_p} \quad \text{....................} \ (4.6)$$

where γ_s, S_p, λ, ε_0, V_p are specific interfacial energy, surface area of the precipitate, elastic modulus, stress-free transformation strain, and volume of the precipitate, respectively. If for simplicity, the following: γ_s, λ and ε_0 are assumed to be constant, therefore ξ can be qualitatively calculated using surface to volume ratio of the precipitates. The ratio S_p/V_p can be calculated using scattering data without assuming any specific model for the precipitates. Surface to volume ratio can be estimated from the scattering data using the following relationship [18]:

$$\frac{S_p}{V_p} = \pi \frac{Lt_{q\to\infty} I(q) q^4}{\int_0^{\infty} I(q) q^2 dq} \quad \text{............................} \ (4.7)$$

where, the limiting value of $I(q)q^4$ can be calculated from Porod plot of the scattering curves. This ratio qualitatively represents the ratio between the energies, ξ. The variation of ξ with aging time is presented in Figure 4.10, the plot clearly depicts that during initial aging duration E_{in} is more dominant over E_s, which diminishes rapidly, whereas E_s becomes more dominant with increasing size of the precipitates. Interestingly, aging time corresponding to the morphological transition matches with this transition as well (Figure 4.7).

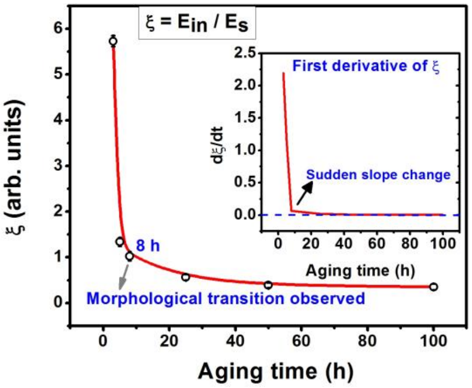

Figure 4.10. Variation of ratio between interfacial energy and strain energy with aging duration and inset shows the change in slope of interfacial to strain energy ratio.

In summary, the nanometre-scale CRPs appreciably influence the bulk properties such as the microhardness and the saturation magnetization of the Fe-Cu binary alloys. The CRPs, as seen in the present investigation, obeys the LSW model asymptotic temporal power laws. More specifically, the temporal power-law exponent determined from SANS analysis for the number density of the CRPs is -1.2(0.1), which is slightly larger than the value predicted by the LSW model. The temporal exponent for the mean radius is in good agreement with the predicted value of 1/3. The experimental evidence reveals that the morphology of the CRPs transforms from spherical to oblate ellipsoid at longer aging durations. Indication for this intermediate morphological transformation is present in the scattering data as well. In our SANS analysis, ellipsoid model is considered wherever necessary in order to obtain accurate information about these nanometre-scale precipitates.

4.5 Summary

The combined use of APT and SANS reveals the morphological evolution of the CRPs during aging of Fe-Cu alloys and provided definitive evidence of the intermediate morphological change of the CRPs from spherical to ellipsoidal shape. This study draws necessary attention to this intermediate change of precipitate morphology and helps in bridging the knowledge gap. It is also shown that in spite of the complex morphological transformation during aging, the mean size and the number density of the CRPs follow the LSW model fairly well, an analysis that could only be achieved by correlating APT with SANS technique. The derived conclusions are as follows:

1. Direct evidence of the intermediate morphological transition of CRPs from spherical to ellipsoid, after 8 h of aging, is revealed by APT. Further, Cu-content in the precipitates enhances significantly with aging duration.

2. The evidence for the morphological transition of the CRPs is detected unambiguously for the first time, by SANS analysis as well. Temporal dependence of mean precipitate size follows $\sim t^{0.39}$ behaviours in contrast to that predicted by classical LSW model ($t^{0.33}$) for aging time between 8 h to 100 h. This supports the observed evolution of microhardness and magnetization.

3. The temporal evolution of number density obtained from SANS and APT corresponds to $t^{-1.2(0.1)}$ and $t^{-2.0(0.2)}$, respectively, indicating a faster rate of coarsening as compared to the simple diffusion limited coarsening mechanism.

References

[1] S. R. Goodman, S. S. Brenner, and J. R. Low, Metallurgical Transactions **4**, 2371 (1973).

[2] S. M. He, N. H. van Dijk, M. Paladugu, H. Schut, J. Kohlbrecher, F. D. Tichelaar, and S. van der Zwaag, Physical Review B **82**, 174111 (2010).

[3] Y. Le Bouar, Acta Materialia **49**, 2661 (2001).

[4] J.-H. Shim, Y. W. Cho, S. C. Kwon, W. W. Kim, and B. D. Wirth, Applied Physics Letters **90**, 021906 (2007).

[5] A. Biswas, D. Sen, S. K. Sarkar, Sarita, S. Mazumder, and D. N. Seidman, Acta Materialia **116**, 219 (2016).

[6] F. De Geuser and A. Deschamps, Comptes Rendus Physique **13**, 246 (2012).

[7] P. J. Othen, M. L. Jenkins, and G. D. W. Smith, Philosophical Magazine A **70**, 1 (1994).

[8] B. L. CHEN, W. WANG, H. XIE, R. R. GE, Z. Y. ZHANG, Z. W. LI, X. Y. ZHOU, and B. X. ZHOU, Journal of Microscopy **262**, 123 (2016).

[9] R. Monzen, M. Iguchi, and M. L. Jenkins, Philosophical Magazine Letters **80**, 137 (2000).

[10] R. Monzen, K. Takada, and C. Watanabe, ISIJ International **44**, 442 (2004).

[11] E. Hornbogen, Acta Metallurgica **10**, 525 (1962).

[12] K. Osamura, H. Okuda, K. Asano, M. Furusaka, K. Kishida, F. Kurosawa, and R. Uemori, ISIJ International **34**, 346 (1994).

[13] A. Deschamps, M. Militzer, and W. J. Poole, ISIJ International **41**, 196 (2001).

[14] M. K. Miller, B. D. Wirth, and G. R. Odette, Materials Science and Engineering: A **353**, 133 (2003).

[15] M. Schober, E. Eidenberger, P. Staron, and H. Leitner, Microscopy and Microanalysis **17**, 26 (2011).

[16] J. Pedersen, Journal of Applied Crystallography **27**, 595 (1994).

[17] D. Sen, O. Spalla, L. Belloni, T. Charpentier, and A. Thill, Langmuir **22**, 3798 (2006).

[18] G. F. A. Guinier, B.C. Walker, L.K. Yudowith, Wiley, New York (1955).

[19] J. A. C. B. J. Aitchison, Cambridge University Press (1957).

[20] K. Osamura, H. Okuda, S. Ochiai, M. Takashima, K. Asano, M. Furusaka, K. Kishida, and F. Kurosawa, ISIJ International **34**, 359 (1994).

[21] M. Perez, F. Perrard, V. Massardier, X. Kleber, A. Deschamps, H. de Monestrol, P. Pareige, and G. Covarel, Philosophical Magazine **85**, 2197 (2005).

[22] L. P. Vandenbossche, M. J. Konstantinović, A. Almazouzi, and L. R. Dupré, Journal of Physics D: Applied Physics **40**, 4114 (2007).

[23] I. M. Lifshitz and V. V. Slyozov, Journal of Physics and Chemistry of Solids **19**, 35 (1961).

[24] A. Umantsev and G. B. Olson, Scripta Metallurgica et Materialia **29**, 1135 (1993).

[25] H. Kikuchi, T. Onuki, Y. Kamada, K. Ara, S. Kobayashi, and S. Takahashi, Journal of Magnetism and Magnetic Materials **310**, 2886 (2007).

[26] S. R. Goodman, S. S. Brenner, and J. R. Low, Metallurgical Transactions **4**, 2363 (1973).

[27] F. M. Kronmuller H, Micromagnetism and the
Microstructure of Ferromagnetic Solids (Cambridge:
Cambridge University Press) (2003).

[28] S. Y. Hu, Y. L. Li, and K. Watanabe, Modelling and Simulation in Materials Science and Engineering **7**, 641 (1999).

[29] K. R. Wagner R, Voorhees PW, Weinheim: Wiley-VCH, 309 (2001).

[30] D. Y. Li and L. Q. Chen, Acta Materialia **45**, 2435 (1997).

Chapter 5

On the Origin of Solute Precipitation in the Fe-Cu Alloy Using First Principle DFT Calculations

Although a good deal of experimental investigations on Cu precipitation and its morphological transition has been discussed in previous chapter, the very important microscopic, electronic origin of the Cu precipitate formation in Fe-Cu alloy is yet to be fully understood. Therefore, we have used first-principle DFT calculations to understand the reason behind such precipitate formation by different solute atoms (mainly Cu and Ni) in the Fe matrix and the details of this investigation has been described in this chapter. We unravel the nature of interactions of point defects (vacancy (V) or di-vacancy) and solute atoms (mainly Cu and Ni) in bcc-Fe lattice. One of the very novel features of the present investigation is to demonstrate the importance of distortion energy-electronic energy compensation in stabilizing the formation of solute (Cu, Ni) clusters in ferritic steel.

5.1 Introduction

The importance of Cu precipitate formation in RPV steel in terms of its structural integrity is already discussed in chapter 2. Further, it is revealed from experimental observations that the addition of Ni to binary Fe-Cu alloys accelerates the Cu precipitation process [1] and Ni also segregates around the Cu precipitates [2]. In addition, the interaction strength among irradiation induced point defects and solute atoms is known to control the precipitation process. Therefore, in this chapter, using first-principle electronic structure calculations within the framework of DFT, the nature of interactions of point defects (vacancy (V) or di-vacancy) and solute atoms (mainly Cu and Ni) in bcc-Fe lattice is revealed. There are only a few studies in recent times on the heavy solute atom interaction with point defects in bcc-Fe [3-8] as discussed in section 2.4.5 of chapter 2. All the previous studies have mainly concentrated on the interaction behavior of solute atoms rather than the origin of such interaction behavior. Whenever a vacancy or an interstitial is generated, the point-defect interaction is governed by two primary factors, namely, distortion effect and electronic effect [9]. For some materials, both the factors are important in deciding the interaction behavior, whereas, for others, one of these two effects plays a major role. Therefore, understanding the fundamental mechanisms behind these fine interactions is very crucial to develop predictive model of evolution in microstructure and mechanical properties of Fe-based materials.

In this chapter, we use DFT to perform a systematic investigation of interaction among the solute atoms (Cu/Ni) themselves and their interactions with irradiation induced point defects (mainly vacancies) in the bcc-Fe lattice. The interaction between irradiation induced defects and solute atoms (Cu/Ni) are studied in detail to obtain the binding energy of different complexes. Moreover, the origin of the binding energy is discussed from the view point of two governing factors i.e. distortion effect and electronic effect, which, to the best of author's knowledge, are studied for the first time in this system. It is observed that the distortion and electronic effects, being opposite in nature in most of the cases studied here, a fine balance between them decides the binding energy for both solute (Cu/Ni) atoms in the bcc-Fe lattice. The nature of Cu-Cu and Cu-Ni interactions and binding energies of V-Cu_n and V-Ni_n clusters provides fundamental understanding of the influence of irradiation induced defects on the solute aggregation in the bcc-Fe lattice.

5.2 Computational details

5.2.1 First-principle calculations

The DFT calculations have been performed using the Vienna ab-initio simulation package (VASP) [10] within the generalized gradient approximation based on Perdew-Burke-Ernzerhof functional [11]. These calculations used the projector augmented-wave method [12] to treat the ion-electron interactions and plane wave basis set with a kinetic energy cutoff of 500 eV to expand the electronic wave functions. We considered a 3×3×3 supercell containing 54 Fe-atoms for bcc-Fe (in a defect free state) to investigate the interaction among the solute atoms (SA) (Cu, Ni) and their interaction with vacancies. The Monkhorst-Pack scheme is utilized to generate the K-points to sample the Brillouin zone. A 6×6×6 K-point grid is chosen for bcc-Fe. The spin-polarization is incorporated during the calculations to consider the magnetism in bcc-Fe lattice, the structures are optimized by relaxing supercell shape and volume as well as all atomic positions.

The formation enthalpy for a supercell containing N-atoms of Fe and one SA is defined as [13]:

$$E^f(SA)_{Fe} = E(Fe_N\text{-}SA) - NE(Fe) - E(SA) \quad \ldots\ldots\ldots\ldots\ (5.1a)$$

Similarly, we define the formation energy of a Fe-A_1-A_2-A_3-….A_n complex as

$$E^f(Fe\text{-}SA_1\text{-}SA_2\ldots SA_n) = E(Fe_N\text{-}SA_1\text{-}SA_2\ldots.\text{-}SA_n) - NE(Fe) - [\textstyle\sum_{i=1}^{n} E(SA_i)] \quad \ldots\ldots\ldots\ldots\ (5.1b)$$

where, SA_1, SA_2, ….SA_n are solute atoms, E(Fe_N-SA) is the total energy of the supercell containing N atoms of Fe and one SA (SA = Cu or Ni), E (Fe) is the energy per atom of the defect free Fe host with bcc structure, and E(SA) is energy of the isolated SA. The terms E(Fe_N-SA_1-SA_2….-SA_n) and E(SA_i) in eq. 5.1(b) are the total energy of the supercell with N Fe atoms and SA_i (*i=1,n*) solute atoms and that with single SA_i solute atom respectively.

The formation energy of m-vacancies is calculated as[14]:

$E^{f}_{vac}(m) = E(Fe_{(N-m)}) - \left(\frac{N-m}{N}\right)E(Fe_{N})$……….(5.2)

Where $E^{f}_{vac}(m)$ is the formation energy of m-vacancy in Fe lattice, $E(Fe_{(N-m)})$ and $E(Fe_{N})$ are total energy of the supercell containing N-m and N Fe-atoms respectively.

For a supercell containing n-interacting entities (A1,A2….A_n)(for n>=2), the binding energy between the interacting entities in matrix is calculated as follows[13]:

$E_b(A_1, A_2, \ldots, A_n) = [\sum_{i=1}^{n} E(A_i)] - [E(A_1 + A_2 + \ldots + A_n) + (n-1)E_{ref}]$ ……. (5.3)

where, $E(A_i)$ is the energy of the supercell containing entity A_i only, $E(A_1 + A_2 + \ldots + A_n)$ is the energy of the supercell containing all n-entities, E_{ref} is the energy of Fe supercell without any entity. Here, a positive binding energy indicates attraction between these entities, whereas a negative binding energy denotes repulsion. The above equation can be easily understood as the difference between the sum of energies ($\sum_{i=1}^{n} E(A_i)$) of *n* individual non-interacting Fe-A_i systems and the sum of energies $[E(A_1 + A_2 + \ldots + A_n) + (n-1)E_{ref}]$ of the resulting complex and the remaining Fe lattices. The $(n-1)E_{ref}$ is coming because when *n* iron lattices with one A_i entity in each lattice reacts to give one Fe complex with all A_i entities in it, remaining (n-1) pure iron lattices will also be created.

We decompose the total binding energy into distortion binding energy ($E^{d}_{b}(VX_n)$) and electronic binding energy ($E^{e}_{b}(VX_n)$) in order to obtain the information about its origin[9] :

$E^{T}_{b}(VX_n) = E^{d}_{b}(VX_n) + E^{e}_{b}(VX_n)$ ……….. (5.4)

$E^{d}_{b}(VX_n)$: is the energy that can be gained by reducing the distortion in host matrix when all defects combine to form a complex. This can be further written as:

$E_b^d(\mathrm{VX_n}) = \mathrm{n}{*}\mathrm{E_d}(\Lambda_X^{Fe}) + \mathrm{E_d}(\Lambda_V^{Fe}) - \mathrm{E_d}(\Lambda_{VXn}^{Fe})$ ………… (5.5)

here, $\mathrm{E_d}(\Lambda_X^{Fe})$, $\mathrm{E_d}(\Lambda_V^{Fe})$ and $\mathrm{E_d}(\Lambda_{VXn}^{Fe})$ are the distortion energies due to a solute atom (X), a vacancy (V) and a complex ($\mathrm{VX_n}$) respectively. Here, $\mathrm{E_d}(\Lambda_\alpha^{Fe})$ is defined as:

$\mathrm{E_d}(\Lambda_\alpha^{Fe}) = \mathrm{E}(\Lambda_\alpha^{Fe}) - \mathrm{K}\, E_{coh}^{Fe}$ ……….. (5.6)

where, K is the number of Fe atoms in Λ_α^{Fe} configuration and E_{coh}^{Fe} is the cohesive energy of pure Fe. $\mathrm{E}(\Lambda_\alpha^{Fe})$ is the energy of only Fe atoms in crystal containing Λ_α^{Fe} complex.

The electronic binding energy is the difference between Fe-X and X-X bonds before and after the formation of $\mathrm{VX_n}$ complex. This can be written as:

$E_b^e(\mathrm{VX_n}) = E_b^{Fe-X}(\mathrm{VX_n}) + E_b^{X-X}(\mathrm{VX_n}) - \mathrm{n}\, E_b^{Fe-X}(\mathrm{X})$ ………. (5.7)

where, $E_b^{Fe-X}(\mathrm{VX_n})$, $E_b^{X-X}(\mathrm{VX_n})$ and $E_b^{Fe-X}(\mathrm{X})$ are energies of Fe-X and X-X bonds in a crystal with a $\mathrm{VX_n}$ complex and Fe-X bond in a crystal with a substitutional X atom respectively, and are defined as follows:

$E_b^{Fe-X}(\mathrm{VX_n}) = \mathrm{E}(\Lambda_{VXn}^{Fe}) + \mathrm{E}(\Lambda_{VXn}^{X}) - \mathrm{E}(\Lambda_{VXn}^{Fe,X})$ ………… (5.8)

$E_b^{X-X}(\mathrm{VX_n}) = \mathrm{n\,E^c} - \mathrm{E}(\Lambda_{VXn}^{X})$ ………… (5.9)

$E_b^{Fe-X}(\mathrm{X}) = \mathrm{E}(\Lambda_X^{Fe}) + \mathrm{E^c} - \mathrm{E}(\Lambda_X^{Fe,X})$ ………… (5.10)

where, $\mathrm{E}(\Lambda_{VXn}^{X})$ and $\mathrm{E}(\Lambda_{VXn}^{Fe,X})$ are the energies of only X atoms in Λ_{VXn}^{Fe}complex and total energy of Λ_{VXn}^{Fe}complex respectively. $\mathrm{E^c}$ is the energy of single solute atom X.

The binding volume for $\mathrm{VX_n}$ complex can be written as[9]:

$\mathrm{V_o}(\mathrm{VX_n}) = \{\mathrm{V_o}(\Lambda_{VXn}^{Fe,X}) + (\mathrm{n}{*}\,\mathrm{V_o}(\Lambda^{Fe}))\} - \{\mathrm{V_o}(\Lambda_V^{Fe}) + (\mathrm{n}{*}\mathrm{V_o}(\Lambda_X^{Fe,X}))\}$ ………… (5.11) where, $V_o(\Lambda_V^{Fe})$, $V_o(\Lambda_X^{Fe,X})$, $V_o(\Lambda_{VXn}^{Fe,X})$ and $V_o(\Lambda^{Fe})$ are volumes of a supercell containing a vacancy, a solute atom X, VX_n complex and pure Fe-lattice respectively. Here, a positive binding volume indicates lattice expansion, whereas a negative binding volume denotes lattice contraction. In all the notations mentioned above, the symbol Λ_Y^X meant that the system is Y, in which X is one of the components and $E(\Lambda_Y^X)$ denotes the energy of only X in a composite system consisting of X and other constituent atoms.

5.2.2 Verification of calculations

To verify the accuracy of our methods, we have calculated the vacancy formation energies in bcc-Fe and validated with the reported results from the literature. In Table 5.1, our calculated results are compared with the values from other first-principle and empirical calculations as well as experiments [4,15-18]. It can be observed that our calculated results are within the error bars of the experimental data and are consistent with results from other computational studies. The binding energies of the divacancy situated with respect to each other at the first nearest neighbour (1NN) and the second nearest neighbour (2NN) positions are also calculated and compared with other results. The present result for the bcc lattice is found to be in very good agreement with that of other calculations. The small deviation of our results from other first principle calculations is mainly due to cell relaxation. We relax the cell volume as well as cell shape, whereas other calculations are carried out under a constant volume condition. The positive value of the vacancy formation energy indicates that the vacancy formation is not energetically favourable in bcc-Fe systems. Although the interaction energy in case of divacancy at the second nearest neighbour with respect to each other is more than that at the first nearest neighbour in bcc iron. These calculation yielded the lattice parameter of 2.831Å for bcc-Fe, the value is in good agreement with experimental [19] and other theoretical results [20]. We have also calculated the elastic constant for pure bcc-Fe lattices. We obtain C_{11} = 295 GPa C_{12} = 161 GPa and C_{44} = 94 GPa in bcc-Fe lattice, these values are consistent with other theoretical [20-21] and experimental results [22].

Table 5.1. Formation energies (in eV) of Vacancy and divacancy (first and second nearest neighbor) in bcc-Fe.

Method	BCC Fe		
	Vacancy	Divacancy	
		1NN	2NN
EAM (Johnson and oh)[a]	1.73	0.16	0.22
US-GGA (PW91, constvol)[b]	2.09	0.17	0.23
US-GGA (PW91, constvol)[c]	2.02	0.15	0.29
PAW-PBE[d]	2.17	0.16	0.23
This work (PAW-PBE)	2.15	0.18	0.23
Experimental value[e,f]	2.0±0.2		

[a]Reference [9], [b]Reference [16], [c]Reference [4], [d]Reference [9], [e]Reference [15] , [f]Reference [18].

5.3 Results and Discussions

5.3.1. Stability of SA in bcc Fe matrix and the migration energy

We have calculated the formation enthalpy of solutes Cu and Ni at substitutional and interstitial (both octahedral and tetrahedral) positions by considering only one solute in the Fe matrix and the results are summarized in Table 5.2.From the energetics shown in Table 5.2 it is clear that both the solute atoms (Cu and Ni) are energetically stable at substitutional position, and it is in agreement with other theoretical results[4].

Table 5.2. Formation enthalpies (in eV) for single SA (Cu/Ni) in bcc-Fe matrix, positioned at either of the two different (octahedral and tetrahedral) interstitial sites or a substitutional site

Formation Enthalpies (eV)		
Configuration	Cu	Ni
Substitutional	-2.7903	-4.747
Tetrahedral	+1.908	-0.004
Octahedral	+2.4139	+0.5168

The diffusion of Cu and Ni atoms in bcc-Fe plays a key role in precipitation process; therefore we have computed the migration barriers for both solute atoms in bcc-Fe lattice. The migration energy is calculated using the standard climbing-image nudged-elastic-band (CINEB) method.In our calculations, we consider the SA hops to the 1NN position of substitutional site. For these calculations, we find a series of steps characterized by pairs of local minimum energy configurations. In our CINEB calculations, the migration path of substitutional migration is sampled with seven images. We have calculated the energy differences of the initial states with respect to normalized reaction coordinates (Figure 5.1(a) & (b)). The maximum energy along this path is recognized as migration energy. The similarity of initial and final states for the migration process is reflected by the symmetry of migration energies as shown in Figure 5.1(c). For Cu and Ni, migration barriers for substitutional mechanism are 0.51 and 0.64 eV respectively, which is in agreement with other theoretical results[4,23]. As evident from the Figure 5.1(c), smaller migration barrier for Cu atoms results in faster diffusion of Cu atoms than Ni atoms in bcc-Fe matrix, as a result of which sluggish movement of Ni atoms will be observed.

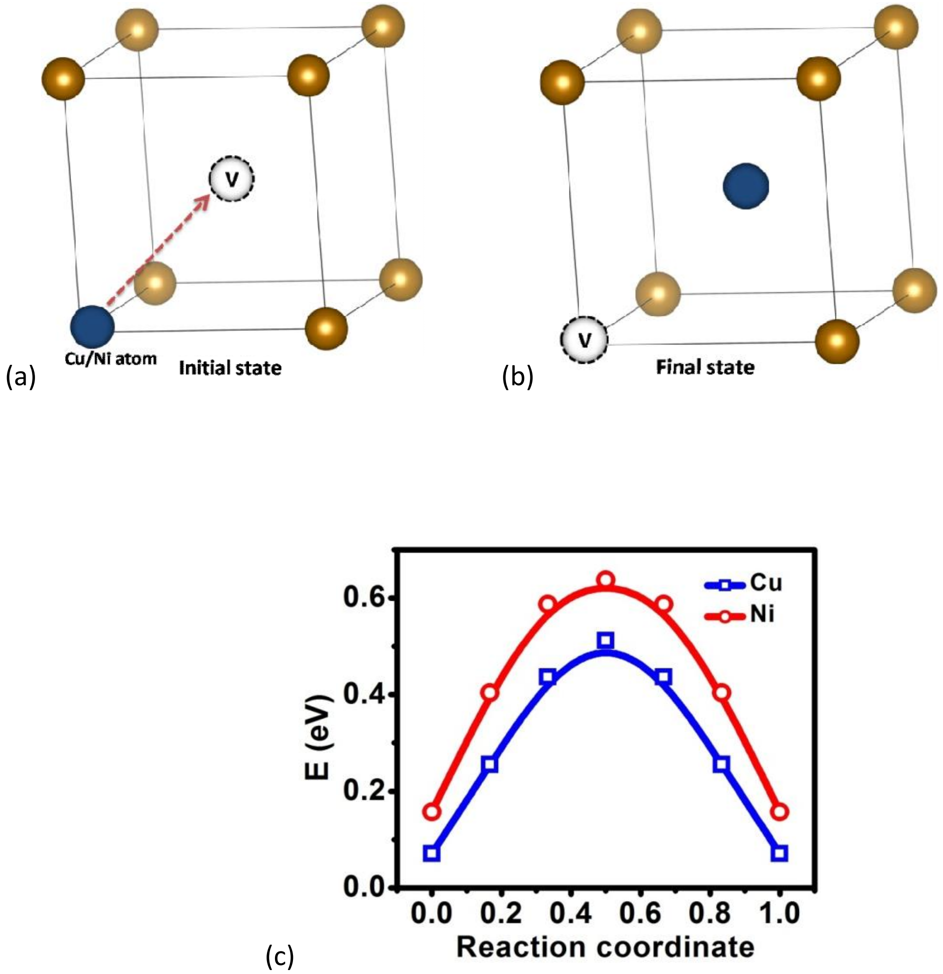

Figure 5.1. (a) Initial configuration for migration of a SA (Cu/Ni atom) from its initial position (blue circle at the corner) to the nearest vacancy (shown as circle at the body center) and the migration path as shown by an arrow in bcc-Fe lattice. **(b)** Final configuration for the same migration **(c)** Migration energies for jump of a Cu and a Ni atom from the initial to final configuration as shown in **(a)** and **(b)** respectively.

5.3.2 Solute-solute and vacancy-solute interactions

In order to understand the interaction behavior, Cu-Cu, Ni-Ni, V-Cu(Ni) and Cu-Ni interactions are investigated at different configurations. The binding energies of Cu-Cu and V-Cu complexes at different nearest neighbor positions are represented in Figure 5.2(a) and the studied configurations are shown in Figure 5.2(d).It is observed that Cu-Cu interactions are attractive at first nearest neighbor and becomes negligible afterwards as binding energy is close to zero. The attractive interactions between Cu atoms in the 1NN position probably causes Cu-clustering in bcc-Fe lattice, the fact which is observed experimentally [24].The strong attractive interaction between V-Cu is observed at first as well as second nearest neighbor and becomes negligible at larger distances. The reported experimental value for V-Cu binding energy is 0.14 eV [25] and from other calculation it is 0.11 eV [4]. Our result (0.13-0.2 eV depending on SA-V distance), which is obtained from more sophisticated calculation than that used in earlier calculation[4],lies in the experimental range. The attractive V-Cu interaction may be due to the fact that a vacancy next to the solute atom allows the system to relieve strain. The strong Cu-V interaction along with small Cu migration barrier is consistent with the fact that Cu diffuses faster than Ni in bcc-Fe lattice and the diffusion is via vacancy mechanism, as observed in earlier calculation [26].

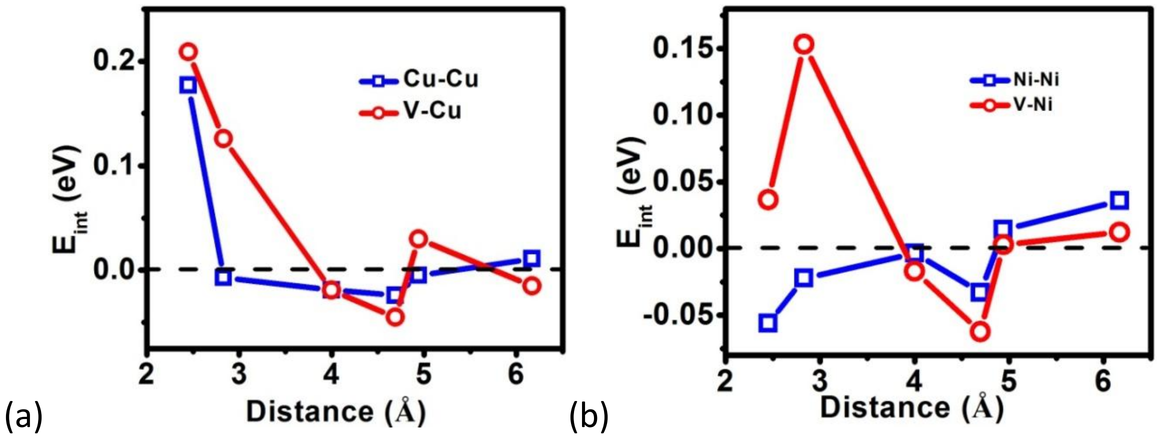

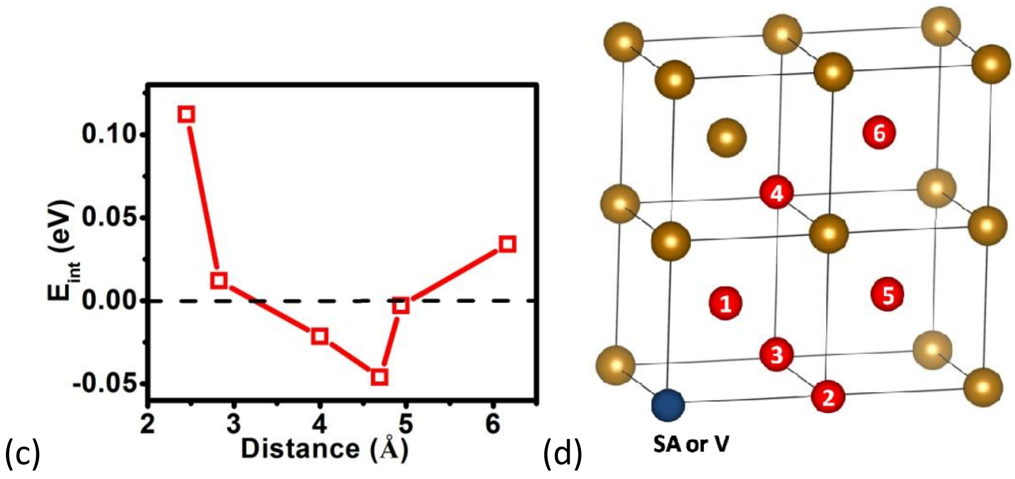

Figure 5.2. Binding energies of SA-SA and V-SA pairs as a function of the distance in bcc-Fe (a) Cu-Cu and V-Cu (b) Ni-Ni and V-Ni (c) Cu-Ni (d) represents the different investigated configurations for the studied complex.

The binding energies for Ni-Ni and V-Ni at different positions are depicted in Figure 5.2(b). It is observed that Ni-Ni interactions are slightly repulsive at shorter distances and becomes negligible afterwards, which implies that Ni solute atoms are not likely to aggregate in bcc-Fe lattice. Whereas, the interaction of V-Ni is more attractive at the second nearest neighbor than at the first nearest neighbor, in accordance with previous calculations [3] and experimental results [27].The interaction between V and Ni is negligible at larger distances. Further, it is observed that the interaction between V-Ni is weaker than that of V-Cu. Therefore, the combination of weaker V-Ni interaction and higher migration barrier results in sluggish Ni diffusion as compared to Cu diffusion in bcc-Fe lattice. During precipitation, as Cu atoms can move faster, it forms the core of the precipitate; whereas, Ni atoms will be at the periphery due to slow diffusion. Our explanation is in concurrence with experimental results [28]. Further, the binding energy between Cu-Ni is shown in Figure 5.2(c) at different Cu-Ni distances. The strong attractive interaction is observed between Cu-Ni at first nearest neighbor distances and becomes negligible at larger distances. This implies that the Cu-Ni atoms tend to agglomerate in bcc-Fe and this is consistent with the experimental results showing Cu-Ni clusters in bcc-Fe[28]. Interestingly, it is observed that the attractive interaction between Cu-Cu atoms is stronger than that between Cu-Ni atoms. This result provides theoretical justification of formation of Ni shell around the Cu-precipitates in bcc-Fe.

5.3.3 Binding energy of V-X_n clusters

In order to understand solute cluster formation tendency in presence of vacancy in a bcc-Fe matrix, the binding energy of V-X_n (X = Cu/Ni) cluster in the Fe matrix is investigated for *n* values upto 5. Different configurations with notations -1d, -2d, -3d (see right hand panel of Figure 5.3) represent relative vacancy-solutes spatial arrangements as one-, two- and three-dimensional respectively. The total binding energies of the V-X_n clusters are listed in Table 5.3 and the corresponding configurations are shown in Figure 5.3.

Complex	**Atom position**
V-X	**A**
V-X_2-1d	**A-F**
V-X_2-2d	**A-B**
V-X_3-2d	**A-D-F**
V-X_3-3d	**A-C-E**
V-X_4-2d	**A-B-D-F**

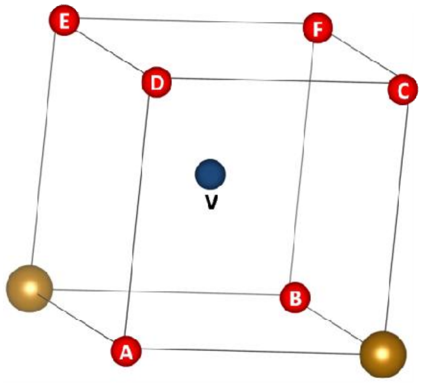

V-X$_4$-3d	**A-C-D-F**
V-X$_5$	**A-B-C-D-F**

Figure 5.3. Schematic representation of the investigated configurations for V-X$_n$ (X=Cu/Ni) clusters. (Here, gold color atoms are Fe atoms; red color atoms are solute atoms)

Table 5.3. Total binding energy (in eV) of V-X$_n$ (X=Cu/Ni) complex in bcc-Fe matrix. The -1d, 2-d and 3-d notations represent whether arrangement V and *n* X atoms are 1-dimensional (forming a line), 2-dimensional (forming a plane) or 3-dimensional.

Configuration	Cu	Ni
V-X	+0.21	+0.04
V-X$_2$-1d	+0.42	+0.09
V-X$_2$-2d	+0.45	+0.14
V-X$_3$-2d	+0.66	+0.29
V-X$_3$-3d	+0.71	+0.33
V-X$_4$-2d	+0.97	+0.49
V-X$_4$-3d	+0.88	+0.50

V-X$_5$	+1.22	-0.15

For substitutional Cu-atoms, the binding energy is positive for all the studied configurations indicating attractive interaction among the Cu atoms and vacancy and therefore it confirms the stability of the Cu complex inside the Fe matrix. Further, the binding energy is consistently increasing with number of Cu-atoms. It is very interesting to note that the total binding energy is not only dependent on the number of Cu-atoms but also on their specific arrangement in the lattice. For example, from the entries shown in Table 5.3,it is clear that complex V-X$_2$ can have two different configurations namely, V-X$_2$-1d, in which V and two solute atoms (X) lie in the same line forming a one-dimensional arrangement and V-X$_2$-2d,in which V and two solute atoms (X) lie in the same plane forming a two-dimensional arrangement. Similarly, V-X$_3$complex can have two different arrangements namely, a 2-dimensional arrangement V-X$_3$-2d, and another non-coplanar three-dimensional arrangement V-X$_3$-3d.Now, if one compares the energies against these entries, it is clearly seen that there is energy difference between V-Cu$_2$-1d and V-Cu$_2$-2d (0.03eV), V-Cu$_3$-2d and V-Cu$_3$-3d (0.05eV), V-Cu$_4$-2d and V-Cu$_4$-3d (-0.09eV) configurations. The general trend that emerges from these energy values is that the higher the dimension of the arrangement, more stable is the arrangement, except for the case of Cu in its VX$_4$ configurations.

In case of Ni-atoms, the binding energy is positive till $n=4$ and it becomes negative (repulsive) for n=5.A single vacancy can accommodate four Ni-atoms to form a stable cluster and after that, addition of one more Ni atom makes the complex energetically unstable. Considering the magnitude of positive energies in cases of Cu and Ni (see Table 5.3), it is apparent that the vacancy-solute clustering involving substitutional Cu atoms are more stable than the corresponding clusters involving Ni atoms. Interestingly, the strong interaction among V-Cu and Cu-Cu as compared to the cases involving Ni atom leads to higher total binding energy of V-Cu_n complex than for the V-Ni_n complex. The finite energy difference between V-Ni_2-1d and V-Ni_2-2d (0.05eV), V-Ni_3-2d and V-Ni_3-3d(0.04eV), and V-Ni_4-2d and V-Ni_4-3d (0.01eV)as listed in Table 5.3 implies that like the V-Cu complex, total binding energy of the V-Ni complex is also dependent not only on the number of solute atoms, but also on the arrangement of solute atoms in the configuration. A deeper insight into the difference in binding energy of the complexes of two different solute atoms in the bcc Fe matrix can be obtained by decomposing the total binding energy into distortion binding energy and electronic binding energy using the method described in section 5.2.1.

5.3.4 Energy Decomposition in V-X_n clusters

It is interesting to explore different factors that control the nature of interactions among different entities. As mentioned above, total interaction energy can be split into two major components, namely electronic effect and distortion effect. The electronic factor primarily includes effect of electron distribution and distortion effect is related to strain induced or relieved due to replacement Fe atoms by solute atoms and mainly includes the interaction of strain field around the defects. Therefore, we calculate here the contributions of these two components of the total binding energy for different vacancy-solute clusters V-Cu_n and V-Ni_n and discuss them in the following subsection.

5.3.4.1 V-Cu_n clusters

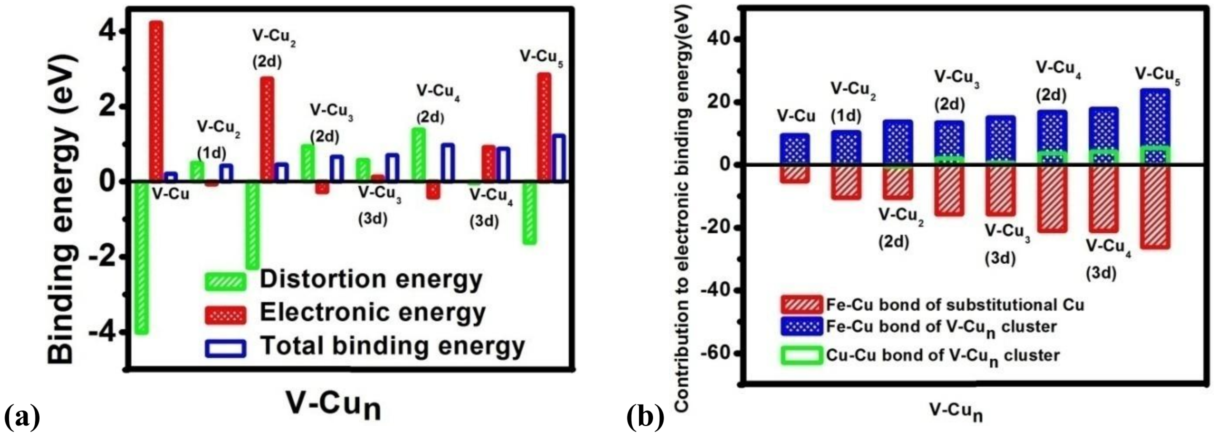

Figure 5.4. (a) Decomposition of total binding energy of V-Cu$_n$ complex into distortion and electronic binding energy **(b)** Decomposition of electronic binding energy into the contributions of different bonds in V-Cu$_n$ complex.

The distortion and electronic binding energies along with the total binding energy for V-Cu$_n$ clusters are represented in Figure 5.4(a). In V-Cu$_n$ complexes, the attractive (positive) or repulsive (negative) nature of the distortion energy does not follow any regular pattern. The positive distortion energy in some of the complexes indicates that the solute and vacancy induced strain in the Fe lattice is reduced due to complex formation. On the other hand, negative distortion energy indicates that the strain induced by separated vacancy and solute atom is enhanced when they form agglomerate of V-X$_n$ (X=Cu/Ni) type. It is to be noticed (see Figure 5.4 (a)) that the strength as well as sign of both distortion and electronic energies depends not only on number of solute atoms but on the relative positions of solute atoms (i.e. topological arrangements) in the lattice as well. For the most of the V-Cu complexes, both the electronic and the distortion energies are quite large and of comparable magnitude but of opposite sign. The small positive total binding energy (0.21 eV) in V-Cu complex is a result of nullification of the huge stabilization gained due to electronic contribution to the binding energy by the destabilizing effect of the distortion energy of almost similar magnitude. The large positive

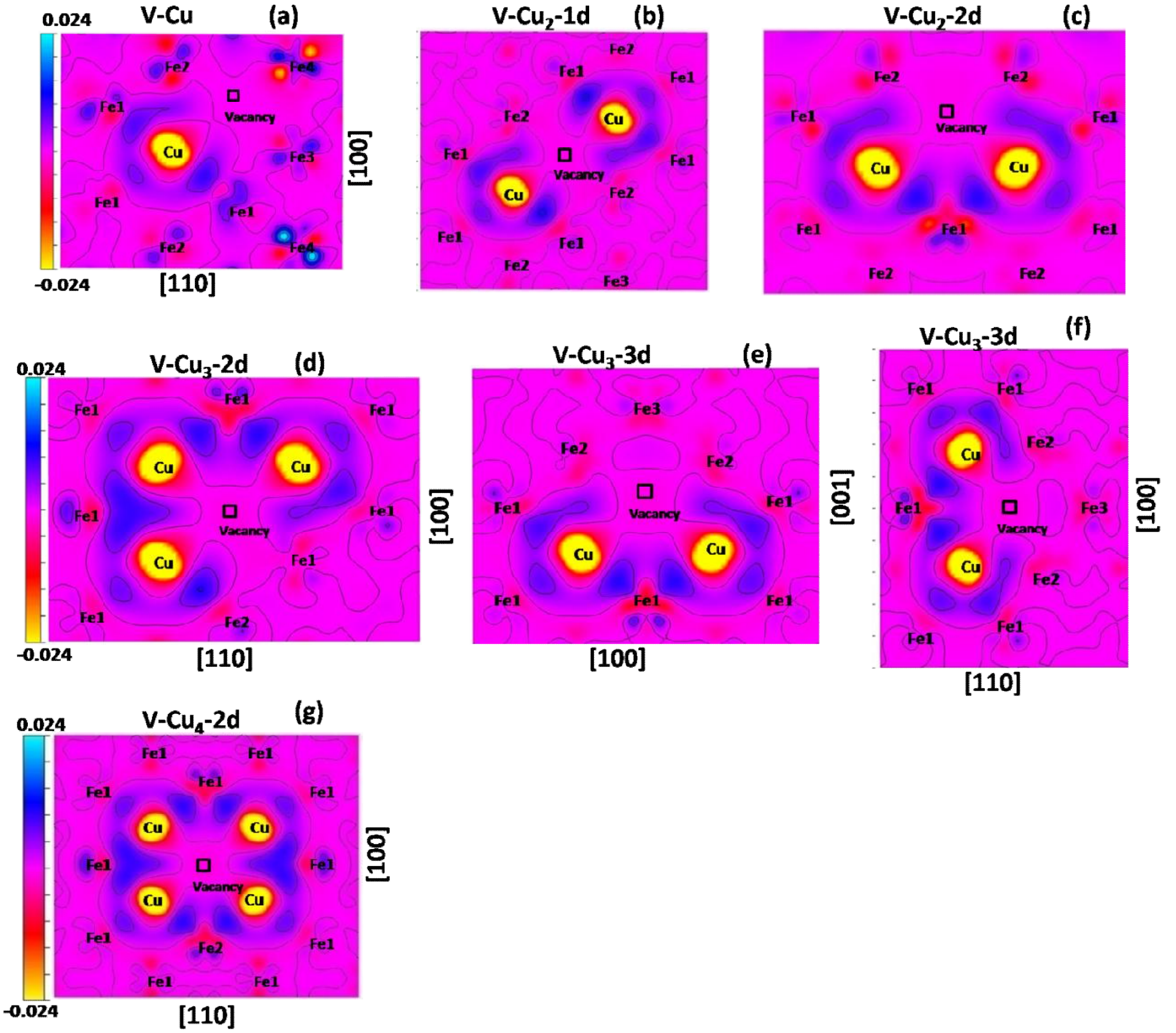

Figure 5.5. The differential charge density distribution (in eV/Ǻ^{3}) for vacancy with solute atoms in V-Cu$_n$ complex in bcc-Fe lattice. The charge distributions of Cu and their nearest neighbor Fe-atoms are shown here.

electronic contribution to the binding energy is a result of redistribution of electron cloud with the formation of Fe-Cu bonds. However, in case of V-Cu$_2$-1d complex, magnitudes of both the distortion and electronic energies are small, but slightly more positive distortion energy outweighs the destabilizing effect of electronic energy, making the complex stable. It may be noticed that unlike V-Cu complex, where stabilization arises from electronic energy, in this case, small, positive total binding energy is coming from stabilizing effect of distortion energy. Again, for V-Cu_2-2d complex, both the energies are quite large, but the resulting small, stabilizing total binding energy (0.45eV, see Table 5.3) is a result of counterbalancing the distortion energy by the stabilizing electronic energy of slightly higher magnitude than the former one. In V-Cu_3-2d, distortion energy is the main stabilizing factor, as the electronic energy acts in opposite direction, whereas in V-Cu_3-3d complex, both the components of energy, although small, acts in the same direction to stabilize the complex. In case of V-Cu_4complex, distortion energy is the stabilizing force in 2d case, but electronic energy is the stabilizing factor in the 3d case. Finally, in V-$Cu_{5,}$ it is the electronic energy that counterbalances the destabilizing effect of the negative distortion energy.

To get further insight into how the electronic energy is distributed among various bonds, further decomposition (Figure 5.4(b)) of electronic energy in V-Cu_n complexes is made and in addition to that, differential charge densities have also been calculated(see Figure 5.5). In all the cases, Fe-Cu bond energy in the complex is positive and it increases with increasing number of Cu atoms in the V-Cu_n complexes. For V-Cu_n complexes with n up to 2, contribution of the Cu-Cu bond energy is negligibly small. Beyond $n=2,$ positive Cu-Cu bond energy increases with increasing number of Cu atoms in the complex. For the V-Cu complex, the electronic energy is positive (see Figure 5.4(a)) and from the decomposition of the electronic energy plot (see Figure 5.4(b)),it is clear that the positive electronic energy is a consequence of cancellation of larger Fe-Cu bond energy, which is positive in the complex by the same (with a negative sign) in the Cu substitutional lattice. This is also evident from differential charge density plots (see Figure 5.5), in which considerable charge transfer between the Cu atom and the surrounding Fe atoms takes place. Therefore, the favorable Fe-Cu interaction in the complex is responsible for the positive electronic binding energy. In the case of V-Cu_2 cluster, the electronic energy differs greatly between V-Cu_2-1d and V-Cu_2-2d configurations (see Figure 5.4(a)). In V-Cu_2-1d complex, as two Cu atoms and vacancy lie in the same line, with the position of the vacancy lying between the two Cu atoms, distance between the two Cu atoms is large enough ($\sqrt{3}a$, a being the lattice parameter, cf. Figure 5.3) and therefore, there is almost no interaction between two Cu atoms. As a result, the binding energy of this complex is close to sum of the binding energies of two isolated V-Cu complexes, indicating no additional gain in stability of V-Cu_2-1d complex with respect to two isolated V-Cu complexes. On the other hand, in V-Cu_2-2d complex, as two Cu atoms and vacancy occupy three vertices of a triangle, the distance between two Cu atoms decreases ($\sqrt{2}a$), as a result of which, interaction between the two Cu atoms becomes repulsive (see negative energy in Figure 5.2(a) at this distance). However, Fe-Cu bonding in V-Cu_2-2dcomplex is stronger than that in the V-Cu_2-1d complex.

The facts discussed above can also be corroborated from differential charge density plots in Figure 5.5. The differential charge density plot for V-Cu_2-2d complex (see Figure 5.5 (c)) clearly indicates that the charge transfer among the 2 Cu atoms and the Fe atom nearest to both the Cu atoms is more than the same in the V-Cu_2-1d case (Figure 5.5(b)). The considerable electron density lying between the nearest Fe atom and the two Cu atoms also indicates that there is considerable electronic interaction between Fe and Cu atoms. The fact that the Fe-Cu bonding in V-Cu_2-2d complex is stronger than that in V-Cu_2-1d complex as observed in Figure 5.4(b) is a consequence of the charge transfer phenomenon discussed above. The above discussion also explains why the electronic energy contribution to the binding energy in the V-Cu_2-2dcomplex is more than that in the V-Cu_2-1d complex. For V-Cu_3complex, the electronic energy is negative for 2d and positive for 3d configuration. The Cu atoms are located more closely to each other in V-Cu_3-2d configurations than in V-Cu_3-3d configurations. Therefore, there will be more Cu-Cu bond formation in V-Cu_3-2das compared to V-Cu_3-3d configuration which is clearly visible from Figure 5.4(b) as well. Moreover, this Cu-Cu bond formation in V-Cu_3-2d configuration weakens the formation of Fe-Cu bond in this complex. Whereas, in V-Cu_3-3dcomplex, interaction among Cu atoms at these distances is repulsive which further results in strong Fe-Cu bond formation. This is consistent with our electronic energy decomposition results as well Figure 5.4(b). Thus, the electronic energy is higher for V-Cu_3-3d as compared to V-Cu_3-2d configuration. In V-Cu_4 complex, the electronic energy is more for V-Cu_4-3d configuration as compared to V-Cu_4-2d. In V-Cu_4-3d configuration, the number of 2NNCu atoms is more than that in V-Cu_4-2d configuration. It is observed from Figure 5.2(a) that Cu-Cu interaction is negligible at 2NN distances which further result in the formation of Fe-Cu bond in V-Cu_4-3d configuration. In addition, Figure 5.4(b) also shows that the Fe-Cu bond is slightly stronger in V-Cu_4-3d than in V-Cu_4-2dconfiguration, which results in more electronic energy for V-Cu_4-3d configuration. Further in V-Cu_5 complex, the number of 2NN Cu atoms increased further which probably implies stronger Fe-Cu bond formation and hence higher electronic energy.

5.3.4.2 V-Ni_n clusters

As in case of V-Cu_n clusters, we have decomposed the total binding energy of different V-Ni_n (n=1-5) clusters into various components as well. The decomposed energies for these clusters along with total binding energies are presented in Figure 5.6(a).The behavior of the components of the total binding energy in this case is different from the same for V-Cu_n clusters (compare the bar graphs in Figure 5.4(a) with those in Figure 5.6(a)).Although the binding energy in this case is positive and increasing with increasing number of Ni atoms, magnitude of the binding energy is very small. It is interesting to note that the distortion energy is positive and electronic energy is negative for *n* = 1 to 3 clusters. Like in the cases of V-Cu$_n$ clusters, in this case also, both the number of solute atoms and their configurations significantly affect the strength of distortion as well as electronic energies. To explore the interaction behavior further, decomposition of electronic binding energy in V-Ni$_n$ clusters is performed as shown in Figure 5.6(b) and differential charge density is also calculated (see Figure 5.7).

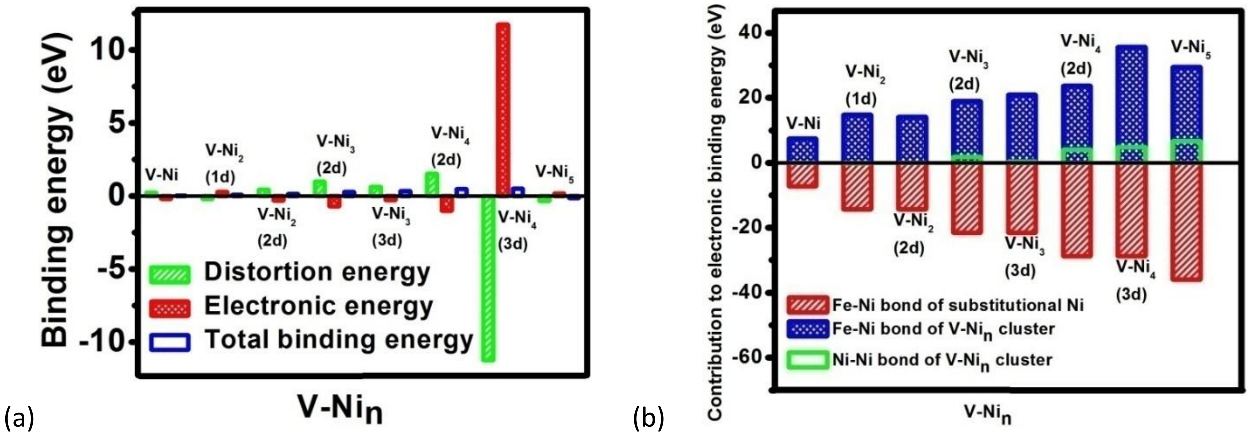

Figure 5.6. (a) Decomposition of total binding energy of V-Ni$_n$ complex into distortion and electronic binding energy (b) Decomposition of electronic binding energy into the contributions of different bonds in V-Ni$_n$ complex.

For the V-Ni complex the electronic binding energy is slightly negative. But the positive distortion energy in this case more than compensates the destabilizing electronic energy component and thereby stabilizes the V-Ni cluster in the Fe matrix. It is apparent from the differential charge density plots (in Figure 5.7) that the negative electronic energy is a consequence of weaker vacancy-solute and Fe-solute interaction as compared to the respective complex in the V-Cu_n case. There is very weak Fe-Ni interaction present in V-Ni complex as compared to Fe-Cu interaction in V-Cu complex. Therefore, electronic binding energy of V-Ni complex is smaller than that in V-Cu complex. In the case of V-Ni_2 cluster, the electronic energy differs slightly between V-Ni_2-1d and V-Ni_2-2d configurations. For V-Ni_2-1d, there is strong repulsive interaction between two Ni atoms (Figure 5.2(b)) but a stronger Fe-Ni bonding in this case (see Figure 5.6(b)). However, there is almost negligible interaction between two Ni atoms in V-Ni_2-2d configuration as shown in Figure 5.2(b). Further, the stronger Fe-Ni bonding in V-Ni_2-1d as compared to V-Ni_2-2d configuration can also be confirmed by differential charge density plots (Figure 5.7(b) and (c)). In addition, the electronic energy decomposition plot (Figure 5.6(b)) also shows that Fe-Ni bonding in V-Ni_2-1d cluster is stronger than in V-Ni_2-2d cluster. Thus, this strong Fe-Ni bond formation in V-Ni_2-1d configuration as compared to in V-Ni_2-2d, leads to the higher (positive) electronic energy in V-Ni_2-1d as compared that in V-Ni_2-2d configuration (negative). In V-Ni_3 complex, the electronic energy is negative for both V-Ni_3-2d and V-Ni_3-3d configurations, although having difference in their magnitudes. In V-Ni_3-3d configuration, all Ni-atoms are at 3NN distance to each other and hence, have negligible interaction among them (as represented in Figure 5.2(b)). It is also to note from Figure 5.6(b) that Fe-Ni bond is stronger in V-Ni_3-3d cluster than that in V-Ni_3-2d cluster. It results in higher electronic binding energy in V-Ni_3-3d as compared to V-Ni_3-2d configuration. In V-Ni_4 complex, there is a large difference between the electronic energies of V-Ni_4-2d and V-Ni_4-3d configurations. The electronic energy is negative for V-Ni_4-2d whereas, highly positive (attractive) for V-Ni_4-3d configuration. The number of Ni atoms at 2NN distance from another Ni atom is more in V-Ni_4-3d configuration as compared to V-Ni_4-2d configuration. Since 2NN

Ni-atoms have repulsive interaction among each other (Figure 5.2(b)), probably this repulsive interaction between Ni-atoms leads to the formation of strong Fe-Ni bonds in V-Ni_4-3d configuration[9]. This argument is consistent with our decomposition of electronic energy results as well. Since, it is observed clearly from Figure 5.6(b) that Fe-Ni bond is stronger in V-Ni_4-3d cluster as compared to that in V-Ni_4-2d cluster. This leads to the positive electronic binding energy in V-Ni_4-3d as compared to in V-Ni_4-2d configuration. Furthermore, the distortion energies of V-Ni_4-2d and V-Ni_4-3d configuration are also showing large difference. The positive value for V-Ni_4-2d and negative for V-Ni_4-3d configuration represent the strain relief in V-Ni_4-2d cluster and enhanced strain in V-Ni_4-3d cluster respectively. This is probably because, in 2d-complex Ni atoms and the vacancy are in the same plane and therefore strain relief by utilizing the vacancy space is plausible. In V-Ni_5, electronic energy is positive (attractive) and distortion energy is negative (repulsive) and the interplay of the two contributions results in negative (repulsive) total binding energy. In passing, it is to be noticed that in both V-Cu_n and V-Ni_n complexes, SA-SA stabilizing interaction increases with the increasing number of SA atoms.

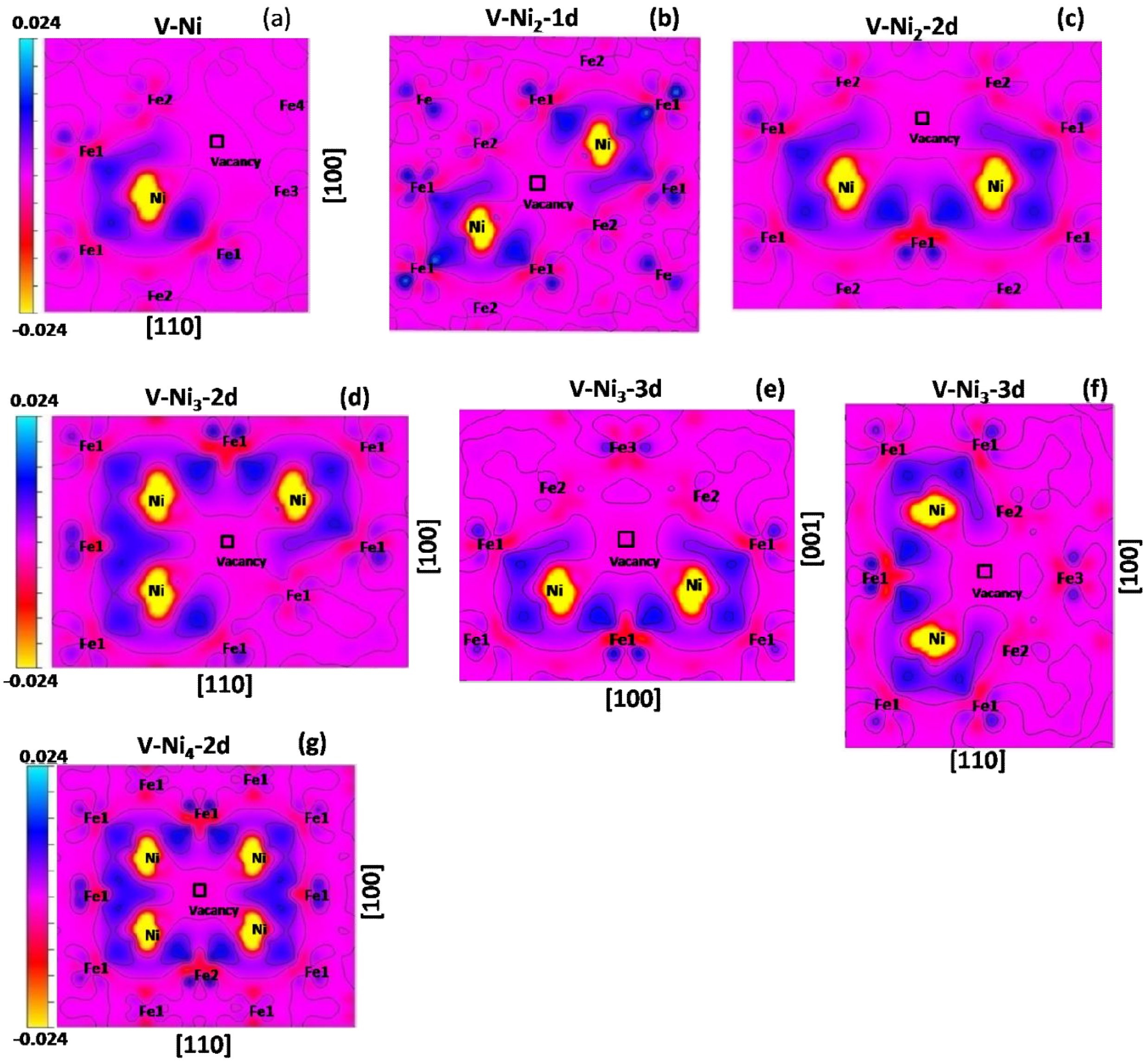

Figure 5.7. The differential charge density distributions (in eV/Ǻ^{3}) for the V-Ni$_n$ complexes (with different *n*) in the bcc-Fe lattice. The charge distributions of Ni and their nearest neighbor Fe-atoms are shown here. Positive values on the scale placed on the left indicate accumulation of electrons.

From the above discussion we can conclude that behavior for vacancy-solute (Cu / Ni) interaction in the bcc-Fe is governed by the combination of electronic and distortion energies, unlike in case of tungsten (W) where electronic energy contribution is dominant over distortion energy contribution to the overall binding energy of the vacancy-solute complex formation [29].Furthermore, in the present case of complex formation between vacancy and Cu or Ni, electronic and distortion energy contributions are always opposite to each other in most of the cases (in terms of stabilizing effect) (see Figure 5.4(a) & 5.6(a)). This implies that the studied configurations for both the solute atoms are stabilized by either electronic energy or distortion energy. For Cu atoms, there are a few configurations in which stability is decided by distortion energy and for some other configurations it is decided by electronic energy. Only for V-Cu_3-3d configuration, both the distortion energy and the electronic energy help in stabilizing the complex. However, for Ni atoms, stability is mainly decided by the distortion energy except for V-Ni_2-1d and V-Ni_4-3d configurations where electronic energy decides the stability. For V-Ni_n complexes, there is not a single studied configuration, in which both the energies are involved in stabilizing the configuration.

Binding volume (BV) as calculated using eq. (5.11) represents change in volume in the lattice due to complex formation. The total binding energy (BE) of the V-X_n (X=Cu/Ni) complexes for different *n* values as a function of BV is shown in Figure 5.8(a) and (c) for Cu and Ni complexes respectively. As can be seen from these figures, in both the cases, total BE follows a non-monotonic trend when plotted as a function of BV. In case of Cu complexes (see Figure 5.8(a)), the total BE increases slightly initially and then suddenly it decreases and after that it increases almost linearly with BV. But for the Ni complexes (Figure 5.8(c)), BE increases initially and then it

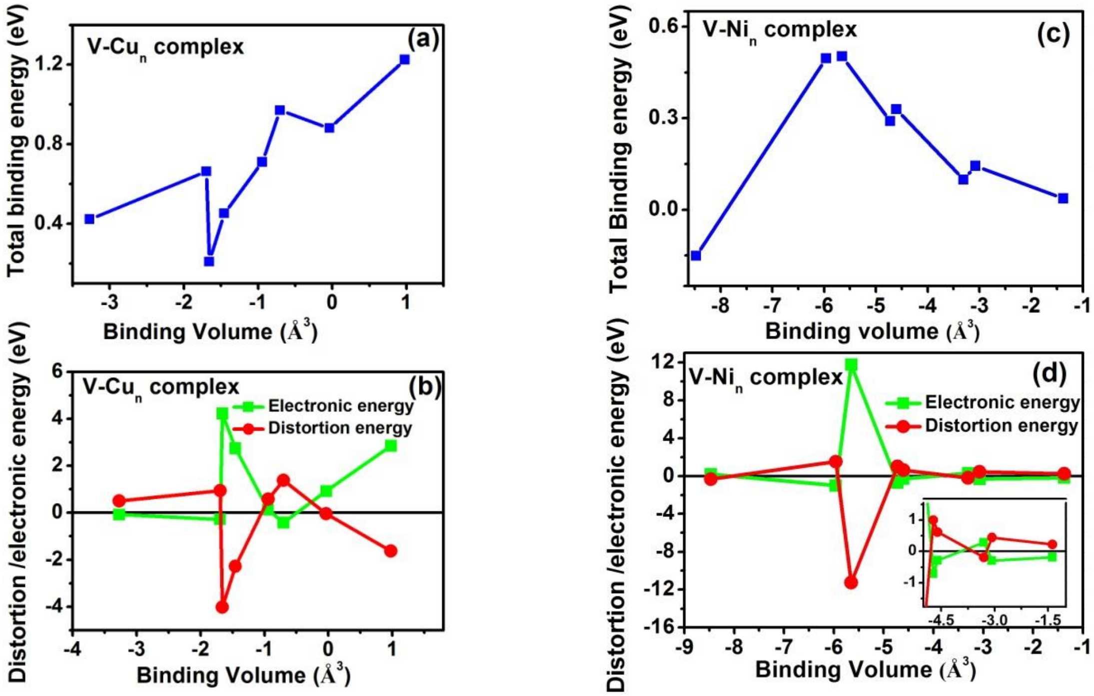

Figure 5.8. (a) Total binding energy and (b) constituent distortion, electronic energies as a function of binding volume for V-Cu$_n$ complexes.(c) Total binding energy and (d) the constituent distortion and electronic energies for the V-Ni$_n$ complexes. In the inset right side of the plot shown in panel (d) is zoomed to show the competing nature of the two.

steadily decreases. The different trend in these two systems is perplexing. In order to get further insight, splitting of total BE into distortion and electronic energies have been performed. The dependence of the component energies on BV as shown in Figures 5.8(b) and (d) clearly demonstrates that as a function of binding volume, distortion and electronic energies act in opposite fashion compensating each other and finally either electronic or distortion energy dictates the stability by over balancing the other. More importantly, in case of V-Cu$_n$ complexes, the total BE increases from 1st to 2nd points in the plot due to increase in positive (favorable) distortion energy. From 2nd to 3rd point, highly positive electronic energy and highly negative distortion energy compensates each other, but the rate of increase in unfavorable (negative) distortion energy being more than that of increase of favorable electronic energy and therefore BE decreases sharply. Beyond this point, there is a steady increase in BV due to decrease in electronic energy but increase in favorable distortion energy with BV. In the last two points again, due to the favorable change in electronic energy with BV, total BE increases.

However, for V-Ni_n complexes, initial increase in BE (from 1st to 2rd point) is due to favorable contribution from the distortion energy. From 2nd to 3rd point of the plot, the electronic energy increases favorably and sharply but distortion energy also increases in opposite direction, giving rise to an overall compensation, in which favorable electronic energy slightly outweighs the unfavorable contribution due to distortion energy. From 3rd point onwards, favorable electronic energy decreases sharply and becomes unfavorable (negative). It is the distortion energy that is favorable and thus the overall BE becomes positive but decreasing. Although splitting of the BE clearly demonstrates the compensatory nature of the component energies, but assigning any physical origin of such behavior is not possible.

5.3.5 Binding energies of Cu_n-Ni_m complexes

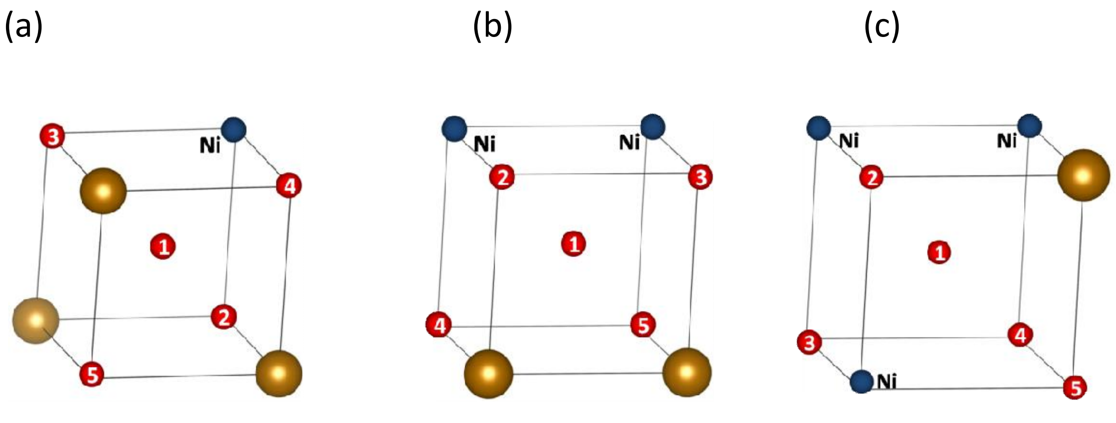

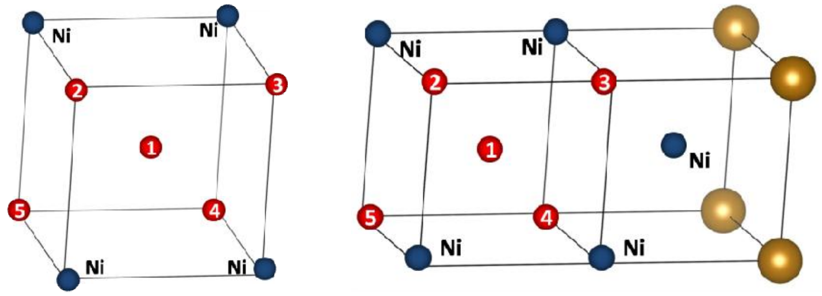

(d) (e)

Figure 5.9. Schematic representation of the investigated configurations for Cu_n-Ni_m complex for *n* and *m* up to 5.(a) *m*=1 (b) *m*=2 (c) *m*=3 (d) *m*=4 (e) *m*=5.

We have investigated the binding energies of different sized stable clusters of Cu_n-Ni_m for *n* and *m* upto 5 and the studied configurations are shown in Figure 5.9. The binding energy results are shown in Figure 5.10 and it is observed that the binding energy of all the clusters are attractive in nature, which implies that the formation of Cu_n-Ni_m clusters are energetically favorable [28]. Interestingly, the binding energy increases with the number of Ni-atoms as well as with the number of Cu-atoms, and thus it indicates that smaller clusters can grow by absorbing Cu or Ni atoms. Further, the rate of increase in the binding energy with increase in number of Cu-atoms is significantly higher than that with increase in number of Ni atoms. The rationale behind this behavior is the stronger Cu-Cu interaction as compared to Ni-Ni interaction in the Fe matrix.

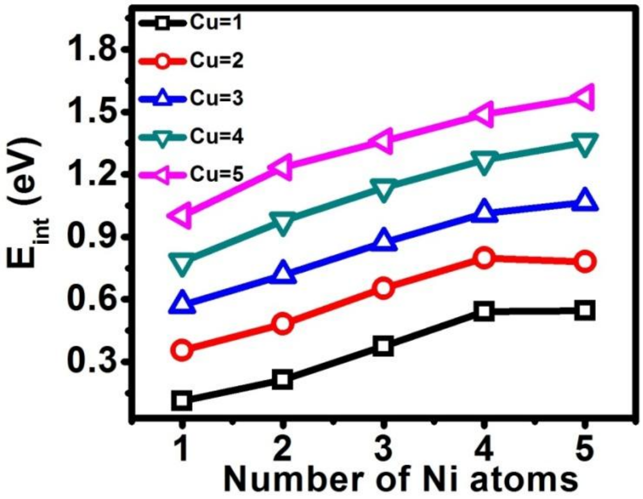

Figure 5.10. The binding energy of Cu_n-Ni_m clusters in bcc-Fe lattice for *n* and *m* upto 5.

5.3.6 Formation energies of Cu_n-Ni_m complexes

In order to understand the feasibility of the presence of the solute atoms in cluster form relative to random solute orientation in the fcc BCC Fe matrix, we have constructed the systems in two different ways: in one case the cluster like configuration as shown in Figure 5.9 is created by placing all solute atoms in nearby substitutional position. In another case, the solute atoms are placed randomly. In this case we have used 128 initial to facilitate the random distribution of the solute atoms. The formation energies are calculated by using eq. 5.1(b) and the results for Fe-Cu_3-Ni_3 and Fe-Cu_4-$Ni_4$are shown in the Table 5.4 below.

Table 5.4. Formation energies of Cu_n-Ni_m atoms in complex form and in random distribution

Solute atoms and numbers	Formation Enthalpy (eV) of Fe- Cu_nNi_m complexes.	
	Complex form	Random distribution
3 Cu, 3 Ni	-23.26	-22.52
4 Cu, 4 Ni	-31.11	-30.22

Inspection of the results clearly shows that in both the cases, solutes in cluster or complex form is more stable than in randomly distributed condition in the bcc Fe matrix.

5.3.7 Binding energy of V_2-X_n clusters

The binding energy of V_2-X_n complex is investigated in order to understand the effect of di-vacancy on solute clustering behavior. The binding energies are represented in Figure 5.11(a) and the

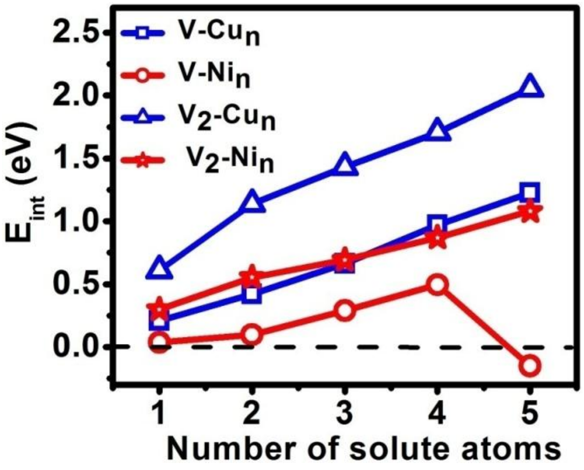

(a)

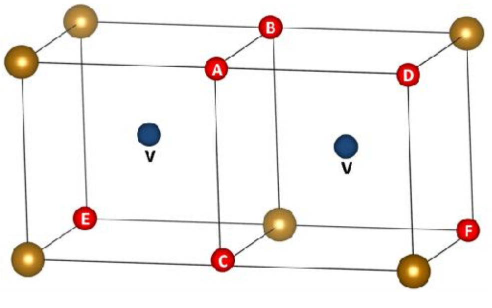

(b)

Complex	Atom position
V_2-X	A
V_2-X_2	B-C
V_2-X_3	B-C-D
V_2-X_4	B-C-D-E
V_2-X_5	B-C-D-E-F

Figure 5.11. (a) The binding energy of V-X_n and V_2-X_n clusters (b) represent the studied configuration for V_2-X_n complex.

studied configurations are shown in Figure 5.11(b). For all the complexes, binding energies with di-vacancy are positive i.e. the complexes are energetically stable. Further, V_2-Cu_n complexes show higher binding energy than V_2-Ni_n complex, however, it increases with number of solute atoms for both Cu and Ni complexes. This further implies that the di-vacancy has stronger attraction for the Cu atoms than for the Ni atoms and can further enhance the diffusion of Cu atoms. Moreover, the binding energy for a di-vacancy is higher than that for single vacancy as can be seen from Figure 5.11(a) for both the complexes. It is interesting to note that V-Ni_5 complex is not stable, but V_2-Ni_5 complex is. At this juncture, our calculations indicate that irradiation defects can promote the aggregation of Cu/Ni atoms as it is seen that the di-vacancy has greater promoting effect on solute aggregation than mono vacancy.

5.4 Summary

In summary, by performing systematic first-principle electronic structure calculations within the framework of DFT, we have demonstrated how the signature of solute (namely Cu and Ni) clustering in ferritic steel can be understood from the careful study of microscopic interactions of Cu and Ni solute atoms with irradiation induced defects in bcc-Fe lattice. The preeminent conclusions from the present investigation are as follows:

The calculated Cu-Cu and V-Cu interactions are found to be attractive (positive) at shorter distances (see Figure 5.2(a)) and this attractive interaction between two Cu atoms and its enhancement in presence of vacancies directly indicate that the aggregation propensity of the Cu atoms to form clusters in the bcc-Fe matrix increases in presence of vacancies. On the other hand, for the Ni-complex, Ni-Ni interaction is repulsive at shorter distances, but V-Ni interaction is attractive up to 2NN distance (see Figure 5.2(b)). Moreover, the migration barrier for 1NN substitutional site for Ni is found to be higher as compared to that for Cu atom (see Figure 5.1(c)). It can be concluded that the combined effect of weaker (as compared to Cu) V-Ni interaction along with higher migration barrier results in sluggish Ni diffusion (through hopping) as compared to Cu diffusion in the bcc-Fe lattice. The combined effects of stronger Cu-Cu interaction and slower Ni diffusion along with repulsive Ni-Ni interaction but attractive Cu-Ni interaction results in the formation of core-shell Cu-Ni clusters, as observed in earlier experimental work[28].This fact is further corroborated from the binding energy calculations of small clusters of Cu_n-Ni_m (with *n* and *m* varies from 0 to 5) present in bcc-Fe matrix. It is clearly demonstrated (see Figure 5.10) that the formation of Cu_n-Ni_m cluster is energetically favorable and the binding energy becomes more attractive as the number of atoms (Cu and Ni) increases in the cluster. From our vacancy and solute interactions studies it transpires that the binding energies of V-X_n complexes are dependent on both number of solute atoms and their configurations (relative positions in the Fe matrix). The most important part of this study involves the decomposition of the binding energy into distortion energy contribution and electronic energy contributions, which in turn, is decomposed further into Fe-SA and SA-SA bonding energies. It is established that the fine balance between the opposing effects (see Figure 5.8(b) and (d)) of the distortion and the electronic energies (in most of the cases) determines overall interaction and stability of Cu and Ni complexes in the bcc-Fe lattice.

Our results indicate that the presence of both mono- and di-vacancies induce attraction and hence accelerates aggregation of solute atoms in the bcc-Fe lattice. Therefore, the presence of irradiation induced defects enhances the aggregation propensity of Cu/Ni solute atoms in bcc-Fe lattice. Recent investigations [30-31] have studied the precipitation behavior in steel using higher length scale methods, in which the information obtained from ab-initio DFT investigation has been used as inputs. But one of the most important outcomes of the present investigation is that for the first time the origin of solute segregation in steel is demonstrated with the electronic scale spatial resolution and different contributions to the binding energy of the solute cluster are also quantified. Present methodology can easily be applied to solute clustering behavior in any other alloys containing any other solute atoms. Further first principle based studies on the interactions of other solute atoms and irradiation induced point defects in the bcc-Fe and fcc-Fe matrices are in progress.

References

[1] K. Osamura, H. Okuda, K. Asano, M. Furusaka, K. Kishida, F. Kurosawa, and R. Uemori, ISIJ International **34**, 346 (1994).

[2] M. K. Miller, P. Pareige, and M. G. Burke, Materials Characterization **44**, 235 (2000).

[3] E. Vincent, C. S. Becquart, and C. Domain, Nuclear Instruments and Methods in Physics Research Section B: Beam Interactions with Materials and Atoms **228**, 137 (2005).

[4] C. Domain and C. S. Becquart, Physical Review B **65**, 024103 (2001).

[5] E. Vincent, C. S. Becquart, and C. Domain, Journal of Nuclear Materials **359**, 227 (2006).

[6] P. Olsson, T. P. C. Klaver, and C. Domain, Physical Review B **81**, 054102 (2010).

[7] N. I. Medvedeva, A. S. Murthy, V. L. Richards, D. C. Van Aken, and J. E. Medvedeva, Journal of Materials Science **48**, 1377 (2013).

[8] W.-x. Song and S.-j. Zhao, Physical Chemistry Chemical Physics **16**, 7222 (2014).

[9] T. Ohnuma, N. Soneda, and M. Iwasawa, Acta Materialia **57**, 5947 (2009).

[10] G. Kresse and J. Furthmüller, Computational Materials Science **6**, 15 (1996).

[11] J. P. Perdew, K. Burke, and M. Ernzerhof, Physical Review Letters **77**, 3865 (1996).

[12] G. Kresse and D. Joubert, Physical Review B **59**, 1758 (1999).

[13] C. Domain, C. S. Becquart, and J. Foct, Physical Review B **69**, 144112 (2004).

[14] T. He, Y. Jiang, R. Zhou, and J. Feng, RSC Advances **6**, 45250 (2016).

[15] L. De Schepper, D. Segers, L. Dorikens-Vanpraet, M. Dorikens, G. Knuyt, L. M. Stals, and P. Moser, Physical Review B **27**, 5257 (1983).

[16] Y. Tateyama and T. Ohno, Physical Review B **67**, 174105 (2003).

[17] C.-C. Fu, F. Willaime, and P. Ordejón, Physical Review Letters **92**, 175503 (2004).

[18] S. M. Kim and W. J. L. Buyers, Journal of Physics F: Metal Physics **8**, L103 (1978).

[19] I. Seki and K. Nagata, ISIJ International **45**, 1789 (2005).

[20] A. F. Bialon, T. Hammerschmidt, and R. Drautz, Physical Review B **87**, 104109 (2013).

[21] D. J. Hepburn, E. MacLeod, and G. J. Ackland, Physical Review B **92**, 014110 (2015).

[22] J. A. Rayne and B. S. Chandrasekhar, Physical Review **122**, 1714 (1961).

[23] N. Anento, A. Serra, and Y. Osetsky, Acta Materialia **132**, 367 (2017).

[24] S. Ahlawat, S. K. Sarkar, D. Sen, and A. Biswas, Microscopy and Microanalysis **25**, 840 (2019).

[25] G. Brauer and K. Popp, physica status solidi (a) **102**, 79 (1987).

[26] Y. Wang, J. Yin, X. Liu, R. Wang, H. Hou, and J. Wang, Progress in Natural Science: Materials International **27**, 460 (2017).

[27] A. Möslang, E. Albert, E. Recknagel, A. Weidinger, and P. Moser, Hyperfine Interactions **17**, 255 (1984).

[28] R. Prakash Kolli and D. N. Seidman, Acta Materialia **56**, 2073 (2008).

[29] X.-S. Kong, X. Wu, Y.-W. You, C. S. Liu, Q. F. Fang, J.-L. Chen, G. N. Luo, and Z. Wang, Acta Materialia **66**, 172 (2014).

[30] G. Bonny, C. Domain, N. Castin, P. Olsson, and L. Malerba, Computational Materials Science **161**, 309 (2019).

[31] L. Messina, M. Nastar, T. Garnier, C. Domain, and P. Olsson, Physical Review B **90**, 104203 (2014).

Chapter 6

Heavy Ion Radiation Study in SS316 Austenitic Stainless Steel

As mentioned earlier in chapter 1, austenitic stainless steel (ASS) is a very important structural element of the core of the nuclear reactors. Therefore, it is critically important to study radiation damage and related structural transformations of austenitic stainless steels. We have investigated various aspects of heavy ion irradiation of austenitic stainless steels in this Chapter.

6.1 Introduction

Irradiation generally leads to significant changes in microstructure and also causes crystal structural transformation in steels, as discussed in section 2.5.2 and 2.5.3 of chapter 2. The martensite phase in low-carbon steel like SS316 is body centred cubic (bcc) with the same lattice parameters as the ferrite phase [1], and the austenite phase is face centred cubic (fcc). Radiation-induced structural transformation in austenitic stainless steel has been investigated earlier using a variety of energetic ions [2-9]. Dudognon et al. [5] explored multiple different ion irradiations in SS316 and found the dependence of structural transformation only on the damage level, irrespective of the identity of the ions. Forward martensitic transformation (MT) in ASS was also observed by Wang et al. [10] under 3 MeV Au ion irradiation. In fact, the existence of forward MT in ASS under ion irradiation is quite well known as discussed in section 2.5.3 of chapter 2. However, there is only one report of radiation-induced reverse MT (i.e. martensite to austenite transformation) in ASS, by Vardiman et al. [7]. They observed reversion of stress-induced martensite to austenite in SS304 on implantation of austenite stabilizing elements (Ni and N ions), whereas Ne implantation had no effects. Notably, the researchers over the years observed either the forward or the reverse MT in their studies involving a wide range of irradiation conditions. To the best of the authors' knowledge, reports of coexistence of both the transformations in irradiated SS316 is absent in the archival literature. This chapter demonstrates radiation-induced reversal of martensite to austenite followed by re-emergence of martensite with increasing fluence, confirmed by XRD analysis and verified by magnetization measurements. The presence of both the structural transformations simultaneously is observed for the first time in this study.

As for the radiation-induced microstructural changes, the presence of Ni-Si precipitates in irradiated austeitic stainless steel is widely reported [11-12] (section 2.5.3 of chapter 2). Therefore, APT and SANS experiments are carried out to probe the microstructural changes in irradiated SS316.

6.2 Experimental details

Commercial grade cold-worked SS316 is used for this work (bulk composition in Table 6.1). Samples with dimension 10 mm x 10 mm x 1 mm, are irradiated at room temperature using the Pelletron accelerator facility at IUAC, Delhi with Ag^{9+} (120MeV) and Au^{8+} (100MeV) ions at three different fluences, $1x10^{13}$, $5x10^{13}$ and $1x10^{14}$ ions/cm^2. The irradiation damage is calculated in terms of displacement per atom (DPA) using Monte Carlo based computer program, SRIM2008 [13], according to the Norgett-Robinson-Torrens (NRT) formula [14] eq. 2.1 in section 2.1 of chapter 2. The calculated DPA profiles for both the ions are shown in Figure 6.1.

The damage depth is more for Ag ions than Au ions whereas, DPA is more for Au ions as compared to Ag ions. Nevertheless, the DPA is found to increase with fluence for both the ions.

Table 6.1. Chemical composition of austenitic SS316 steel (wt%).

Element	**Fe**	**C**	**Si**	**P**	**Ni**	**Mn**	**S**	**Cr**	**Mo**
wt%	**Bal.**	**0.017**	**0.36**	**0.035**	**10.02**	**0.91**	**0.022**	**16.07**	**2.08**

Detailed characterization of the alloy (before and after irradiation) has been performed using XRD and DC magnetization measurements (section 3.6 and 3.7 of chapter 3). Thickness of the samples was reduced from the un-irradiated side to ~100 μm for the XRD measurements. The exact same set of samples is used for the magnetization experiments as well.

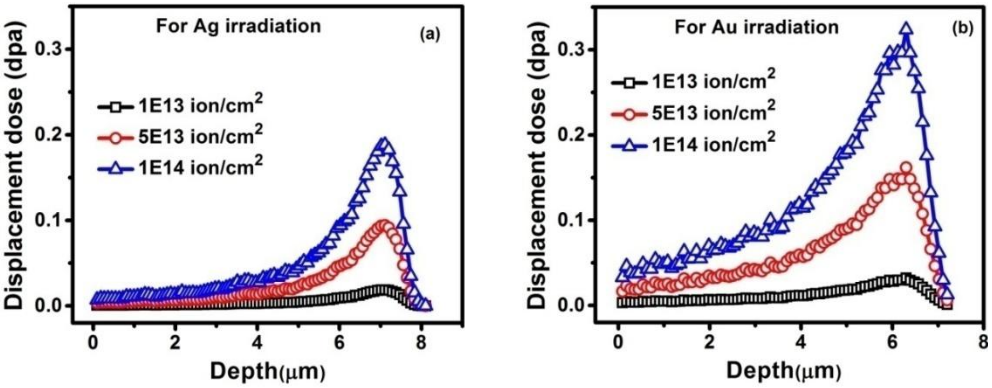

Figure 6.1. Represents damage profile of samples irradiated with (a) Ag ions (b) Au ions, at different fluences.

For the as-received SS316 samples, APT specimens are machined from the bulk samples to the dimension: 0.3mm x 0.3mm x 8 mm and subsequently electropolished in two stages using 10 vol % perchloric acid in methanol and 2 vol % perchloric acid in butoxyethanol, respectively (as per section 3.2.2.1). For the irradiated SS316 samples, site-specific APT specimens from the radiation-damaged region are prepared using focussed ion beam (FIB) method (as per section 3.2.2.2). APT experiments are carried out at a sample temperature of 50 K under ultrahigh vacuum ~ 1.5 E -10 mbar, using a CAMECA LEAP-5000XR instrument in IISC Bangalore. Ultraviolet (UV) laser pulsing mode with laser energy 100 pJ is utilized. Analysis of the tomographic data has been performed using IVAS software. SANS experiments have been carried out at D22 SANS facility at the Institute Laue Langevin (ILL) Grenoble, France, using an incident neutron wavelength of $\lambda = 0.6$ nm.

The DFT calculations have been performed using the Vienna ab-initio simulation package (VASP) [15] within the generalized gradient approximation based on Perdew-Burke-Ernzerh of functional [16]. The projector augmented-wave method [17] is used to treat the ion-electron interactions and plane wave basis set with a kinetic energy cutoff of 500 eV to expand the electronic wave functions. We considered a 3×3×3 supercell containing 108 Fe-atoms for fcc-Fe lattice. The Monkhorst-Pack scheme is utilized to sample the K-points in Brillouin zone. A 3×3×3 K-point grid is chosen for fcc-Fe lattice.

The formation enthalpy for a supercell containing N-atoms of Fe and one SA is calculated using eq. (5.1a) in chapter 5.

6.3 Results and Discussion

6.3.1 X-ray diffraction results

XRD patterns before and after irradiation are shown in Figure 6.2(a): all the major peaks of austenite are present, which is consistent with the literature [5]. Additionally, a small peak corresponding to (110) reflection of martensite (ferrite) phase is detected in the as-received sample (Figure 6.2(b)), which originated during cold working of SS316. Cold-worked ASS is known to contain stress-induced martensite [18-20].

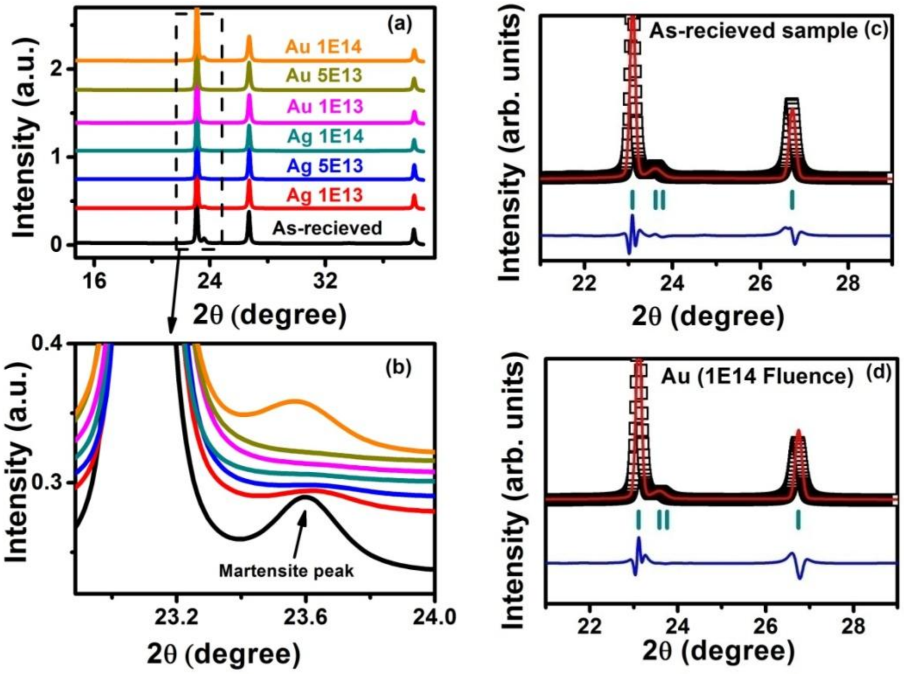

Figure 6.2. Represents (a) XRD patterns for as-recieved and irradiated samples (b) magnified view of the martensite peak. Reitveld fitted XRD pattern for (C) As-recieved sample (d) sample irradiated with 1x10^{14}ions/cm^{2}Au ion fluence.

Rietveld refinement of the diffraction patterns is performed using GSAS software [21]. Rietveld-refined profiles for the as-received condition and after Au (1x10^{14} ions/cm^2) ion irradiation are depicted in Figure 6.2(c) and (d), respectively. The goodness of the fit parameters for these refinements, like R(F^2) ~ 5% - 9%. The variation of phase fractions of martensite and austenite determined by Rietveld analysis is plotted against the fluence in Figure 6.3(a) and (b), respectively. The as-received sample shows higher fraction of martensite in comparison to all the irradiated samples. For Ag ion irradiation, the martensite phase fraction decreases progressively with increasing fluence (Figure 6.3(a)). At the same time, the corresponding austenite phase fraction increases continually with Ag ion fluence (Figure 6.3(b)), which signifies reversion of martensite to austenite. This clearly establishes the existence of reverse MT in SS316 under Ag ion irradiation.

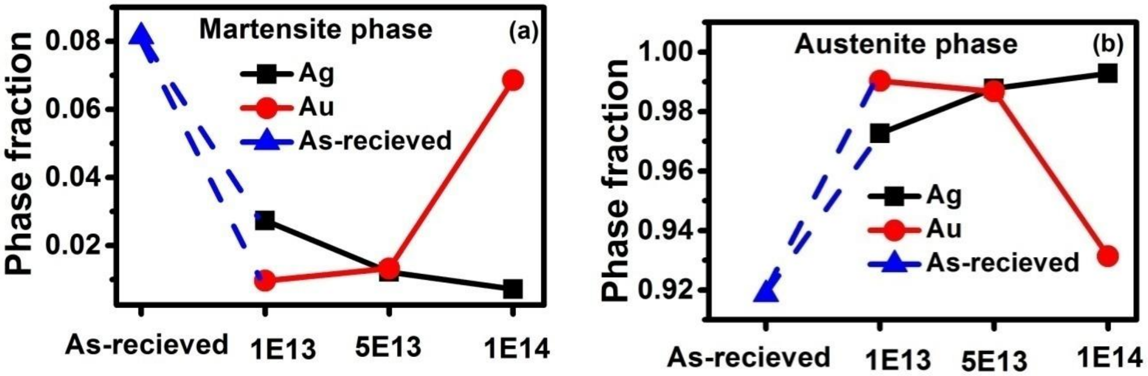

Figure 6.3. Phase fraction of (a) martensite phase; (b) austenite phase.

Interestingly, depending upon the fluence, both reverse and forward MT are observed when SS316 was irradiated with Au ions (Figure 6.3(a)). The martensite phase fraction at 1x10^{13} ions/cm^2 fluence of Au is lower than the as-received sample (Figure 6.3(a)), indicating presence of reverse MT. But, the martensite phase fraction increases for higher fluence, which implies forward MT. In addition, the austenite phase fraction (Figure 6.3(b)) reciprocates the martensite phase fraction behaviour for both the ion irradiations, which suggests the mutual transformation of austenite ↔ martensite phase during irradiation.

6.3.2 Magnetization results

Since martensite is ferromagnetic and austenite is paramagnetic, magnetization follows a linear relationship with the martensite phase fraction in steel [3,22]. Magnetization as a function of magnetic field up to 9 Tesla is recorded for each sample at room temperature with the field lying in the plane along the length of the rectangular shaped samples. The variation of spontaneous magnetization, obtained from high field linear extrapolation, is shown in Figure 6.4. For Ag ion irradiation, its value decreases with increasing fluence, which is a definitive indication of reduction in the martensite phase fraction. In contrast, its value initially decreases for Au ion irradiation for 1x10^{13} ions/cm^2 fluence, but increases afterward with further increase in fluence (for 5x10^{13} ions/cm^2 and 1x10^{14} ions/cm^2). Variation of magnetization values for Ag and Au ion irradiations follow exactly the same trend as the one showed by their respective martensite phase fractions (Figure 6.3(a) and Figure 6.4). Certainly, the magnetization response of SS316 under irradiation corroborates the XRD analysis results remarkably well.

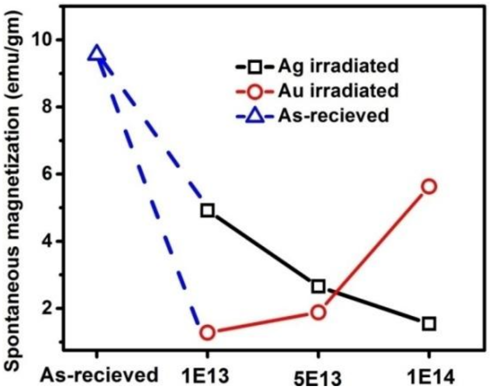

Figure 6.4. Displays spontaneous magnetization of as-recieved and all irradiated samples.

6.3.3 First-principle calculation

In order to understand the origin of these structural transformations, stabilities of both energetic atoms (Ag and Au) are studied based on the formation enthalpy in fcc-Fe lattice, Table 6.2. It is important to note that the formation enthalpy is lower for Au as compared to Ag in fcc Fe-lattice, which signifies comparatively higher stability for Au atoms. This result is consistent with earlier report [23]. Higher stability of the Au atoms in the fcc Fe-lattice, can be related to the higher solubility of Au rather than Ag in Fe-lattice [24-25].

Table 6.2. Formation enthalpy (in eV) for single SA (Ag/Au) in fcc-Fe lattice.

	Formation enthalpy
	FCC-Fe
Ag	-0.342
Au	-1.654

6.3.4 Microstructural evolution

6.3.4.1 Small angle neutron scattering (SANS) results

We have carried out SANS experiments for all irradiated samples and the corresponding scattering curves along with fitting profile are shown in Figure 6.5. The SANS data is analysed using SASFIT program using spherical particle model. It is observed that the dimension of inhomogeneities present in irradiated samples is of very small size typically of the order of few nano-meters and radius is increasing with fluence (Table 6.3).

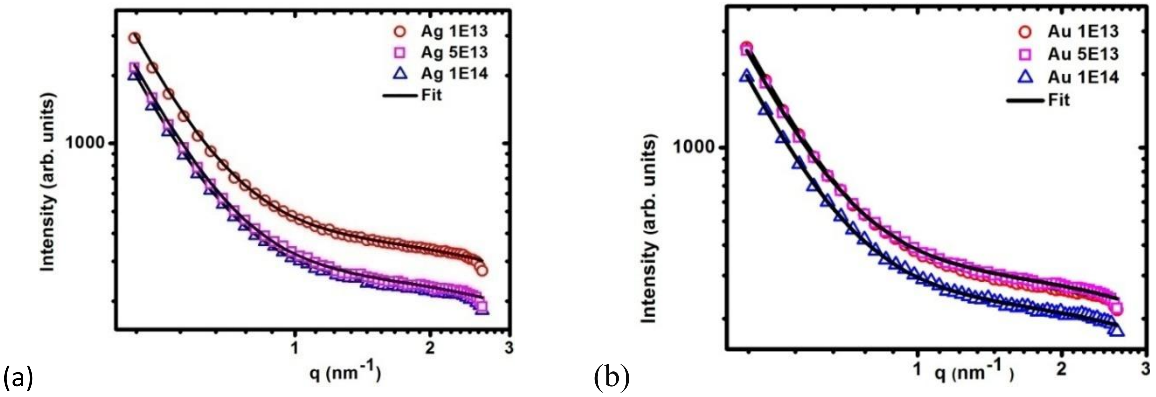

Figure 6.5. Variation of SANS scattering intensity profile for SS316 samples irradiated with (a) Ag ions (b) Au ions; for different fluences.

Table 6.3. Size of inhomogenities present in irradiated SS316 samples. The error in size value is 0.01.

Fluence	**1E13**	**5E13**	**1E14**
Ag ions : Radius (nm)	**0.38**	**0.39**	**0.39**
Au ions : Radius (nm)	**0.40**	**0.40**	**0.41**

6.3.4.2 Atom probe tomography (APT) results

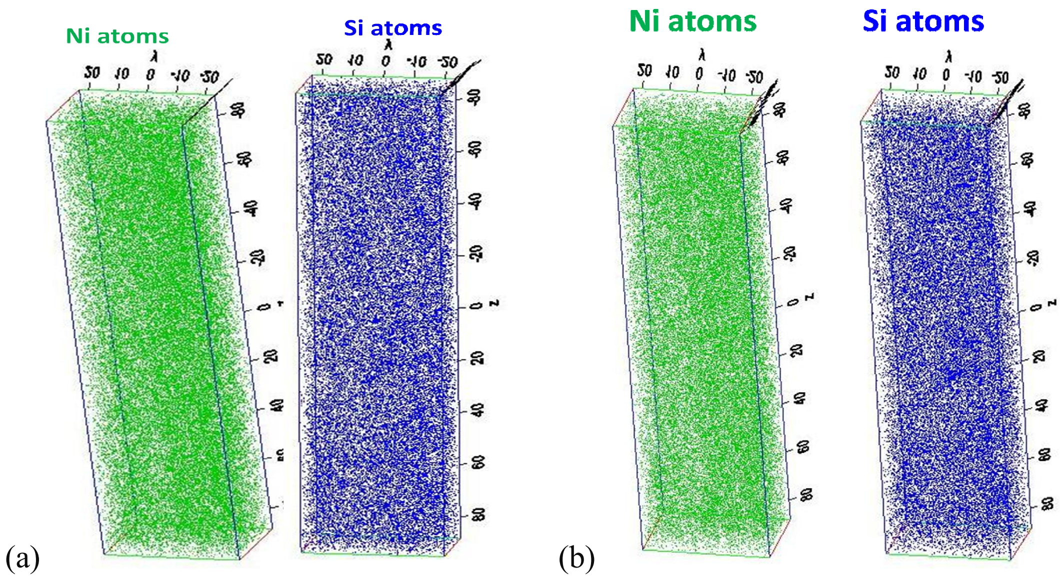

Figure 6.6. Atom maps representing Ni and Si atoms in (a) as-received SS316 (b) Au $1x10^{14}$ ions/cm^2 fluence irradiated SS316.

Atom maps of as-received and Au $1x10^{14}$ ions/cm^2 fluence irradiated samples are represented in Figure 6.6. We have used cluster algorithm method for this analysis. Only Ni and Si atoms are displayed for clarity and they are found to be uniformly distributed throughout the analysis volume in both as-received and highest damage irradiated sample (i.e. Au $1x10^{14}$ ions/cm^2 fluence). All other elements are also uniformly distributed in both samples. The sign of the inhomogeneities identified during SANS analysis are not noticed in APT analysis. This may be due to the very small size as can be seen from Table 6.3.

6.3.5 Discussion

Our work reports the existence of both forward and reverse MT in SS316 under heavy ion irradiations. However, the most striking observation is that even though Ag ions have a higher DPA and double the fluence of Au ions, they do not induce a forward MT. The occurrence of these transformations can be explained by the following two phenomena occurring simultaneously under irradiation: (i) radiation-induced forward MT in steel, caused by radiation-induced stresses [6]; (ii) reverse MT due to stabilization of austenite (Ag and Au are known to be austenite stabilizers) [5,26]. We have shown in the subsequent paragraphs, that the nature of the structural transformation depends upon the interplay of the above two factors and is controlled by their relative contribution.

Occurrence of reverse MT, for all fluences of Ag ion (Figure 6.3(a)), indicates the dominance of the second factor. In case of Au ion irradiation, contributions from both the factors appear to be significant as both forward and reverse MT were observed (Figure 6.3(a)). It is interesting to note that the martensite phase fractions at $1x10^{13}$ ions/cm^2 fluence for both Ag and Au ions are lower than that of the as-received sample (Figure 6.3(a)). This might be because the stress induced by irradiation is inadequate to form martensite at lower irradiation fluence, and the second factor dominates over the first one and results in stabilization of austenite. Higher stability of Au in Fe-lattice (*ab initio* calculations, Table 6.2) indicates that Au is a stronger austenite stabilizer than Ag. In fact, this explains why at a fluence 1x10^{13} ions/cm^2, Au ions show a lower phase fraction of martensite than Ag ions (Figure 6.3(a)).

On increasing the fluence of Au ions to 5x10^{13} ions/cm^2, dominance of the first factor is observed as austenite starts transforming to martensite, which is confirmed by the increase in the martensite phase fraction and the corresponding magnetization value (Figure 6.3(a) & Figure 6.4). It is also observed that the irradiation damage produced by Au ion of 5x10^{13} ions/cm^2 fluence, is lower than that of Ag ion of 1x10^{14} ions/cm^2 fluence, Figure 6.1(a) & 1(b). However, despite the lower fluence of the Au ions, the radiation-stress induced MT is observed only in the former case. This difference in the irradiation effect between Ag and Au ions may be attributed to the difference in the levels of radiation-induced stress. Though, for similar fluence, higher mass ions induce higher stresses than lighter mass ions [3], there is no report that shows that the induced stresses by lower fluence Au ions will be higher than Ag ions of higher fluence. Hence, to understand the formation of martensite by lower fluences of Au ions when compared to higher fluences of Ag ions, we calculated the vacancies generated for different fluences of Au and Ag ions using the SRIM2008 program. Vacancies created by ion irradiation are often used as an indicator of the radiation-induced stresses [3]. It can be seen from Figure 6.7(a) that the total number of vacancies per Au ion are higher than that per Ag ion. Furthermore, it is observed that Au ions with lower fluence (5x10^{13} ions/cm^2) and corresponding lower DPA generate larger number of vacancies when compared to Ag ions with higher fluence (1x10^{14} ions/cm^2) and higher DPA (Figure 6.7(b)). In fact, it is noticed (Figure 6.7(b)) that even though the damage is higher in the case of Ag, Au ion generates ~ 2 x10^{17} vacancies more than the Ag ion (point B and C in Figure 6.7(b) inset). This clearly indicates that Au ions with lower fluence cause more radiation-induced stress than Ag ions with the maximum fluence in the current study. This also helps us understand why Ag ions did not cause a forward MT. This observation strongly suggests that the MT induced by radiation-stress depends not only on the damage level (DPA) in the material but also on the type of ions used. Not surprisingly, at 1x10^{14} ions/cm^2 Au ion fluence, the stress induced in the material is higher and so also is the martensitic phase fraction.

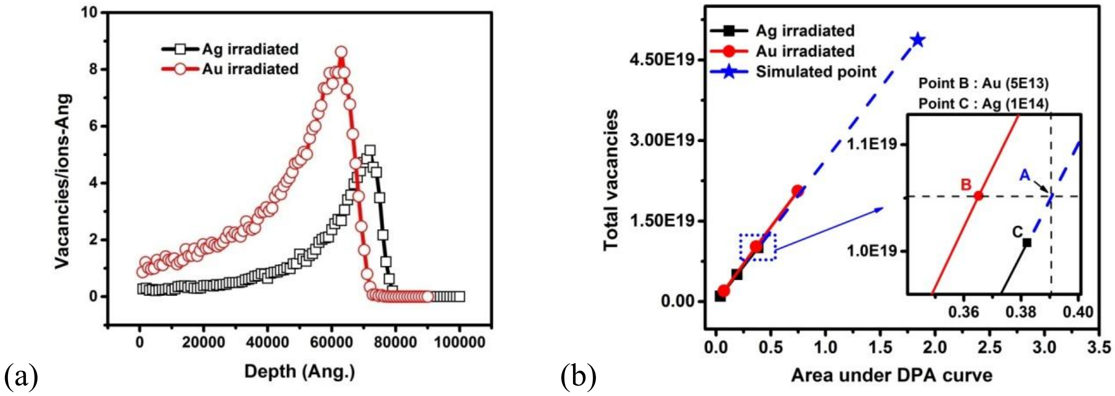

Figure 6.7. (a) Vacancy distribution for 120MeV Ag ions and 100MeV Au ions in SS316 (b) Variation of total vacancies with area under DPA curve. The star on this graph indicates the point which is simulated to extrapolate the experimental curve for Ag ions. Point B corresponds to 5x10^{13} ions/cm^2 fluence of Au ions and Point C corresponds to 1x10^{14} ions/cm^2 fluence of Ag ions.

Most of the earlier irradiation studies on SS316 have used much higher DPA levels than the ones used in this study. This could explain why almost all of them have reported forward MT under irradiation. In fact the only report on reverse MT is by Vardiman et al. [7], who used much lower damage level as compared to the others. In the present study, when irradiated with Au ions, reverse MT is observed only when the damage level is relatively low; whereas the radiation-stress induced forward MT is seen at higher damage levels. To locate the fluence of Ag ions which would induce enough radiation damage to induce a forward MT, the DPA vs vacancy correlation was extrapolated by simulating the total vacancies generated for a higher fluence of these ions ($5x10^{14}$ ions/cm^2), Figure 6.7(b). It indicates that at a fluence of $1.022x10^{14}$ ions/cm^2, the irradiation induced stresses for Ag ions will be similar to that of Au ions ($5x10^{13}$ ions/cm^2) (point A in Figure 6.7(b)), which induce a forward MT. Even though experimentally, we did not observe forward MT for the maximum fluence of Ag ions, our study indicates that at still higher fluence this transformation will be observed. Earlier studies have shown that irradiation by Ag ion at a higher DPA does indeed result in a forward MT [5]. On simulating the vacancy vs DPa plot from the data of reference 25, we found that the vacancies generated are several orders of magnitude higher than that of Au ion at ($5x10^{13}$ ions/cm^2). This gives further credence to the rationalization provided here.

We have also carried out SANS and APT experiments in order to understand the microstructural evolution of SS316 under irradiation. From SANS data, it is observed that very small size inhomogeneities (less than 1nm) are present in irradiated samples (Table 6.3), presumably as a result of rather limited irradiation damage in samples (Figure 6.1). Subsequently, we have performed APT experiments to study these small inhomogeneities. However, all elements present in SS316 are homogeneously distributed throughout the analyzed volume and no perceptible inhomogeneity is detected by APT analysis.

6.4 Summary

The present study shows that though, radiation damage by Au and Ag ions is known to cause forward MT, we observe, that upto a critical fluence, the cold-worked SS316 actually shows a reverse MT. We have, for the first time, shown the existence of both forward and reverse MT simultaneously in ion irradiated SS316. Reverse MT was detected till the radiation-induced stresses were inadequate to form martensite. However, the moment this critical point is crossed, forward MT is observed. Our results strongly indicate that the nature of phase transformation in ASS not only depends upon the extent of irradiation damage but also on the identity of the ions. The variation between the irradiation behaviors of Ag and Au ion is explained based on their stability and differences in the stress produced by them. Our finding offers the potential to tailor the properties of steels in terms of phase fraction and defects by irradiating them with a certain known fluence of different ions. This can be of great use in the industry.

Reference

[1] R.-b. Song, J.-y. Xiang, and D.-p. Hou, Journal of iron and steel research, international **18**, 53 (2011).

[2] O. Morozov, V. Zhurba, I. Neklyudov, O. Mats, A. Rud, N. Chernyak, and V. Progolaieva, Nanoscale Research Letters **10**, 154 (2015).

[3] H. Sanda, M. Takai, S. Namba, A. Chayahara, and M. Satou, Applied Physics A **50**, 573 (1990).

[4] J. Dudognon, M. Vayer, A. Pineau, and R. Erre, Surface and Coatings Technology **203**, 180 (2008).

[5] J. Dudognon, M. Vayer, A. Pineau, and R. Erre, Surface and Interface Analysis: An International Journal devoted to the development and application of techniques for the analysis of surfaces, interfaces and thin films **40**, 772 (2008).

[6] I. Sakamoto, N. Hayashi, B. Furubayashi, and H. Tanoue, Journal of applied physics **68**, 4508 (1990).

[7] R. Vardiman and I. Singer, Materials Letters **2**, 150 (1983).

[8] R. Leutenecker, G. Wagner, T. Louis, U. Gonser, L. Guzman, and A. Molinari, Materials Science and Engineering: A **115**, 229 (1989).

[9] N. Hayashi, I. Sakamoto, and T. Takahashi, Journal of Nuclear Materials **128**, 756 (1984).

[10] Q. Wang, H. Ogiso, S. Nakano, J. Akedo, and H. Ishikawa, Nuclear Instruments and Methods in Physics Research Section B: Beam Interactions with Materials and Atoms **206**, 118 (2003).

[11] A. Etienne, B. Radiguet, N. J. Cunningham, G. R. Odette, R. Valiev, and P. Pareige, Ultramicroscopy **111**, 659 (2011).

[12] W. Van Renterghem, M. J. KonstantinoviÄ‡, and M. Vankeerberghen, Journal of Nuclear Materials **452**, 158.

[13] J. P. B. a. M. D. Z. J.F. Ziegler, edited by I. I. Press2008).

[14] M. J. Norgett, M. T. Robinson, and I. M. Torrens, Nuclear Engineering and Design **33**, 50 (1975).

[15] G. Kresse and J. Furthmüller, Computational Materials Science **6**, 15 (1996).

[16] J. P. Perdew, K. Burke, and M. Ernzerhof, Physical Review Letters **77**, 3865 (1996).

[17] G. Kresse and D. Joubert, Physical Review B **59**, 1758 (1999).

[18] A. K. De, D. C. Murdock, M. C. Mataya, J. G. Speer, and D. K. Matlock, Scripta materialia **50**, 1445 (2004).

[19] E. Nagy, V. Mertinger, F. Tranta, and J. Sólyom, Materials Science and Engineering: A **378**, 308 (2004).

[20] B. Radiguet, A. Etienne, P. Pareige, X. Sauvage, and R. Valiev, Journal of Materials Science **43**, 7338 (2008).

[21] A. Gagin and I. Levin, Journal of Applied Crystallography **48**, 1201 (2015).

[22] K. Kayser, WIRE, 167 (1969).

[23] D. J. Hepburn, E. MacLeod, and G. J. Ackland, Physical Review B **92**, 014110 (2015).

[24] H. Fuse, N. Koshizaki, Y. Ishikawa, and Z. Swiatkowska-Warkocka, Nanomaterials **9**, 198 (2019).

[25] L. J. Swartzendruber, Bulletin of Alloy Phase Diagrams **5**, 560 (1984).

[26] D. Amram, O. Kovalenko, and E. Rabkin, Acta Materialia **98**, 343.

Chapter 7

Interactions of Foreign Interstitial Atoms (C, N, B, O) and Point Defects in Body- and Face-Centered Cubic Iron Lattice

Apart from heavy atoms likes Cu, Ni, Cr, Mn etc. smaller atoms like B, C, N and O are also present in steel either as additives or as impurities and their interaction with radiation induced point defects may lead to structural degradation of the steels. In order to gain fundamental knowledge about electronic structure aspects and the interaction of these solute atoms with point defects like vacancies, ab-initio DFT calculations are essential. The finer aspects of interactions among the point defects and small solute atoms present in ferritic and austenitic steels have been studied thoroughly using first-principle DFT calculations and are presented in this chapter. A systematic comparison is established among the four solute atoms (SA) and /or vacancies (V) by investigating Fe-SA, SA-SA and V-SA interactions in both the Fe-lattices.

7.1 Introduction

There have been a large number of studies focussing on interaction behaviour of Carbon (C), nitrogen (N), boron (B) and oxygen (O) in bcc-Fe lattice, whereas, a few studies are present in case of fcc-Fe lattice (section 2.6 of chapter 2). As far as we are aware of, there is no report available on the extensive investigation of C, N, B, O interactions and their interaction with vacancies in fcc-Fe. Further, there are conflicting reports present as far as stable position for B atom in bcc-Fe is concerned. Therefore, a comparison of point defects interactions in bcc-Fe and fcc-Fe systems will be particularly interesting, in view of wide applications of both the Fe systems.

In this chapter, we use extensive calculations using DFT to perform a systematic investigation of interaction between different complexes of foreign interstitial atoms C, N, B, O and their interaction with vacancies in both bcc-Fe and fcc-Fe lattices. The detailed investigation of interaction energies, density of states and differential charge densities of different complexes comprising one or more solute atoms and/or vacancies in the bcc-Fe and fcc-Fe lattices is presented. Wherever possible, comparison is made between the results for bcc-Fe and fcc-Fe lattices.

7.2 Computational details

7.2.1 First-principle calculations

The details of the DFT calculation are given in section 5.2.1 of chapter 5. Here, a 3×3×3 supercell containing 54 Fe-atoms for bcc-Fe and 108 Fe-atoms for fcc-Fe (in a defect free state) is used to investigate the interaction among the solute atoms (SA) (C, N, B,O) and their interaction with vacancies. The Monkhorst-Pack scheme is utilized to sample the K-points in Brillouin zone. A 6×6×6 K-point grid is chosen for bcc-Fe and 3×3×3 for fcc-Fe lattice. The spin-polarization effect is incorporated during the calculations to consider the magnetism in bcc-Fe lattice, whereas it is not considered for fcc-Fe. In order to find the minimum energy, the structures are optimized by relaxing supercell shape and volume as well as all atomic positions.

The formation enthalpy for a supercell containing N-atoms of Fe and one SA is calculated using eq. (5.1a) in chapter 5. The formation energy of vacancies is calculated using eq. (5.2) in chapter

5. For a supercell containing n-interacting entities (A1,A2….A_n))(for n>=2), the binding energy between the interacting entities in matrix is calculated using eq. (5.3) in chapter 5.

7.2.2 Verification of calculations

In order to verify the accuracy of our model (supercell size (54 atom in this case)) and methods (different parameters like energy cut-off, K-points to sampling etc. and different methodological details like DFT functionals, pseudopotential etc.) we have calculated the vacancy and di-vacancy formation energies in bcc-Fe and fcc-Fe and compared with the reported experimental as well as other computational results from the literature (Table 7.1). In Table 5.1 of chapter 5, our calculated results for bcc-Fe were compared with those from other first-principle and empirical calculations as well as experiments [1-8]. Our calculated results [9] are within the error bars of the experimental data and are consistent with the results from other computational studies. Similarly, our calculated results for elastic constants are also in agreement with other results. For the fcc-Fe lattice, results from other calculations are not available. These calculation yielded the lattice parameter of 3.445Å for fcc-Fe, this value is in good agreement with experimental [6] and other theoretical results [7]. We have also calculated the elastic constant for fcc-Fe lattices. We obtain C_{11} = 420 GPa C_{12} = 214 GPa and C_{44} = 239 GPa in fcc-Fe lattice, the values are consistent with other theoretical [7,10] and experimental results [8].

Table 7.1 Formation energies (in eV) of Vacancy and divacancy (first and second nearest neighbor) in fcc-Fe lattices.

Method	FCC Fe	
	Vacancy	Divacancy

		1NN	2NN
This work (PAW-PBE)	2.3	0.16	-0.09
Experimental value[a]	1.7±0.2		

[a]Reference [5]

7.3 Results and discussion

7.3.1 Single SA (C, N, B, O) in bcc-Fe and fcc-Fe

7.3.1.1 Stability of SA

It is well known that the small solute atoms usually occupy the interstitial sites in transition metals. In bcc-Fe and fcc-Fe lattices, there are two types of solution sites, namely (a) interstitial sites [octahedral (O-site) and tetrahedral (T-site)] and (b) substitutional sites (S-site). We have calculated the formation energies of all the four SAs, namely C, N, B, O at different sites in bulk bcc-Fe as well as fcc-Fe using eq.(7.1) and the corresponding results are summarized in Table 7.2.

Table 7.2 Formation enthalpies (in eV) and Bader-charges for single SAs (C, N, B, O) in bcc-Fe and fcc-Fe lattices, positioned at two different interstitial sites and a substitutional site. Energy entry with the symbol (O) signifies that SA positioned at T site initially, relaxes to octahedral position after optimization using full ionic relaxation.

		BCC Fe				FCC Fe			
Configuration	Property	C	N	B	O	C	N	B	O
	Formation-	-4.956	-2.186	-5.725	-2.303	-6.160	-4.805	-6.277	-2.970

Substitutional	enthaply	(-8.742)^{a}	(-2.387)^{a}	(-5.37)^{b}	(-2.31)^{d}				
	Bader-charge	-0.98	-1.09	-0.55	-1.0	-0.96	-0.99	-0.34	-0.92
Tetrahedral	Formation-enthaply	(O) (-9.787)^{a}	(O) (-4.407)^{a}	-5.024 (-4.77)^{c}	-3.445 (-3.19)^{d}	-6.269	-6.758	-3.497	-4.688
Octahedral	Formation-enthaply	-7.337 (-10.710)^{a}	-5.234 (-5.196)^{a}	-5.695 (-5.20)^{b}	-3.963 (-3.75)^{d}	-9.142	-8.880	-6.507	-5.564
	Bader-charge	-1.07	-1.18	-0.51	-1.06	-0.99	-1.11	-0.44	-1.06
	Calculated atomic radii (Å) [11]	0.67	0.56	0.87	0.48				

^{a}Reference [12], ^{b}Reference [13], ^{c}Reference [14], ^{d}Reference [15]

Based on the formation enthalpy results, the most stable position for C, N and O atom is the O-site in both bcc-Fe and fcc-Fe lattices and it is in agreement with the experimental observations [16] and other theoretical results [12,15]. The energy difference between the octahedral and substitutional occupancies for C, N and O in both the bcc- and fcc-Fe lattices is found to be large and it is more than 1.5eV. We are unable to calculate formation enthalpy of C and N atoms at T-site (in bcc-Fe), as the starting tetrahedral configuration always relaxes to the O-site configuration. Interestingly, B atom is more stable at S-site in bcc-Fe with a small energy difference to the O-site, and the present result is in agreement with the previous calculations [13-14]. It is interesting to note that this energy difference is as small as thermal energy (k_BT) at room temperature and therefore whether B atom will occupy octahedral interstitial site or substitutional site in a bcc Fe lattice will very much depend on the temperature of the system. In contrast, in the fcc-Fe lattice, the O-site is favourable as compared to S-site for B atom also like other SAs considered. In general, small atoms (C, N, B, O) in fcc-Fe lattice forms more stable complex than the corresponding complex in bcc lattice (see magnitude of formation energies in bcc and fcc for stable positions in Table 7.2). Among various SAs considered here, C atom forms the most stable complexes with iron in both bcc and fcc iron lattices.

The atomic sizes [11] of B, C, N and O atoms (see Table 7.2) are small enough to allow interstitial occupancy but large enough to yield significant lattice distortion. In case of bcc-Fe, O-site is more preferred for SA over the T-site even though the size of T-site is larger than O-site. The rationale behind this behaviour is that the O-site has only two nearest neighbour Fe-atoms, making strain relief more favourable than that at T-site with four nearest neighbour Fe-atoms [14,17]. The atomic radii of B atom is the largest among all SAs considered here (i.e. B, C, N and O), and as a consequence, if it is in interstitial position, it will entail more strain in bcc-Fe lattice by displacing the nearest Fe-atoms. This displacement is comparatively small for substitutional occupancy, and therefore, B atom occupies the S-site rather than O-site in bcc-Fe. On the other hand, the size of O-site in fcc-Fe is larger than that in bcc-Fe, and thus it explains why B atom is stable in the O-site in case of fcc-Fe. From the calculated Bader-charges (Table 7.2) it is observed that the octahedral occupancy results in larger charge transfer to C, N and O atoms as compared to substitutional sites in both the Fe-lattices. However, in the bcc-Fe lattice, the extent of charge transfer in substitutional B is more than that in octahedral B, whereas in fcc-Fe case, it is the reverse.

7.3.1.2 Density of states

In order to understand detail bonding characteristics, we have calculated the projected density of states (PDOS) for the iron atoms in the first nearest neighbours to the C, N, B and O solute atoms as well as for the solute atom itself in bcc-Fe and fcc-Fe lattices as shown in Figure 7.1(a-h) and

Figure 7.2(a-h) respectively. Comparison of the density of states (DOS) of pure Fe 3d states with that of the 1NN Fe atoms to the solute atoms occupying the octahedral site in bcc-Fe lattice reveals that there is a depletion of 3d states in Fe-SA systems as compared to that in pure Fe. However, no such trend is observed in the case of fcc-Fe systems. It is observed from PDOS that the hybridization between 1NN Fe 3d states and SA 2p states is stronger for octahedral SA than for substitutional SA in both the Fe-lattices. The strong hybridization between 1NN Fe 3d and SA 2p state of octahedral B, C, N and O atoms is observed in bcc-Fe which is in good agreement with other calculations [12-13,15]) and a similar hybridization trend is observed in fcc-Fe as well. On the other hand, no such strong hybridization is observed when the SA is located at substitutional position in both the Fe-lattices. Interestingly, the strength of hybridization appears to depend not only on the solute position in lattice but also on solute nature and is increasing in B<C<N<O order for both the Fe-lattices. The energy ranges of the strong hybridization between 1NN Fe 3d and SA 2p states decrease noticeably in B>C>N>O order in both Fe-lattices as shown by black dashed vertical lines in Figure 7.1 & 7.2. The highest energy range for the B atom and the lowest energy range for the O atom indicate less localized interaction of B atom than of O atom with Fe atoms (see Figure 7.1(i) and 7.2(i)) in both the Fe-lattices. Thus, the Fe-SA interaction is becoming more confined in B<C<N<O order in both Fe-lattices. However, why B atom is more stable in substitutional position rather than in octahedral position cannot be explained on the basis of hybridization.

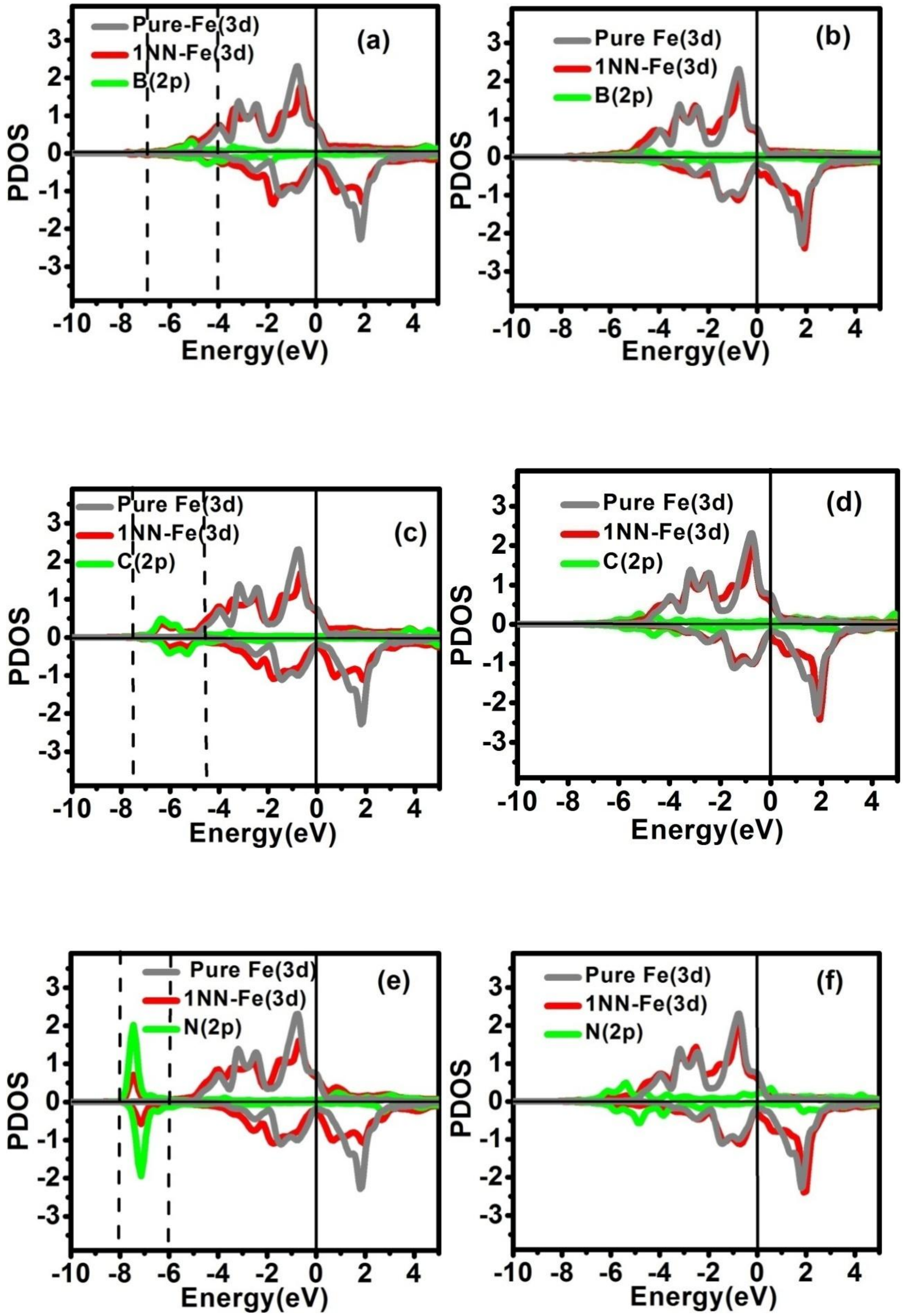
(a)
Pure-Fe(3d)
1NN-Fe(3d)
B(2p)
PDOS
3
2
1
0
-1
-2
-3
-10
-8
-6
-4
-2
0
2
4
Energy(eV)
(b)
Pure Fe(3d)
1NN-Fe(3d)
B(2p)
PDOS
Energy(eV)
(c)
Pure Fe(3d)
1NN-Fe(3d)
C(2p)
PDOS
Energy(eV)
(d)
Pure Fe(3d)
1NN-Fe(3d)
C(2p)
PDOS
Energy(eV)
(e)
Pure Fe(3d)
1NN-Fe(3d)
N(2p)
PDOS
Energy(eV)
(f)
Pure Fe(3d)
1NN-Fe(3d)
N(2p)
PDOS
Energy(eV)

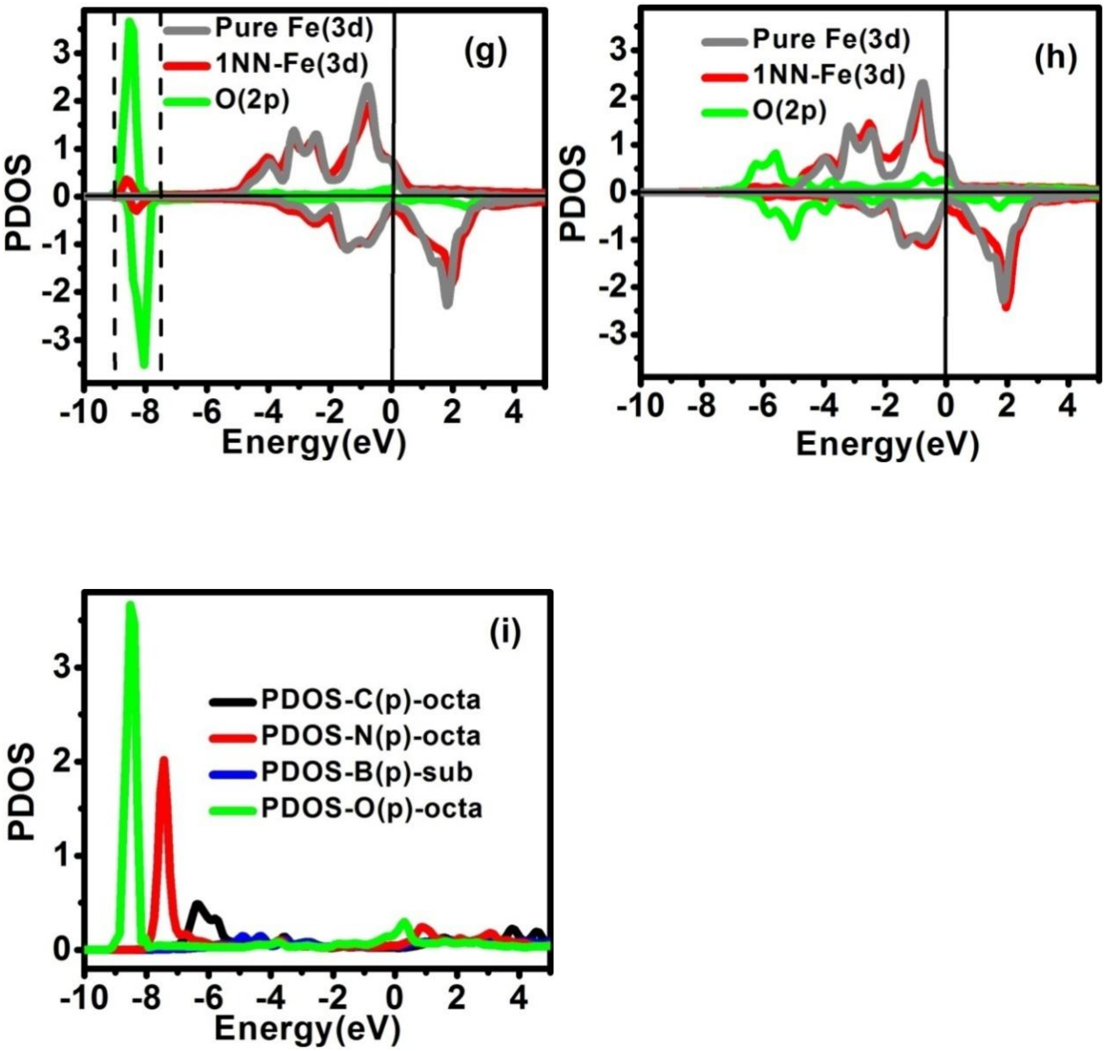

Figure 7.1. PDOS calculated for bcc supercell containing 54 Fe atoms and one SA (C, N, O and B) positioned at octahedral (a, b, c, d) and substitutional (e, f, g, h) sites in bcc-Fe lattice. (i) p-states of C, O and N at Octahedral site and B at substitutional site in bcc-Fe. Pair of black dashed lines shows the energy range for strong hybridization between Fe 3d and SA 2p states.

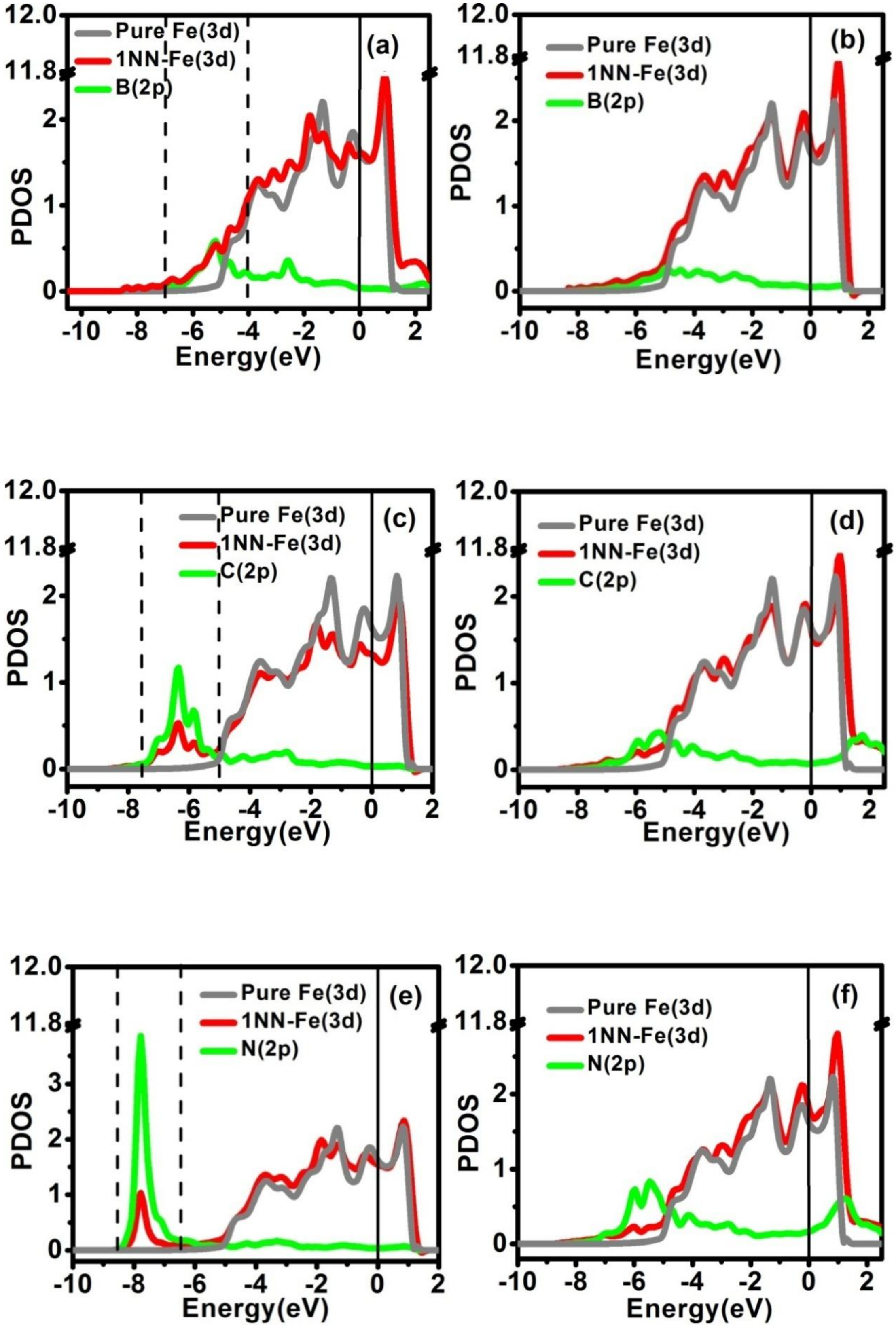

(a)
Pure Fe(3d)
1NN-Fe(3d)
B(2p)
(b)
Pure Fe(3d)
1NN-Fe(3d)
B(2p)
(c)
Pure Fe(3d)
1NN-Fe(3d)
C(2p)
(d)
Pure Fe(3d)
1NN-Fe(3d)
C(2p)
(e)
Pure Fe(3d)
1NN-Fe(3d)
N(2p)
(f)
Pure Fe(3d)
1NN-Fe(3d)
N(2p)
PDOS
12.0
11.8
3
2
1
0
Energy(eV)
-10
-8
-6
-4
-2
0
2

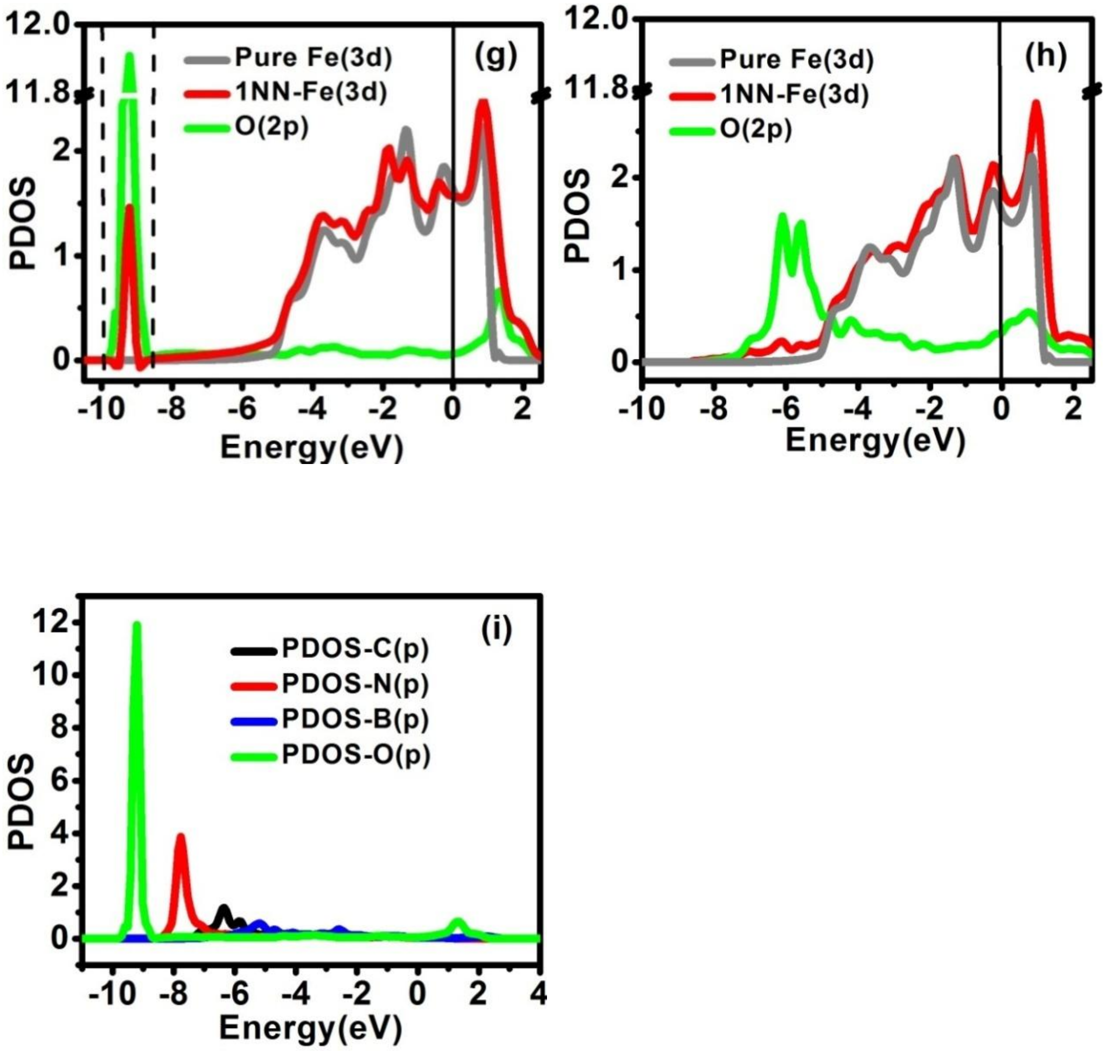

Figure 7.2. PDOS calculated for fcc supercell containing 108 Fe atoms and one SA (C, N, O and B) positioned at octahedral (a, b, c, d) and substitutional (e, f, g, h) sites in fcc-Fe lattice. (i) p-states of C, N, B and O at Octahedral site in fcc-Fe. Pair of black dashed lines shows the energy range for strong hybridization between Fe 3d and SA 2p states.

7.3.1.3 Differential charge density

In order to gain further insight, the interaction between SAs and neighbouring Fe atoms are examined with the help of differential charge densities as shown in Figure 7.3 & 7.4. The differential charge density is defined as the difference between the charge density of (I) Fe-system containing interstitial atom, (II) the superposition densities of host Fe and the free interstitial. It can be seen (see Figure 7.3 & 7.4, upper and lower panels) that in both bcc and fcc-Fe systems with solute atom at octahedral position, charge transfer between SA and the nearest neighbour Fe atoms is much more as compared to the same in substitutional solute case. This result supports our PDOS results as well. It is noteworthy that in both the Fe-lattices, the contour deformation of charge density around octahedral solute atom decreases in B>C>N>O order. It possibly depends on the size of the solute atom, as atomic radii of the SA follow the same trend. However, the extent of charge transfer follows the order O>N>C>B, indicating stronger interaction in case of O-atom and least in case of B-atom. It is to note that although B is stable in substitutional position, charge transfer between the B atom and the Fe neighbours in this case is substantially weaker than that in octahedral B case. It is also observed that in bcc-Fe with the octahedral substituent, localized charge transfer occurs between the solute atom and both first and second nearest neighbours. In contrast, in fcc-Fe systems, the solute atom strongly interact with 1NN Fe atoms through strong and localized charge transfer and a very weak and delocalized charge transfer is observed in case of 2NN Fe atoms. This mainly depends on the distance of SA and neighbour Fe atoms. As in case of bcc-Fe, this distance is 1.77 Ǻ and 1.97 Ǻ for 1NN and 2NN Fe atoms respectively and the same in fcc-Fe is 1.86 Ǻ and 3.04 Ǻ. Hence, there is no significant charge transfer among SA and 2NN Fe atom in fcc-Fe as compared to bcc-Fe. The range and strength of charge transfer between SA and the neighbouring Fe atoms is more in bcc-Fe than in fcc-Fe systems. Like bcc-Fe systems, in fcc-Fe also, the extent of charge transfer follows the order O>N>C>B.

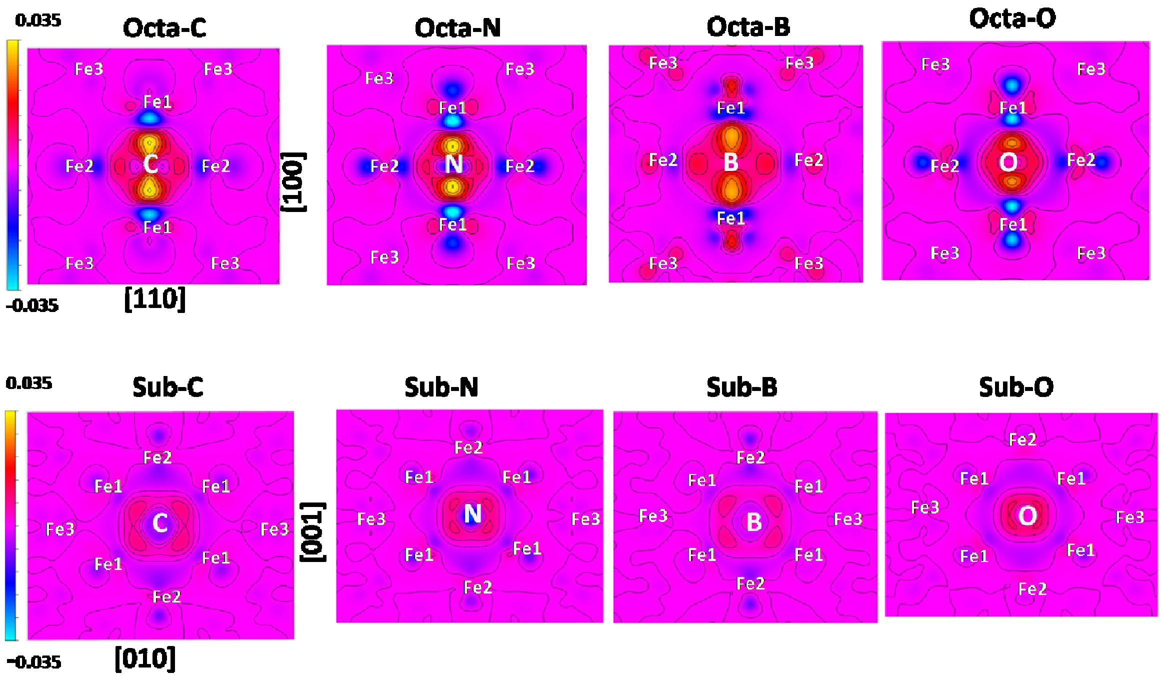

Figure 7.3. The differential charge density distribution for C, N, B and O atom at octahedral and substitutional site in bcc-Fe lattice. The plots show the charge distribution of SA and their nearest neighbour Fe-atom.

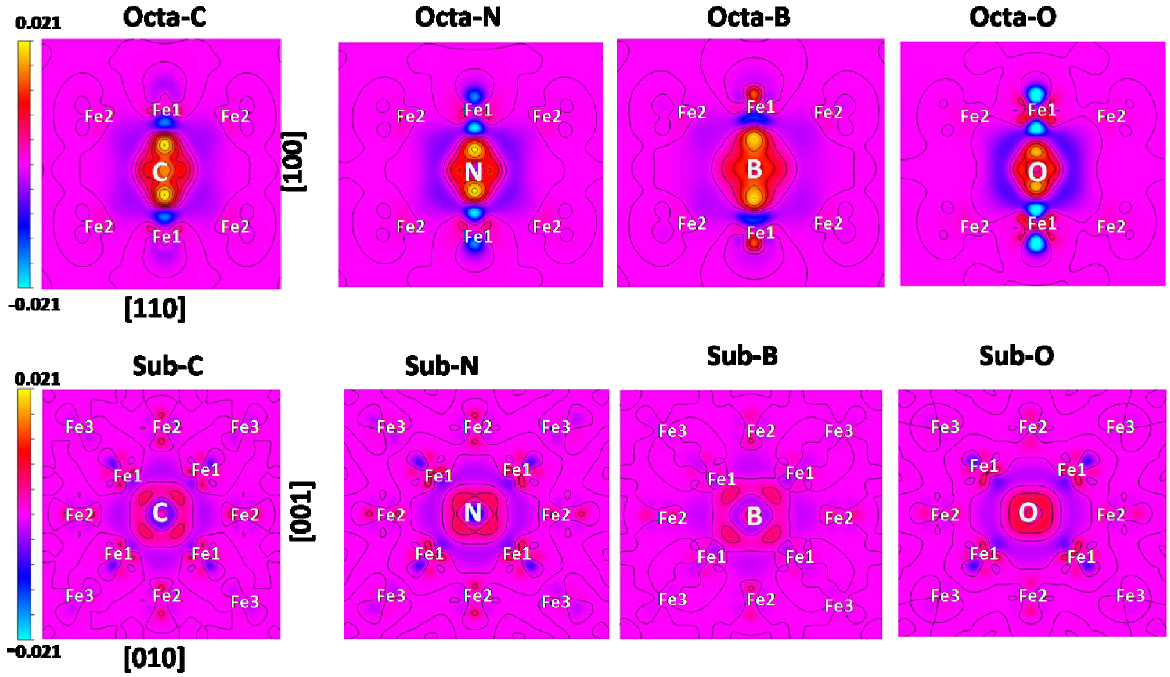

Figure 7.4. The differential charge density distribution for C, N, B and O atoms at octahedral and substitutional site in fcc-Fe lattice. The plots show the charge distribution of SA and their nearest neighbour Fe-atom.

7.3.1.4 Local magnetic moment

The change in the local magnetic moment of neighbouring Fe atoms is observed after interaction with SA in bcc-Fe lattice. Indeed, as also mentioned in previous DFT study [12] that after interaction with the solute atom, population of the minority-spin d states of 1NN Fe atoms is larger than that in pure bcc-Fe. This leads to the decrease in local magnetic moment of 1NN Fe atoms. The local magnetic moments of Fe atoms as well as SAs are tabulated in Table 7.3. The presence of SAs strongly influences the magnetic moment of closest Fe atoms. It is clearly seen that the local magnetic moment of the 1NN Fe decreases substantially for all solute atoms. As the distance between Fe atom and SA is increasing, the local magnetic moment increases and tends towards the local moment of pure Fe. Furthermore, the calculated local magnetic moment for 3NN Fe atoms (see Table 7.3) is more than that of pure bcc Fe as also observed in an earlier study [12].

Table 7.3 Local magnetic moment carried by SA's and their neighbours in bcc-Fe after relaxation. For Fe atom in perfect bcc supercell, the local magnetic moment is 2.24 μ_B/atom.

Configuration		C (μ_B/atom)	N (μ_B/atom)	B (μ_B/atom)	O (μ_B/atom)
Octahedral	SA	-0.145	-0.115	-0.16	0.039
	Fe-1NN	1.658	1.654	1.729	1.972
	Fe-2NN	2.207	2.208	2.232	2.381
	Fe-3NN	2.404	2.42	2.385	2.41
	SA	-0.102	0.005	-0.145	0.221
	Fe-1NN	2.249	2.375	2.221	2.478

Substitutional	Fe-2NN	2.237	2.217	2.194	2.229
	Fe-3NN	2.291	2.292	2.24	2.285

7.3.2 Interaction with point defects in bcc-Fe and fcc-Fe

7.3.2.1 SA-SA interactions

We characterize the interaction of two solute atoms at either octahedral position or substitutional position depending on their stability in bcc-Fe and fcc-Fe lattices. In our calculations, B atom is positioned at S-site in bcc-Fe and O-site in fcc-Fe, whereas other solute atoms (C, N and O) are positioned at O-site in both the Fe lattices. In particular, we have calculated the distance dependent interaction energy for different configurations (see Figure 7.5 & 7.6) of two SAs in bcc-Fe and fcc-Fe.

(i) bcc-Fe

In order to compare the interaction among different solute atoms, binding energy is calculated for the same set of configurations for C, N and O atoms (see Figure 7.5(b) for different configurations), as they all occupy octahedral interstitial position. However, the configurations for B atom are quite different (see B-B and B-SA, where SA=C, N, O, configurations in Figure 7.5(d) and (e) respectively) due to its substitutional occupancy. Our calculated results for different interactions in bcc-Fe systems are in very good agreement with the previous results [12]. From Figure 7.5(a) it is observed that in case of C, N and O atoms, the homo and hetero atom interactions between any two solute atoms are repulsive at shorter distances for the configurations explored here. It implies that C, N and O atoms prefer to stay away from each other. Among all the investigated interactions, N-N interactions are the most repulsive one as compared to other interactions. The configurations corresponding to larger inter-solute distances show attractive interaction. In particular, the O-O interactions in configurations **cfg2** and **cfg3** as seen from Figure 7.5(a) are considerably attractive. The distance dependent interaction between any two isolated atoms generally follows the general behaviour that it is repulsive at short range and attractive (as a result of dipole-dipole interaction) at intermediate range, finally going to zero at longer range. It is embedded in the Fe matrix. Domain et al. [12] reported only repulsive inter-solute interaction, which is different from the present result. However, they also obtain attractive interaction in some of the configurations when larger system size is considered. It is to note that we also recovered similar results (all repulsive) as Domain et al. [12] by using their methods with fixed volume calculation. The present result that attractive interaction exists at intermediate inter-solute distances has also been observed in a recent study [15].

For B atom, the binding energies of sub-sub (B-B) and sub-oct (B-SA, where SA=C/N/O) configurations are shown in Figure 7.5(c). It is observed that B-B interaction is significantly attractive in nature at shorter distances unlike in the cases of C-C, N-N, O-O, C-N, C-O and N-O complexes, in which repulsive interaction is observed at short distances. Further, B interaction with C, N and O are also attractive in nature at shorter distances even though these distances are smaller as compared to the corresponding distances for C, N and O interactions with each other (Figure 7.5(a) & (c)). This implies that the behaviour of B atom is completely different as compared to C, N and O atoms in the bcc-Fe systems. This might be due to the difference in preferential site i.e. S-site for B occupancy and O-site for occupancy of C, N and O atoms in bcc-Fe systems. This attractive interaction energy between B and other solute atoms is mainly due to the geometrical arrangement of the 1NN Fe atom with B at S-site and C/N/O at O-site. It is observed that the substitutional B atom tends to contract 1NN Fe-B distances, whereas octahedral SA=C/N/O tends to elongate the 1NN Fe-SA distances. However, larger SA-Fe distance in the former case than that in the latter might be reason for introducing less strain in the former, hence giving rise to attractive interaction energy [7]. The binding energy of substitutional and octahedral B atom is reported earlier in a few reports [7,18]. The repulsive interaction of octahedral B with other octahedral B and C atom in bcc-Fe is reported by He *et al.* [18]. However, Balaon *et al.* [7] confirmed the attractive interactions for substitutional B atom with B, C, N and O atoms at short distances, which corroborates our results. This implies that the interaction nature of B atom in bcc-Fe depends significantly on its preferential site. From our calculations, B atom has a tendency to bind to the point defects, this has been confirmed experimentally [19] as well. As the B atom is in substitutional position and smaller in size than the substituted Fe atom, it helps other impurity atoms to relieve strain in the lattice, resulting in attractive binding energy. However, at larger distances the interaction becomes negligible here as well. The range i.e. the inter-solute distance beyond which interaction is negligible, for B-B interactions is about 4.90 Ǻ and that for B-C or B-N or B-O interactions is around 5.34 Ǻ.

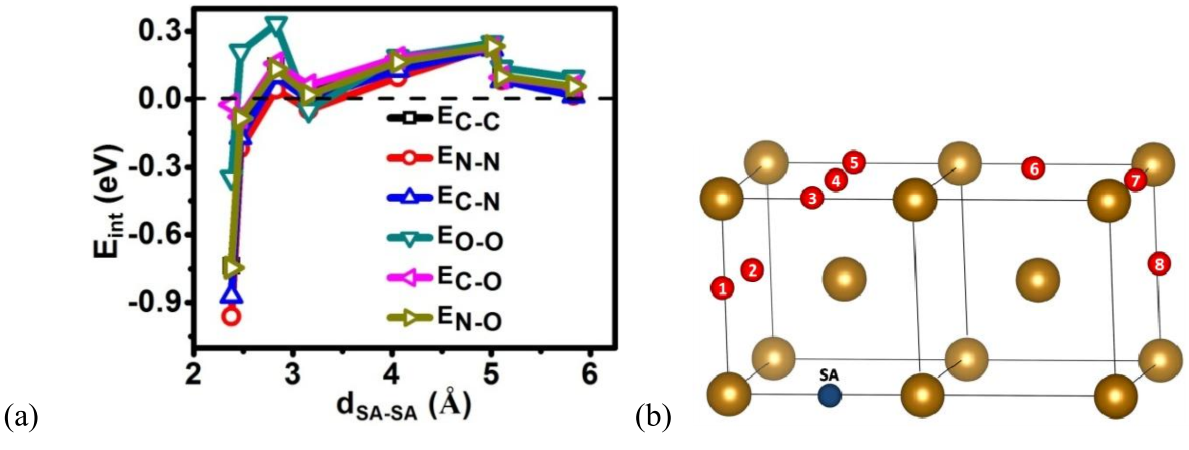

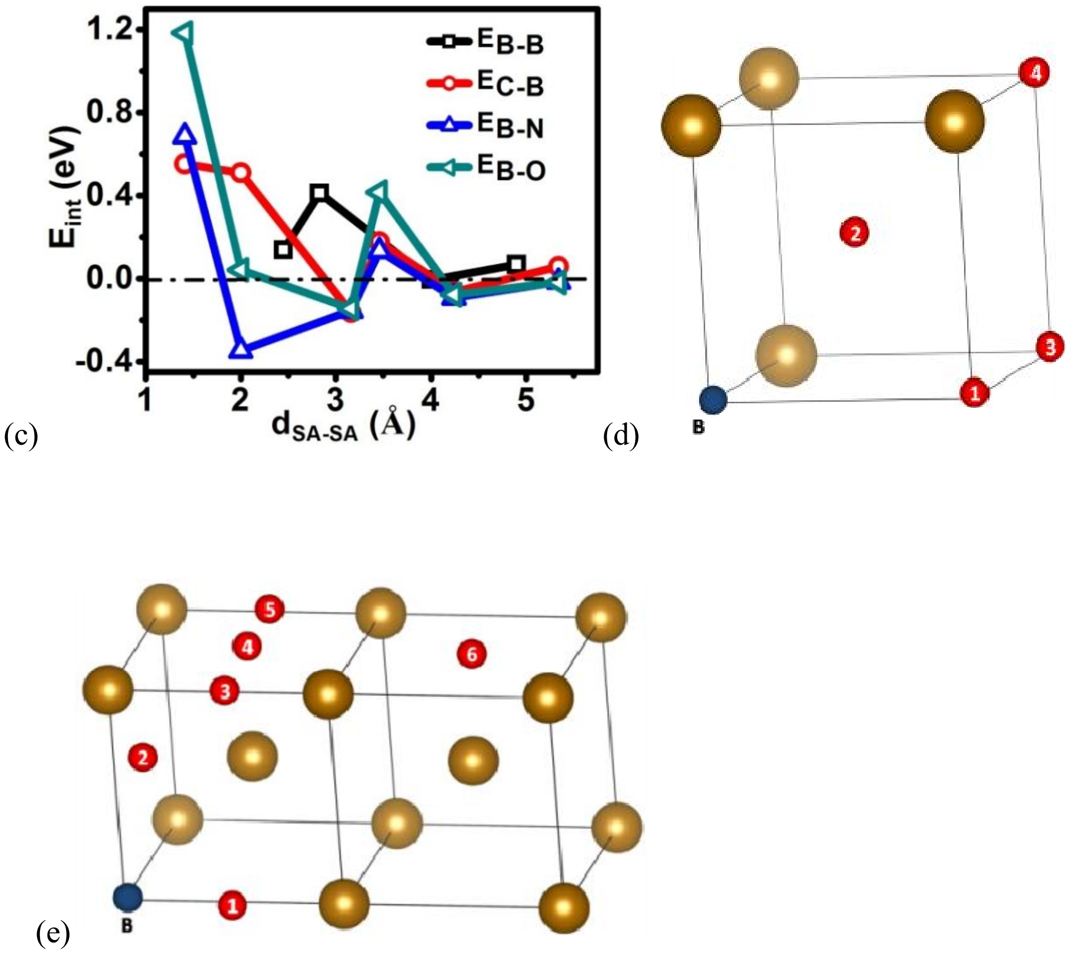

Figure 7.5. (a) Binding energies of SA-SA pairs (SA=C, N and O) as a function of the distance between two SA's in bcc-Fe and (b) the corresponding SA-SA configurations. (c) Binding energies of SA-B pairs and different investigated configurations for (d) B-B and (e) SA-B(SA=C, N and O) interactions.

(ii) fcc-Fe

As it has been discussed in earlier section, in fcc-Fe, all C, N, B and O atoms prefer to occupy the O-site, therefore interaction energy is calculated at the same configurations (Figure 7.6 (b)) for all solute atoms. The binding energy of different possible SA-SA configurations as a function of inter-solute distance is depicted in Figure 7.6 (a). It is observed that all the interactions are repulsive at shorter distances, implying that in fcc-Fe systems all solute atoms prefer to stay away from each other. The repulsive interaction between two solute atoms decreases as distance increases and at a larger distance, interaction becomes negligible. Up to an inter-solute distance of 6.44 Å, the interaction between any two solute atoms is found to be repulsive without going through attractive region. Here, the N-N interaction is the most repulsive and B-B interaction is the least repulsive. Unlike bcc-Fe systems, the interaction behaviour of B atom is similar to that of C, N and O atoms in fcc-Fe systems. The main difference between the interactions in bcc-Fe and fcc-Fe lattices arises in case of B and O atoms. In fcc-Fe, B atom has always repulsive interactions with all solute atoms, whereas it binds with other solute atoms in bcc-Fe lattices. In contrast to the bcc-Fe systems, in fcc-Fe systems, O-O interaction is always repulsive, implying that the formation of O agglomerate in fcc-Fe is not as easy as in case of bcc-Fe. The range of interaction between any two solute atoms in the fcc-Fe system is around 6.44 Å. As interaction is repulsive here, beyond the inter Fe-SA distance of 6.44 Å, stable Fe-SA complex may be obtained.

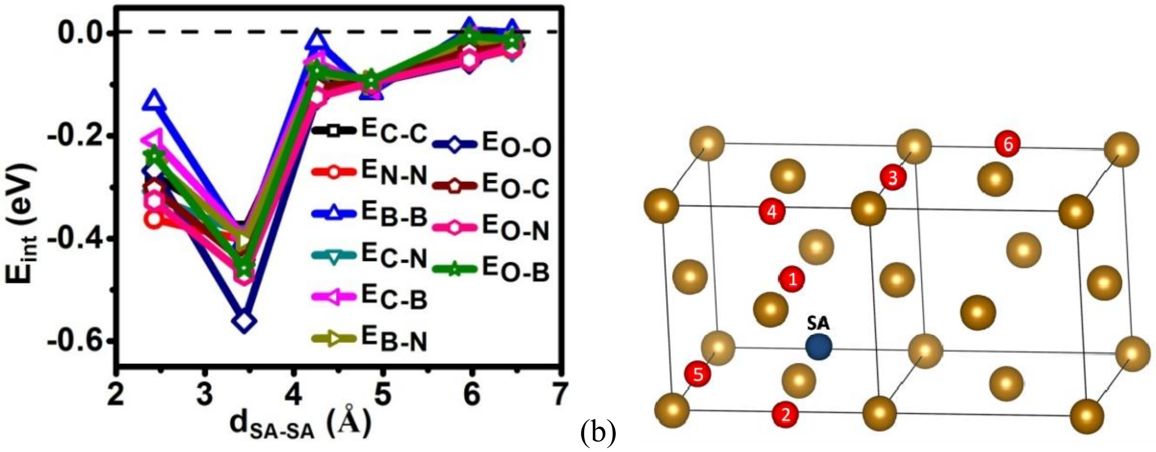

(a)

(b)

Figure 7.6. (a) Binding energies of SA-SA pairs as a function of the distance between two SA's in fcc-Fe for SA = C, N, O, B (both at oct –oct position) complexes (b) different configurations for SA-SA interactions in fcc-Fe lattice.

7.3.2.2 One SA-one vacancy interactions

The configurations investigated for one solute with one vacancy interactions are represented in Figure 7.7 for both the Fe-lattices. The distance dependent binding energies for bcc-Fe and fcc-Fe systems are displayed in Figure 7.7 (a) & (d) respectively. The configurations considered for V-B and V-SA (SA=C/N/O) interactions in the bcc-Fe lattice are shown in Figure 7.7 (b) and (c) respectively. The configuration for V-SA interaction in the fcc-Fe lattice is shown in Figure 7.7 (e)

(i) In bcc-Fe and fcc-Fe

From the calculated binding energies it is clear that vacancy tends to bind B, C, N and O atoms at shorter distances in both the Fe-lattices. All the SAs form stable vacancy-solute pair due to trapping effects, which support the fact that solute near a vacancy does not become substitutional and the $d_{V\text{-}SA}$ does not vanish. The V-B interaction at the minimum V-B distance considered here is more attractive than other V-SA interaction in fcc-Fe systems, whereas it is not so attractive in bcc-Fe systems. It is mainly due to stable substitutional position for the B atom in bcc-Fe system. As a result, minimum distance between a vacancy and a B atom is more in bcc-Fe systems than that in fcc-Fe systems. Therefore, it becomes difficult to compare B-V interaction in these two different lattices. Interestingly, it is to observe that the B-SA (=B, C, N, O) interaction curves in

Figure 7.5 (c) resemble with the V-SA (=B, C, N, O) interaction curves in Figure 7.7 (a) for the bcc-Fe systems. It suggests that B atom behave like a vacancy in the bcc-Fe lattice. In fcc-Fe systems, however, interaction of B atom with any other SA is repulsive in nature (Figure 7.6(a)), but vacancy interacts with the SA with attractive interaction.

In both the lattices, the V-SA interaction energy strength is decreasing in O>N>C order (in agreement with other calculations [15]), whereas atomic radii of these SAs are showing the opposite trend (Table 7.2), i.e. decrease in C>N>O order. It suggests that V-SA interaction is effectively determined by the atomic dimension of impurity atom. The attractive V-SA interaction may be due to the fact that a vacancy next to the impurity atom allows the system to relieve strain that will observe in absence of a vacancy. The only exception to this general trend is the V-B interaction which is stronger than other V-SA interaction, although B atom is having the largest atomic size among all the SAs. It is to note that for nearest neighbour V-B interaction, B atom is relaxing towards vacancy site and becomes substitutional atom in fcc-Fe lattice. The V-SA interaction strength is always stronger in bcc-Fe than in fcc-Fe (Figure 7.7 (a) & (d)), indicating stronger vacancy trapping ability in the former lattice (well in agreement with previous result [18]).

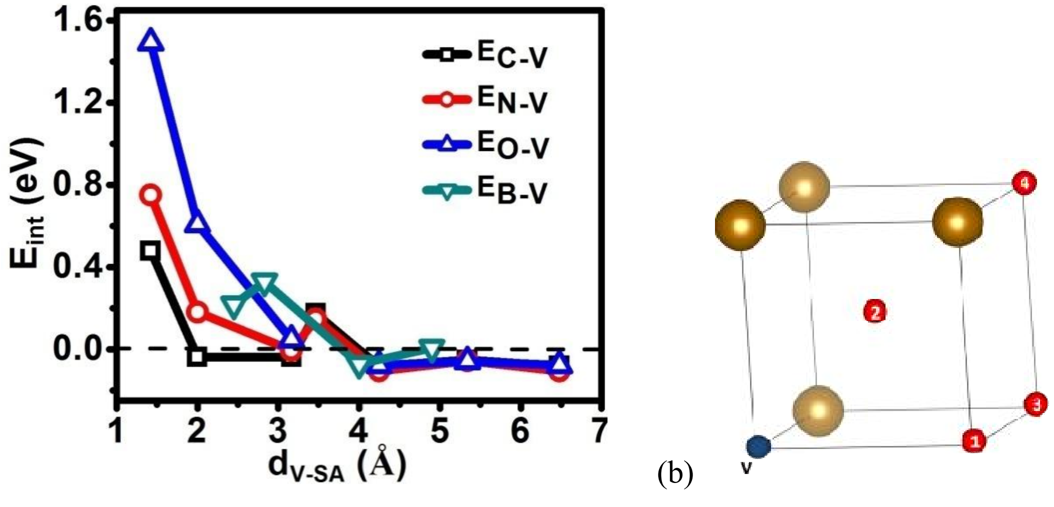

(a)

(b)

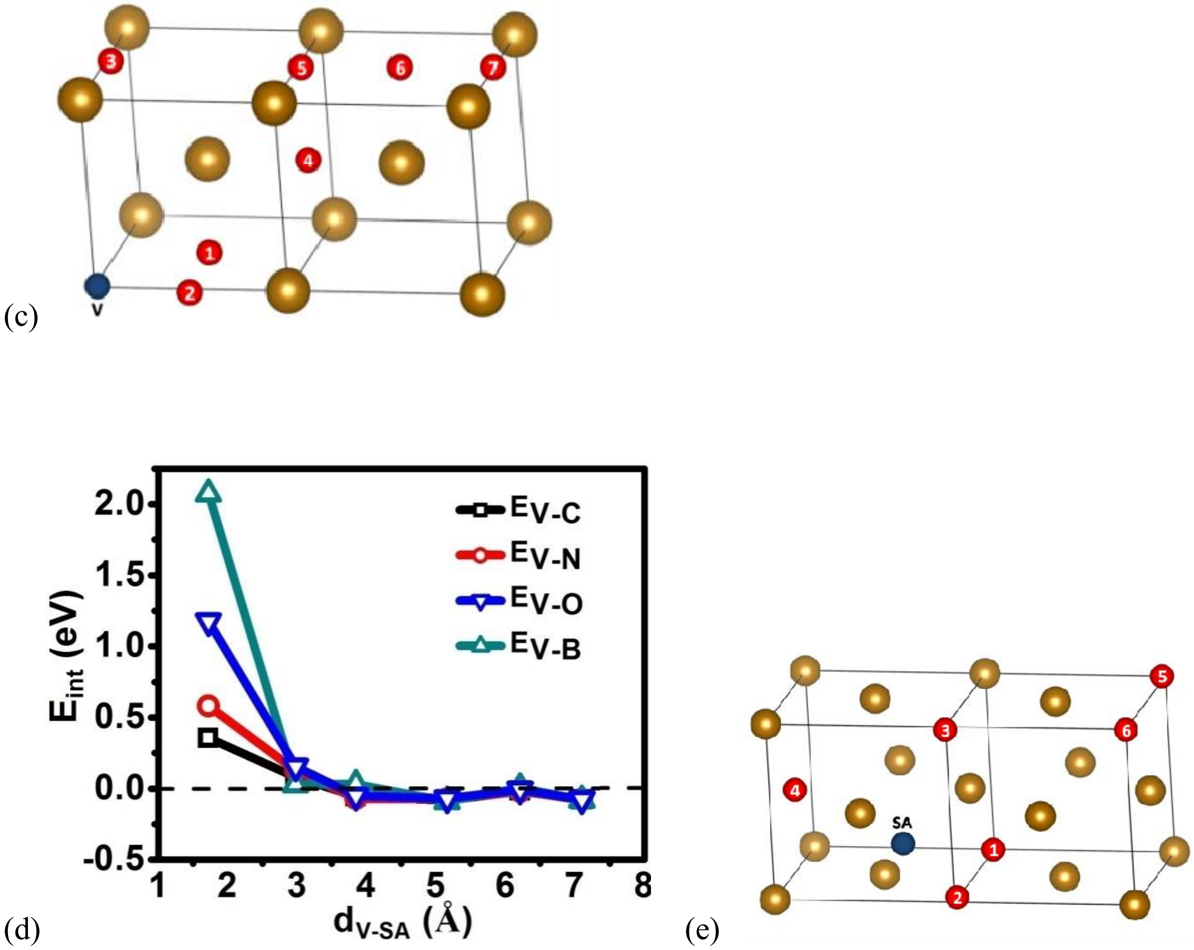

Figure 7.7. (a) Binding energies of V-SA (SA = C, N, O, B) pairs as a function of V-SA distance in bcc-Fe lattice. The investigated configurations are displayed in (b) for B-V complex and (C) V-SA (SA = C, N, O) complex in bcc-Fe lattice. (d) Binding energy for V-SA (SA = C, N, O, B) complexes in fcc-Fe lattice and corresponding configurations are shown in (e).

To illustrate the results further, we have calculated the differential charge density to analyze the interaction between vacancy and SAs for highest stable configuration in bcc-Fe and fcc-Fe.

Corresponding contour plots are shown in Figure 7.8. It is observed that in bcc-Fe, the charge distribution between SA and vacancy has become more negative in C>N>O>B order, which is in line with V-SA binding energy results. The same behaviour is observed for fcc-Fe for C, N and O atoms, whereas, B atom is moved towards vacancy during relaxation and become substitutional SA for nearest neighbour V-SA configuration only (for **cfg1** in Figure 7.7(e)).

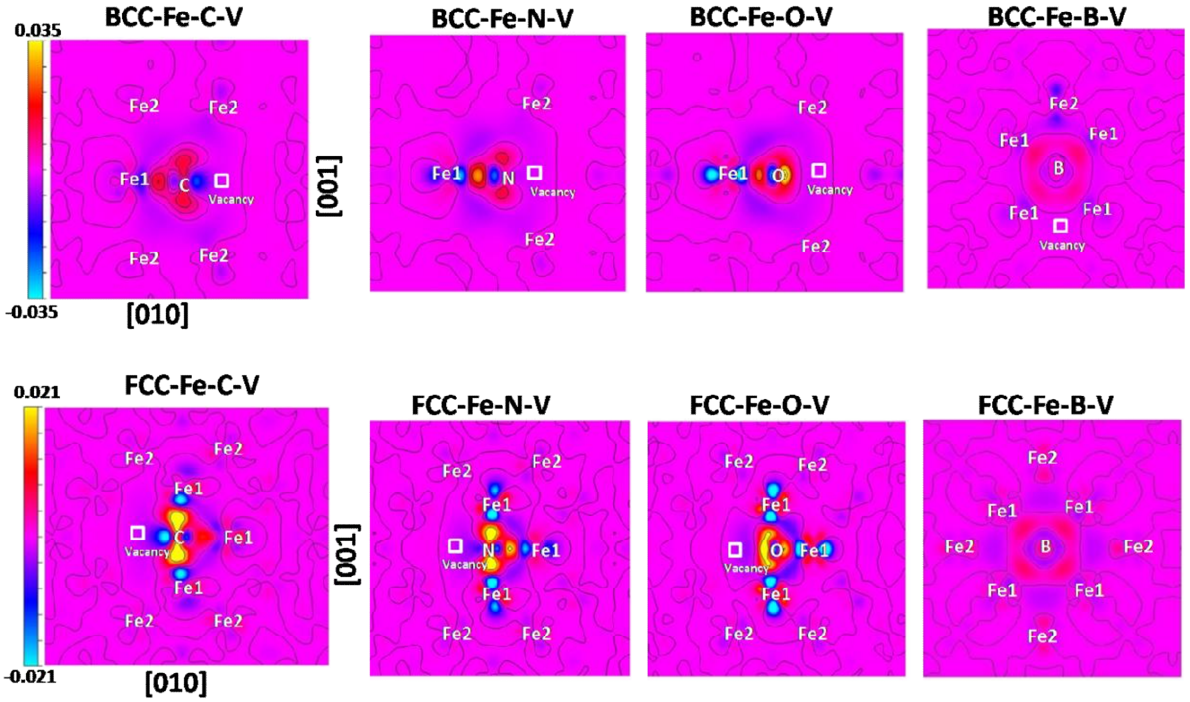
BCC-Fe-C-V BCC-Fe-N-V BCC-Fe-O-V BCC-Fe-B-V

FCC-Fe-C-V FCC-Fe-N-V FCC-Fe-O-V FCC-Fe-B-V

Figure 7.8. The differential charge density distribution for vacancy with C, N, B and O atoms in bcc- and fcc-Fe lattices. The charge distributions of SA and their nearest neighbour Fe-atoms are shown here.

7.3.2.3 Two SA - one vacancy interactions

The investigated configurations for two solute atoms and one vacancy are represented in Figure 7.9 (a), (b), (c), (d) & (e).

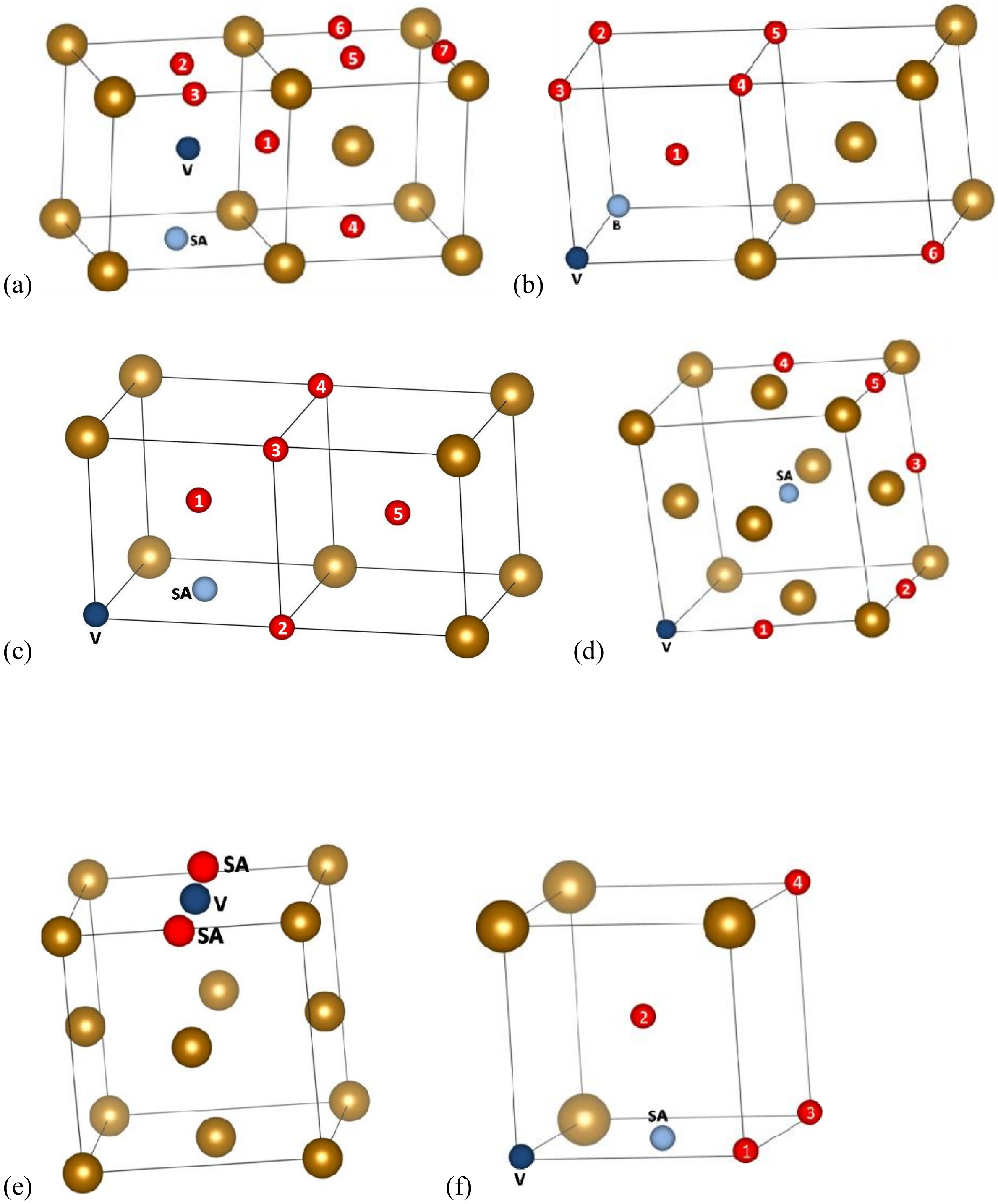

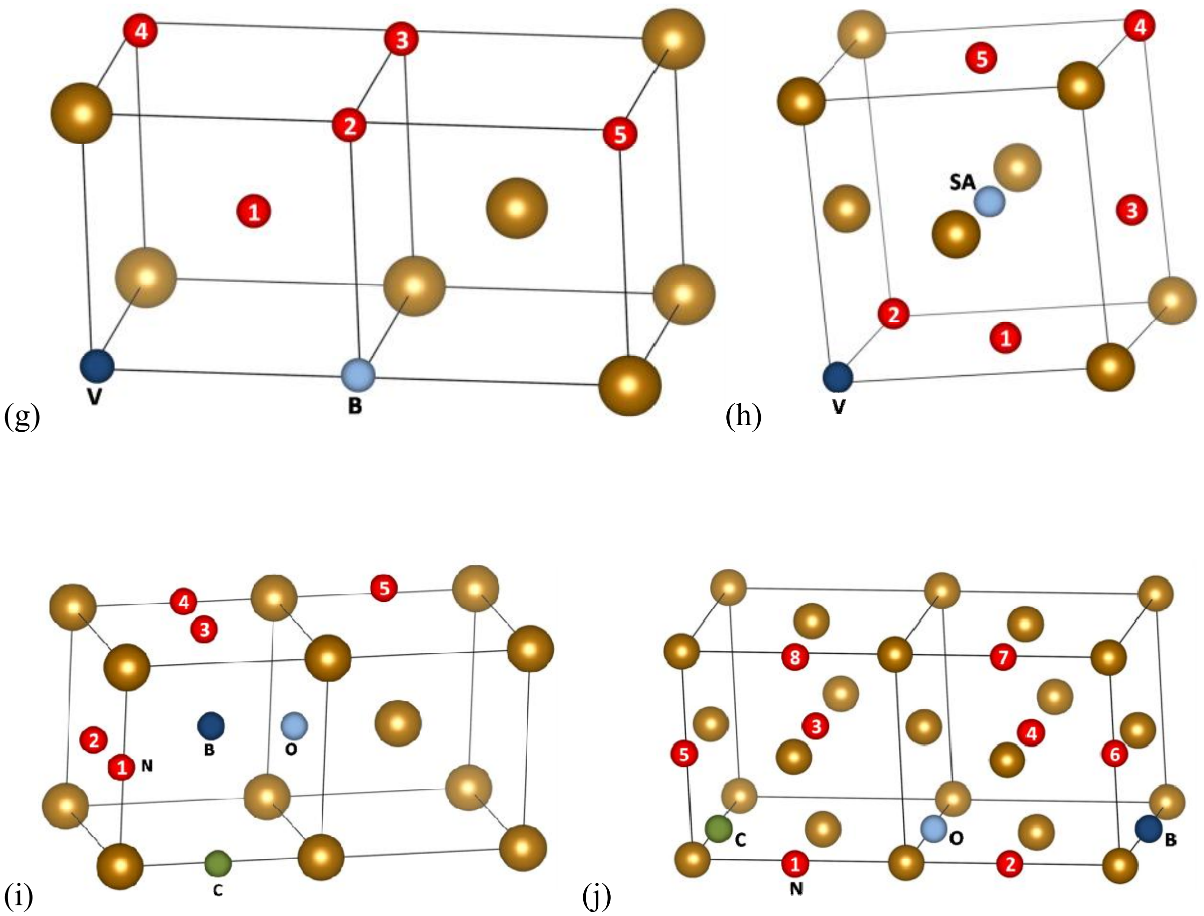

Figure 7.9. Schematic representation of the investigated configurations for V-SA_2 for (a) C, N and O atom (b) B atom (c) B atom with C, N and O in bcc-Fe lattice (d) C, N, B and O atom in fcc-Fe lattice (**cfg1** to **cfg5**) (e) C, N, B and O atom in fcc-Fe lattice (**cfg6**). And the investigated configurations for V_2-SA for (f) C, N and O atom in bcc-Fe lattice (g) B atom in bcc-Fe lattice (h) C, N, B and O atom in fcc-Fe lattice. The four solute interaction configurations are (i) C-N-B-O in bcc-Fe lattice with C, B and O are at fixed position (j) C-N-B-O in fcc-Fe lattice with C, B and O are at fixed position.

(i) In bcc-Fe

We have explored the interaction of one vacancy with two SAs of same as well as of different identity in bcc-Fe systems and the results are summarized in Table 7.4. During these calculations V-SA and SA-SA distances are varied in order to get different configurations. It can be seen from Table 7.4 that the most stable configuration for C atoms in V-C_2 complex is different from that of V-N_2 and V-O_2 complexes. The C atoms favour to be in two closest octahedral sites i.e. **cfg1**, whereas the most stable configuration for N and O atoms is **cfg2**, in which two octahedral sites are symmetric with vacancy position along [100] direction. It is observed that the binding energy of **cfg2** for C, N and O atom can be obtained by superposition of binding energy for two V-SA complexes, suggesting non-interacting nature of the two SAs (C, N, O) around a vacancy in **cfg2**. The binding energy values of the V-SA_2 complexes are increasing in C<N<O order, which is consistent with the V-SA interaction results (Figure 7.7 (a)). All the interactions among V and two different SAs are tabulated in Table 7.5. The most stable configuration for any two of the C, N, O atoms and the vacancy is **cfg2** and for B atom it is **cfg1**. The binding energy values for different configurations mainly depend on the distance between two SAs and V-SA. All the investigated configurations for each solute atom have positive binding energy, implying the stabilization of the different V-SA_2 complexes.

Table 7.4 Binding energy of two SAs (C, N, B, O) of same identity and a vacancy in bcc Fe. The calculations are done with 54-atom supercell. The column 9, 10, 12 and 13 give the distances between two SAs and vacancy-SA.

Different Configurations	E_{V-C2} (eV)			E_{V-N2}(eV)			E_{V-O2}(eV)	d_{v-SA} (A^o)	d_{SA-SA} (A^o)	E^*_{V-B2}(eV)	d_{B-B} (A^o)	d_{v-B} (A^o)
	This work	Domain[a]	Ohnuma[b]	This work	Domain[a]	Ohnuma[b]						

Cfg^1_{V-SA2}	+1.33	1.24	1.56	+0.53	0.32	0.73	+2.11	1.41	2.0	+0.77	2.41	2.41
Cfg^2_{V-SA2}	+0.94	0.71	1.53	+1.48	1.25	1.83	+3.12	1.41	3.16	+0.67	3.94	2.78
Cfg^3_{V-SA2}	+0.51	0.30		+1.08	0.85		+2.32	2.0	2.83	+0.32	4.83	3.94
Cfg^4_{V-SA2}	+0.49			+0.69			+1.58	3.16	2.83	+0.35	3.94	4.83
Cfg^5_{V-SA2}	+0.51			+0.80			+1.63	3.16	4.0	+0.67	6.23	5.57
Cfg^6_{V-SA2}	+0.63			+0.87			+1.74	3.46	4.24			
Cfg^7_{V-SA2}	+0.47			+0.78			+1.52	4.47	5.1			

[a]Reference [12], [b]Reference [20], *configuration for B case are shown in Figure 7.9(b)

Table 7.5 Binding energy of two different SAs (C, N, B, O) with a vacancy in bcc Fe. The calculations are done with 54-atoms supercell. The column 5, 6, 10 and 11 give the distances between two SAs and vacancy-SA.

Different Configurations	E_{C-N-V} (eV)	E_{C-O-V} (eV)	E_{N-O-V} (eV)	d_{v-SA} (A^o)	d_{SA-SA} (A^o)	E_{B-C-V} (eV)	E_{B-N-V} (eV)	E_{B-O-V} (eV)	d_{v-B}(A^o)	d_{B-B}(A^o)
Cfg^1_{V-SA2}	+0.84	+0.92	+1.25	1.41	2.47	+0.70	+1.08	+1.86	2.47	1.42
Cfg^2_{V-SA2}	+1.22	+1.99	+2.27	1.41	3.16	+0.68	-0.16	+0.67	2.83	2.0
Cfg^3_{V-SA2}	+0.79	+1.20	+1.50	2.0	2.83	+0.13	+0.31	+0.85	4.0	3.49
Cfg^4_{V-SA2}	+0.47	+0.46	+0.73	3.16	2.83	+0.15	+0.32	+0.53	4.94	3.49
Cfg^5_{V-SA2}	+0.54	+0.60	+0.86	3.16	4.0	-0.09	+0.12	+0.53	4.73	3.19
Cfg^6_{V-SA2}	+0.61	+1.39	+0.96	3.46	4.24					
Cfg^7_{V-SA2}	+0.48	+0.48	0.77	4.47	5.1					

(ii) In fcc-Fe

The binding energy among two solute atoms and a vacancy in fcc-Fe systems at different configurations is tabulated in Table 7.6. Interestingly, all SAs (C, N, B, O) exhibit the similar interaction behaviour and have identical minimum energy configuration (**cfg6** from Table 7.6). In stable configuration i.e. **cfg6**, both SAs are positioned at two octahedral sites symmetric with respect to vacancy position along [100] direction. Like in case of bcc-Fe system, here as well, the binding energy of **cfg6** for C, N and O atom (except B atom) can be obtained by superposition of binding energy for two V-SA complexes, suggesting non-interacting nature of the two SAs (C, N, O) around a vacancy in **cfg6**.The interaction of B atom with B or any other SA in presence of the vacancy leads to attraction of B atom towards vacancy as can be seen clearly from charge density plots as well (Figure 7.10 & 7.11). This might be the reason behind the different interaction nature of B atom in fcc-Fe system. We compare the binding energy value at **cfg6** for all SAs and found it to increase in B>O>N>C order. This again follows the same trend as V-SA interaction in fcc-Fe lattice. The negative binding energies associated with all the investigated configurations other than **cfg1** and **cfg6**, represent unstable complexes for all SAs in those configurations. Furthermore, configurations **cfg3**, **cfg4** and **cfg5** have the same binding energy for all the solute atoms even though these configurations differ from each other in terms of solute directions with respect to vacancy and another solute (Figure 7.9 (d)). This result enunciates the isotropic nature of point defect interactions in these configurations in fcc-Fe lattices.

The most important difference in the energies of V-SA$_2$ complexes in bcc and fcc-Fe lattices is that in case of fcc-Fe systems, stabilization energy of the V-SA$_2$ system is less than that of the corresponding V-SA complex. It means that the addition of another solute atom to the V-SA complex destabilizes the system in fcc-Fe. On the other hand, in bcc-Fe systems, as already mentioned, the stabilization energy of the V-SA$_2$ complex is almost double to that of the V-SA complex. This observation again point towards the fact that vacancy trapping ability is stronger in bcc-Fe systems than in fcc-Fe systems.

Table 7.6 Binding energy of two SAs (C, N, B, O) of same and different identity with a vacancy in fcc Fe. The calculations are done with 108-atoms supercell. The column 12 and 13 give the distances between two SAs and vacancy-SA.

Different Configurations	$E_{V\text{-}C2}$ (eV)	$E_{V\text{-}N2}$ (eV)	$E_{V\text{-}B2}$ (eV)	$E_{V\text{-}O2}$ (eV)	$E_{V\text{-}C\text{-}N}$ (eV)	$E_{V\text{-}C\text{-}B}$ (eV)	$E_{V\text{-}C\text{-}O}$ (eV)	$E_{V\text{-}N\text{-}B}$ (eV)	$E_{V\text{-}N\text{-}O}$ (eV)	$E_{V\text{-}B\text{-}O}$ (eV)	$d_{v\text{-}SA}$ (A^{o})	$d_{SA\text{-}SA}$ (A^{o})
$Cfg^{1}_{V\text{-}SA2}$	+0.11	+0.28	+1.89	+0.95	+0.30	+2.08	+1.02	+1.96	+1.02	+1.03	1.72	2.98
$Cfg^{2}_{V\text{-}SA2}$	-0.21	-0.25	-0.09	-0.08	-0.26	+0.01	-0.07	-0.12	-0.04	-0.07	3.85	2.43
$Cfg^{3}_{V\text{-}SA2}$	-0.17	-0.19	-0.09	-0.09	-0.21	+0.04	-0.03	-0.09	-0.01	-0.03	5.16	2.43
$Cfg^{4}_{V\text{-}SA2}$	-0.17	-0.19	-0.09	-0.09	-0.21	+0.04	-0.03	-0.09	-0.01	-0.03	5.16	2.43
$Cfg^{5}_{V\text{-}SA2}$	-0.17	-0.19	-0.09	-0.09	-0.21	+0.04	-0.03	-0.09	-0.01	-0.03	5.16	2.43
$Cfg^{6}_{V\text{-}SA2}$	+0.75	+1.23	+2.50	+2.38	+0.99	+1.75	+1.59	+1.64	+1.81	+2.35	1.84	1.84

We have calculated the differential charge density for the most stable configuration in each complex in bcc as well as in fcc-Fe lattices (Figure 7.10 & 7.11). In bcc-Fe, the $V\text{-}SA_2$ complex in **cfg1**, differential charge density suggests the covalent bond nature with a significantly high electronic charge accumulation between two C-atoms (see Figure 7.12), which is in agreement with previous DFT studies [12,15]. The distance between two C-atoms after relaxation is found to be 1.43Å, which is well within the typical covalent bond length of C-C (1.38-1.48 Å [12]).

This behaviour is not observed in case of N and O atom for the same configuration, which is shown (Figure 7.12) here for N atom. It has been observed (see Table 7.4) that the most stable configuration of the V-C2 complex is the **cfg1** but the same for O and N complex is **cfg2**. The extra stability of the **cfg1** may be attributed to the covalent bond formation between the C-atoms in the V-C2 complexes. No such bond formation has been observed in any other complexes. The differential charge density maps of N and O complexes in **cfg2** are plotted in Figure 7.10 and we found that it is very much similar to the one obtained for V-SA (see Figure 7.8), indicating the absence of interaction between two SAs along [100] direction. However, the covalent bond formation is not observed between two C atoms in any of the configurations in fcc-Fe system (Figure 7.12). There is no covalent bond formation mainly due to the distance between the two C atoms here is (2.7 Å) larger than the typical C-C covalent bond length. In fcc-Fe, all SAs have similar interaction behaviour.

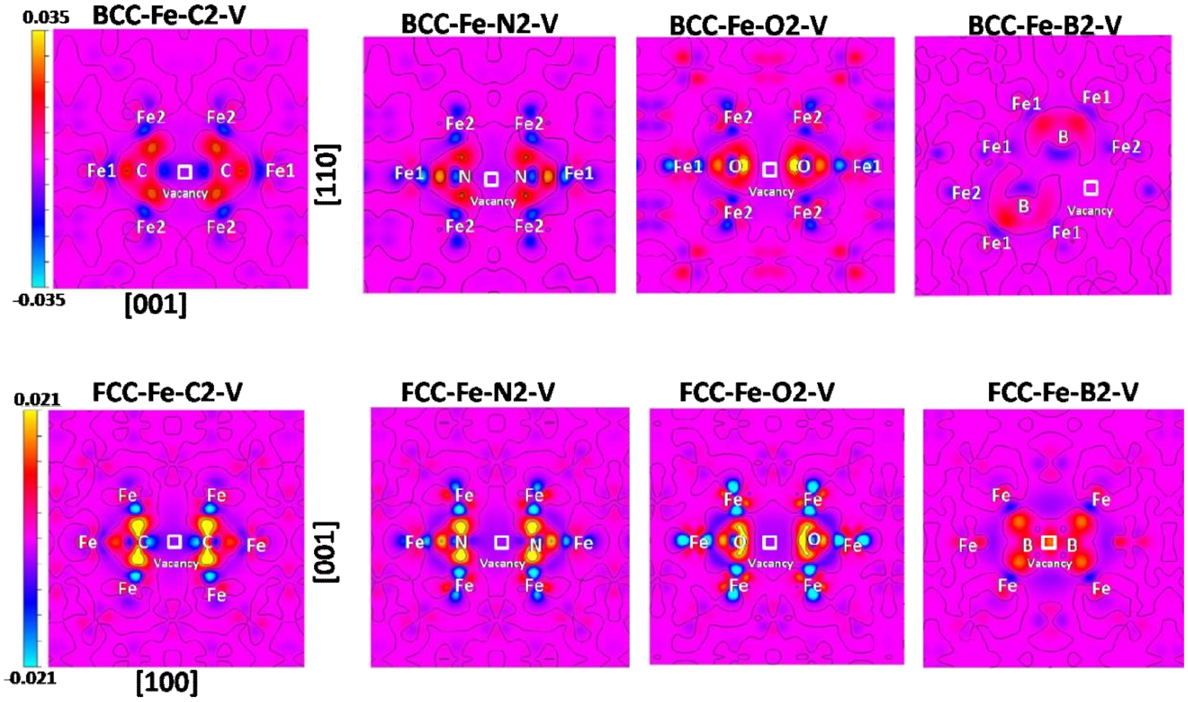

Figure 7.10. The differential charge density distribution for vacancy with two SA atoms in bcc-Fe (cfg2) and fcc-Fe (cfg6) lattice. The plot shows the charge distribution of SA and their nearest neighbour Fe-atom.

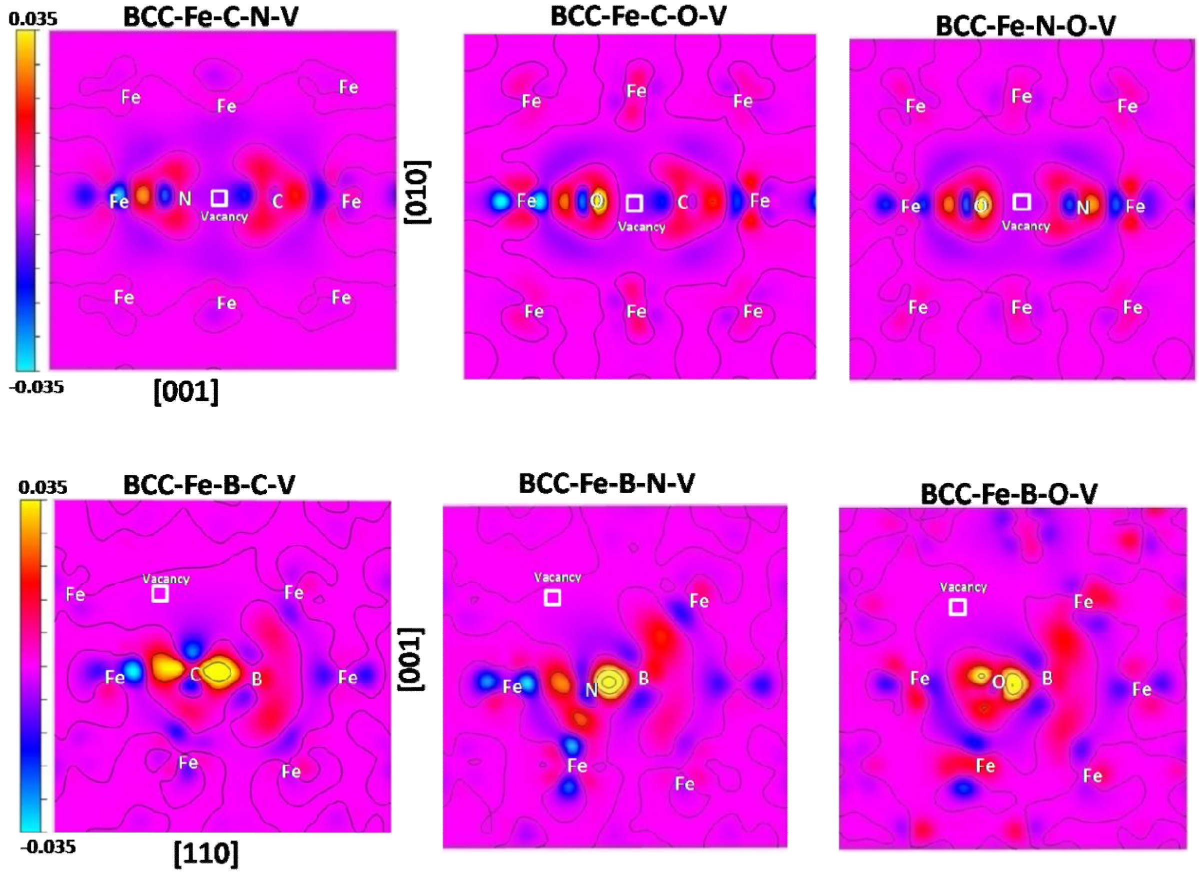

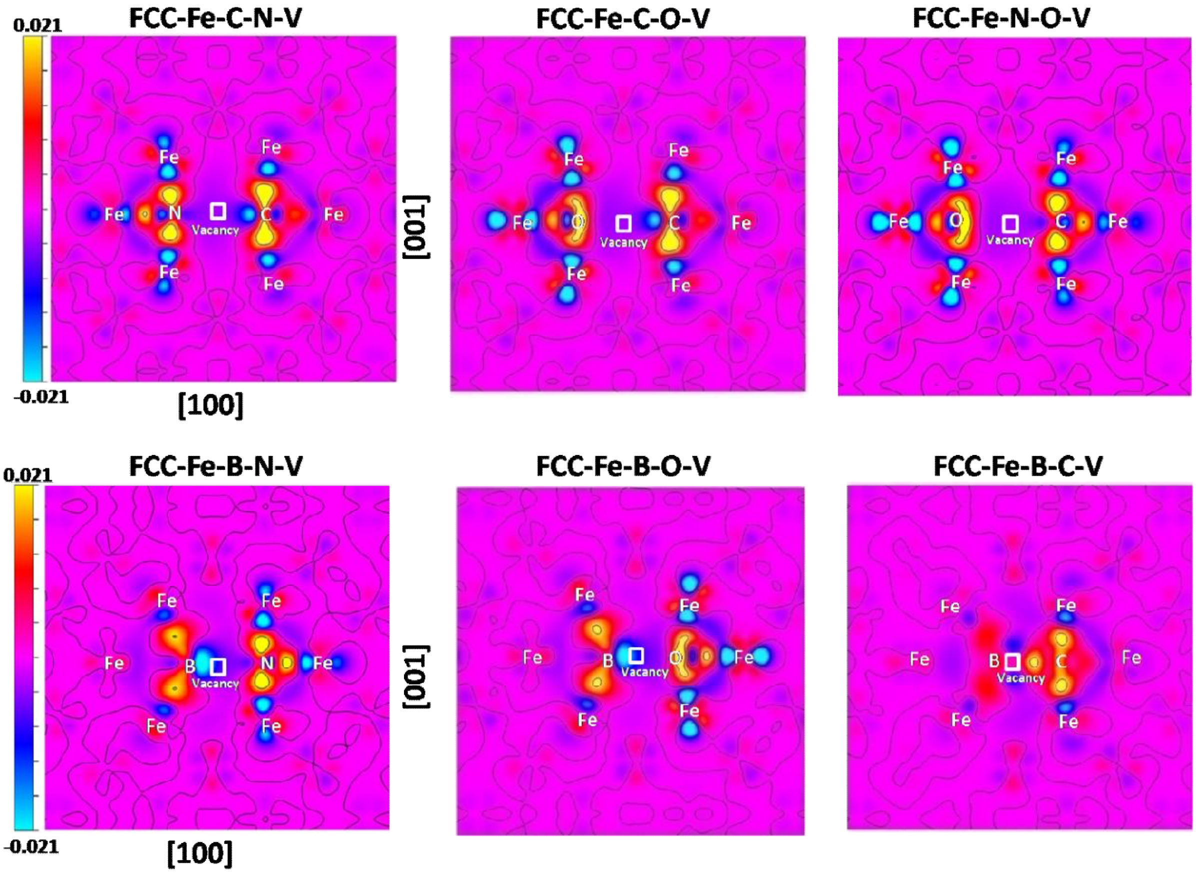

Figure 7.11. The differential charge density distribution for vacancy with two different SA atoms in bcc-Fe (cfg2) and fcc-Fe (cfg6) lattice. The plot shows the charge distribution of SA and their nearest neighbour Fe-atom.

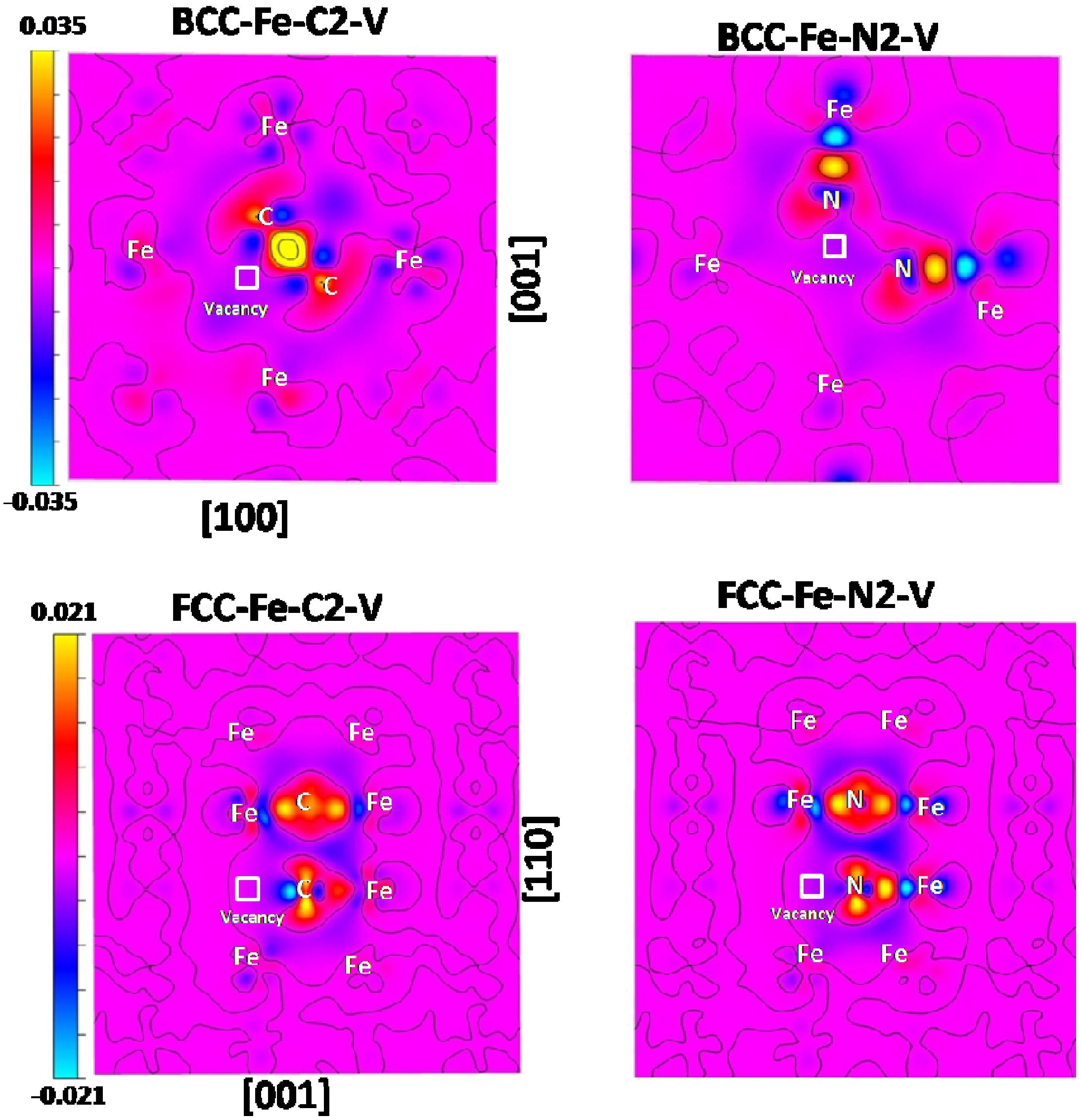

Figure 7.12. The differential charge density distribution for vacancy with two C and N atoms for **cfg1** in both bcc-Fe and fcc-Fe lattice.

7.3.2.4 Interactions of one solute atom – two vacancies

We have determined the interaction among one solute atom and two vacancies at different configurations (Figure 7.9 (f), (g) & (h)) in both the Fe-lattices. The binding energies of all the

SAs with two vacancies at different configurations in both the Fe-lattices are summarized in Table 7.7 & 7.8. In all configurations, mainly V-V distance and V-SA distances are varied.

(i) In bcc-Fe

Calculated binding of the SA-V_2 complex for different SAs is reported in Table 7.7. In all the cases, binding/stabilization energy decreases with increasing SA-V separation. For example, configurations **cfg3** and **cfg4** with SA as C, N and O atoms and configurations **cfg3** and **cgf5** with SA as B atom separated by different V-V separations but same SA-V separations are found to have nearly same binding/stabilization energy. In all these configurations stated above, V-V distance is too large to produce any significant V-V interaction (see Figure 7.14(a) red line). Among all SA-V_2 complexes studied here, O atom forms the most stable complex and C atom forms the least stable one, with the stability order O>B>N>C. It is interesting to note that in all the configurations studied here, binding energy is attractive or stabilizing in nature, indicating stable complex formation.

If the energetics of the SA-V systems (Figure 7.7 (a)) is compared with that of SA-V_2 systems (Table 7.7) it transpires that addition of one more vacancy to SA-V complex increases the stability of the complex. Thus, multiple vacancies can effectively bind to a SA resulting in agglomeration of vacancy-solute clusters.

Table 7.7 Binding energy of single SA (C, N, B, O) with two vacancies in bcc Fe positioned at different configurations.

Different Configurations	$E_{C\text{-}V2}$ (eV)	$E_{N\text{-}V2}$ (eV)	$E_{O\text{-}V2}$ (eV)	$d_{V\text{-}V}$ (A^o)	$d_{V\text{-}SA}$ (A^o)	Different Configurations	$E_{B\text{-}V2}$ (eV)	$d_{V\text{-}V}$ (A^o)	$d_{V\text{-}B}$ (A^o)
$Cfg^1_{SA\text{-}V2}$	+0.16	+0.36	+1.19	2.83	2.0	$Cfg^1_{SA\text{-}V2}$	+0.77	2.45	2.45
$Cfg^2_{SA\text{-}V2}$	+0.32	+0.76	+1.89	2.45	1.41	$Cfg^2_{SA\text{-}V2}$	+0.65	4.0	2.83
$Cfg^3_{SA\text{-}V2}$	+0.12	+0.34	+0.81	4.0	3.46	$Cfg^3_{SA\text{-}V2}$	+0.32	4.9	4.0
$Cfg^4_{SA\text{-}V2}$	+0.12	+0.31	+0.82	4.9	3.46	$Cfg^4_{SA\text{-}V2}$	+0.33	4.0	4.9
						$Cfg^5_{SA\text{-}V2}$	+0.31	6.33	4.0

(ii) In fcc-Fe

The binding/stabilization energy of the SA-V_2 complexes (SA=B, C, N, O) in fcc-Fe lattice has been reported in Table 7.8. In fcc-Fe systems, stabilization energy of the SA-V_2 complex of any solute atom is more than that of the corresponding SA-V system (see Figure 7.7 (d)), thus signifying that multiple vacancies can bind with the solute atom more effectively leading to multi-vacancy-SA clusters. The relative stability order for different SAs for the SA-V_2 complex follows the same order as for SA-V complex, i.e. B>O>N>C.

For all the SAs, **cfg1** is found to be the most stable configuration among all the configurations studied here. It is to note that in the configuration **cfg1**, the distance between the two vacancies is around 2.43Å and it can be seen later in Figure 7.14(a) that at this distance, V-V interaction is quite attractive. Therefore the extra stability pertaining to **cfg1** is a consequence of strongly attractive V-V interaction at short range (see first point in Figure 7.14(a)). It is also to note that **cfg2** and **cfg4** configurations have almost the same binding/stabilization energy, but in case of **cfg4**, two vacancies are aligned on the opposite sides of the SA along [111] direction, thus forming a dumbbell-like structure and it is not so in case of **cfg2**. Interestingly, **cfg3** and **cfg5** configurations have the same V-V and SA-V distances but having different configuration directions and they have the same binding energy. These facts suggest that the nature of interaction of solute atoms with vacancies in fcc-Fe is isotropic in nature.

Table 7.8 Binding energy of single SA (C, N, B, O) with two vacancies in fcc-Fe positioned at different configurations.

Different Configurations	$E_{C\text{-}V2}$ (eV)	$E_{N\text{-}V2}$ (eV)	$E_{B\text{-}V2}$ (eV)	$E_{O\text{-}V2}$ (eV)	$d_{V\text{-}V}$ (A^o)	$d_{V\text{-}SA}$ (A^o)
$Cfg^1_{SA\text{-}V2}$	+0.62	+0.89	+2.26	+1.54	2.43	1.72
$Cfg^2_{SA\text{-}V2}$	+0.15	+0.24	+0.04	+0.29	3.44	2.98
$Cfg^3_{SA\text{-}V2}$	+0.39	+0.71	+2.06	+1.33	4.22	1.72
$Cfg^4_{SA\text{-}V2}$	+0.15	+0.25	+0.06	+0.29	5.96	2.98
$Cfg^5_{SA\text{-}V2}$	+0.39	+0.71	+2.06	+1.33	4.22	1.72

The differential charge density for most stable configuration in both the Fe-lattices is shown in Figure 7.13. It is observed that the charge distribution between SA and vacancy is different for different SA which explains the change in binding energy of different SA.

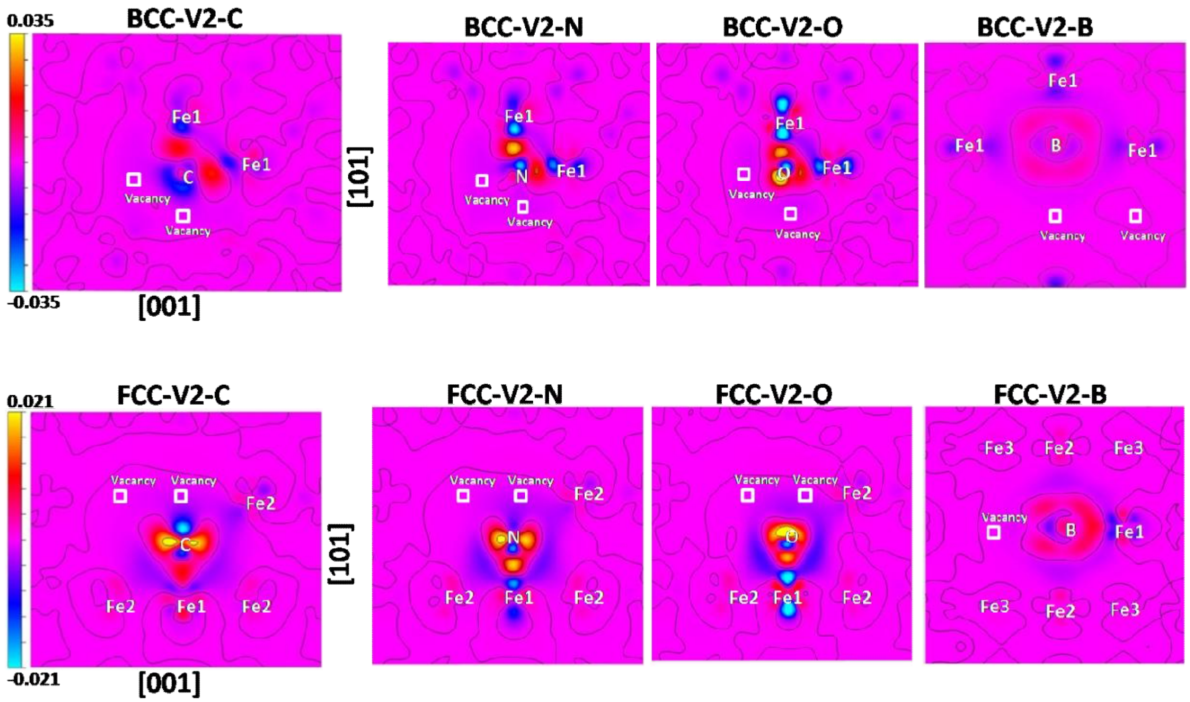

Figure 7.13. The differential charge density distribution (in eV/Å^3) for two vacancies with single SA atom in bcc and fcc-Fe lattices. The plot shows the charge distribution of SA and their nearest neighbor Fe-atoms.

7.3.2.5 Four SAs interactions with each other

We have calculated the interaction among all SAs (C, N, B, O) in both the Fe-lattices (Table 7.9) at different configurations as shown in Figure 7.9 (i) and (j). In bcc-Fe, there are a few stable configurations mainly due to attractive interaction (which may be a consequence of substitutional occupancy of the B atom) of B with other SAs (see Figure 7.5(c)), but in fcc-Fe, as all the solute atoms are occupying interstitial positions, the system becomes completely unstable for all the investigated configurations as reported in Table 7.9. The huge strain generated in the fcc system with the presence of four different interstitial SAs can be a plausible rationale behind such instability in the systems.

Table 7.9 Binding energy of four different SAs (C, N, B, O) in bcc-Fe and fcc-Fe lattices with different configurations.

BCC Fe				FCC Fe			
Different Configurations	$E_{\text{C-N-B-O}}$ (eV)	$d_{\text{N-B}}$ (A^{o})	$d_{\text{N-C}}$ (A^{o})	Different Configurations	$E_{\text{C-N-B-O}}$ (eV)	$d_{\text{N-B}}$ (A^{o})	$d_{\text{N-C}}$ (A^{o})
$Cfg^{1}_{\text{C-N-B-O}}$	+0.20	2.0	2.38	$Cfg^{1}_{\text{C-N-B-O}}$	-2.31	5.44	2.43
$Cfg^{2}_{\text{C-N-B-O}}$	+0.86	1.42	2.47	$Cfg^{2}_{\text{C-N-B-O}}$	-2.22	2.43	5.44
$Cfg^{3}_{\text{C-N-B-O}}$	-0.03	1.41	3.16	$Cfg^{3}_{\text{C-N-B-O}}$	-2.31	5.44	2.43
$Cfg^{4}_{\text{C-N-B-O}}$	-1.04	2.01	4.06	$Cfg^{4}_{\text{C-N-B-O}}$	-2.22	2.43	5.44
$Cfg^{5}_{\text{C-N-B-O}}$	+0.90	3.63	5.01	$Cfg^{5}_{\text{C-N-B-O}}$	-2.32	7.31	2.43
				$Cfg^{6}_{\text{C-N-B-O}}$	-2.29	2.43	7.31
				$Cfg^{7}_{\text{C-N-B-O}}$	-1.93	4.22	6.44
				$Cfg^{8}_{\text{C-N-B-O}}$	-1.94	6.44	4.22

7.3.2.6 Vacancy-vacancy interaction

Vacancies have a predominant influence on the materials properties because of their important role in atomic diffusion. During irradiation, besides mono-vacancies, vacancy clusters also form which influence the structural properties of materials. This motivates our investigation for vacancy-vacancy interaction in both bcc-Fe and fcc-Fe at different configurations (Figure 7.14 (b) & (c)). The corresponding binding energies for bcc and fcc systems are shown in Figure 7.14

(a). In bcc-Fe, 1NN and 2NN vacancy pairs are found to have attractive interaction, implying that the vacancy upto 2NN can make clusters in bcc-Fe. The peak at 2NN neighbour is consistent with the di-vacancy binding energy being larger for 2NN than for 1NN (see Table 7.1). This result is in well agreement with other reported simulation result [21]. In contrast, in fcc-Fe, only 1NN vacancy pair is observed to have strong attractive interactions and 3NN showing some weak attractive interaction, whereas all other investigated configurations are found to have either repulsive or negligible interaction. It can be concluded that vacancy cluster formation is more probable in bcc-Fe as vacancy can bind 1NN as well as 2NN vacancy as compared to that in fcc-Fe, where only 1NN vacancy will take part significantly in the cluster formation process. This argument is consistent with the experimental result [22], in which it is demonstrated that bcc iron has greater tendency to form vacancy clusters. In both Fe-lattices, the binding energy becomes negligible with increasing inter-vacancy distance.

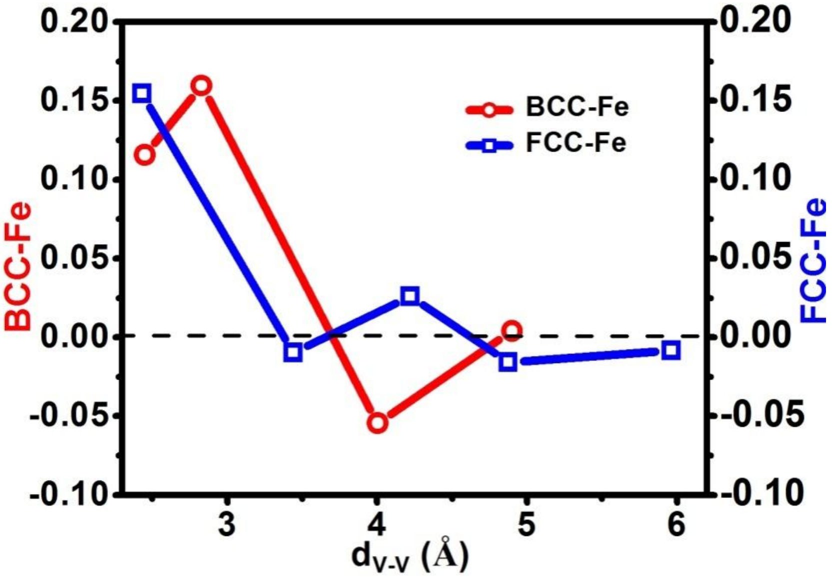

(a)

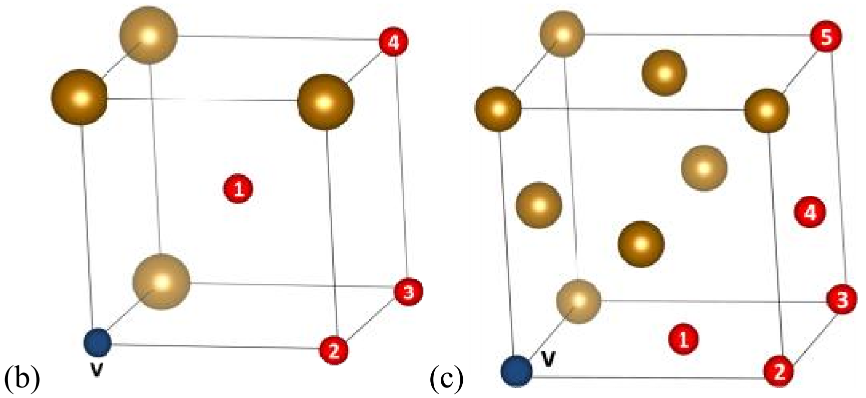

Figure 7.14. (a) Vacancy-vacancy binding energy with distance in bcc-Fe and fcc-Fe lattices and the corresponding configurations are displayed in (b) and (c) respectively.

7.3.2.7 Vacancy-SA$_m$ interaction

The binding energy for V-SA$_m$ (SA = C, N, B, O) is investigated for *m* value upto 5 in both Fe-lattices. We limited our investigations to clusters where solute atoms are either at 1NN or 2NN to the vacancy in order to consider compact clusters. The corresponding binding energies are displayed in Figure 7.15. In bcc-Fe (see Figure 7.15(a)), we noticed that single vacancy binds the SAs upto *m*=3 to 4 independent of solute identity. In case of O and B atoms, system is always stable upto m=5, whereas it becomes unstable for C and N beyond *m*=4.

In fcc-Fe, the binding energy for all the solute atoms is monotonically decreasing with increasing *m*. For B and O atoms, clusters containing four to five solute atoms are stable. Upto *m*=2, the strength of binding energy is increasing in the order C<N<O<B, which is already explained (see section 7.3.2.3) with the help of atom radii with B as exception here as well. Interestingly, the binding energy of C is less than that of N when it is attractive, whereas after *m*=2, magnitude of

C clusters interaction energy overrides that of N clusters and becomes less repulsive. In both the lattices, the interaction of the clusters containing N are most repulsive here as well, consistent with the previous (solute-solute interaction, see Figures 7.5(a) and 7.6(a)) observations. It is interesting to note that the interaction energy of the solute atom clusters with 4 atoms as shown in Table 7.9 are unstable in all possible combinations for the fcc-Fe, but in the present case introduction of one vacancy in such cluster makes the cluster stable or near stable.

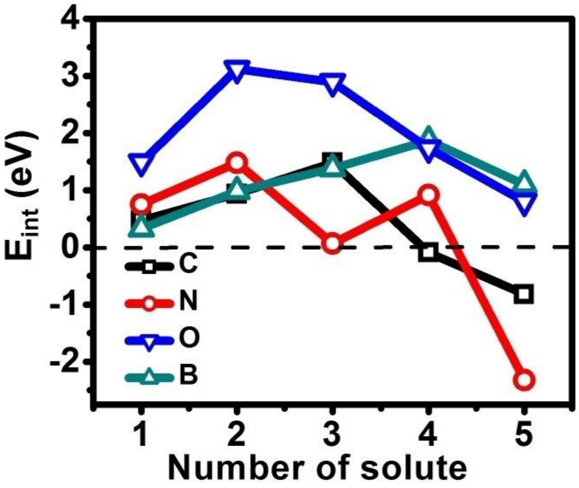

(a)

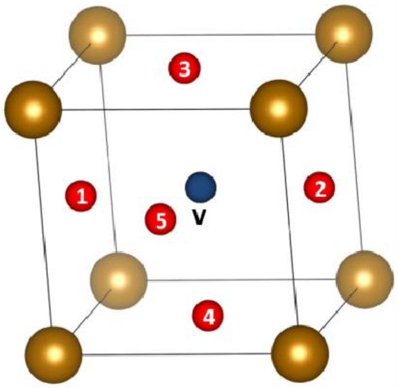

(b)

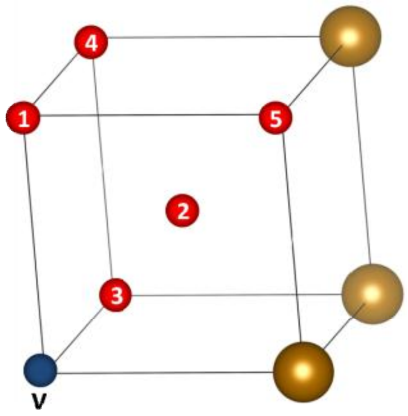

(c)

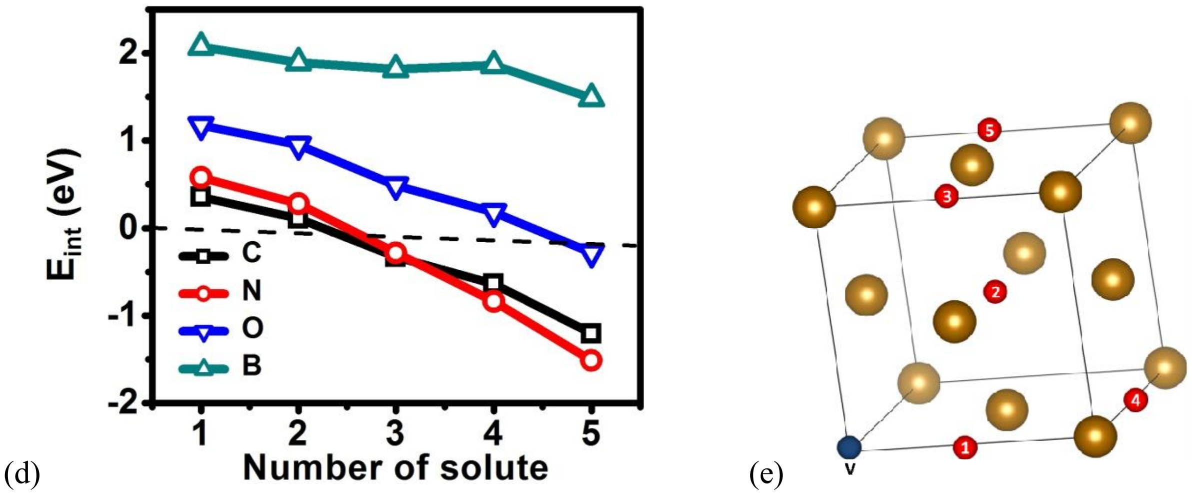

Figure 7.15. Binding energy of V-SA$_m$ clusters for SA= C, N, B and O for m =1-5 in (a) bcc-Fe and (d) fcc-Fe lattice. The investigated configurations are for (b) V-SA$_m$ (SA= C, N, O) in bcc lattice (c) V-B$_m$ in bcc lattice and (e) V-SA$_m$ (SA= C, N, B, O) in fcc lattice.

7.4 Summary

In summary, we present a comparative analysis of the results obtained from extensive first-principle calculations on the interaction of vacancies and solute atoms (C, N, B, O) in bcc-Fe and fcc-Fe lattices. The substitutional site is more favourable for B atom in bcc-Fe while the most preferred site in fcc-Fe is octahedral interstitial site. However, the difference in energy of B atom in octahedral and substitutional sites in bcc-Fe is close to thermal energy (k_BT) at room temperature. Our results suggest that the stability of all SAs is influenced more by the geometrical factor than by the chemical nature. From the calculated interaction energy of the solute atom with self and other SAs, we find the general tendency that B atom tends to bind other SAs in bcc-Fe, while it repels in fcc-Fe. This diverse interaction behaviour is explained on the basis of its different stable configuration in these two Fe-lattices. For all other SAs (C, N, O), nature of interaction among SAs is repulsive in both the Fe-lattices. Based on our results, vacancy always binds all solute atoms in both the Fe-lattices. Moreover, a similarity is observed between interaction behaviour of B atom and vacancy with other point defects in bcc-Fe, while no such resemblance is observed in fcc-Fe. It is also found that the trapping ability of vacancy is stronger in bcc-Fe as compared to fcc-Fe lattice. In case of two solute atoms in presence of a vacancy, it is found that two C atoms form a covalent bond in bcc-Fe, but not in fcc-Fe. It is found that the interaction of four solute atoms in the fcc-Fe lattice is repulsive in nature irrespective of the configuration considered, but introduction of a vacancy in such systems stabilizes it. The nature of bonding and charge delocalization have been analysed in detail in all the cases from differential charge density plots.

References

[1] L. De Schepper, D. Segers, L. Dorikens-Vanpraet, M. Dorikens, G. Knuyt, L. M. Stals, and P. Moser, Physical Review B **27**, 5257 (1983).

[2] C. Domain and C. S. Becquart, Physical Review B **65**, 024103 (2001).

[3] Y. Tateyama and T. Ohno, Physical Review B **67**, 174105 (2003).

[4] C.-C. Fu, F. Willaime, and P. Ordejón, Physical Review Letters **92**, 175503 (2004).

[5] S. M. Kim and W. J. L. Buyers, Journal of Physics F: Metal Physics **8**, L103 (1978).

[6] I. Seki and K. Nagata, ISIJ International **45**, 1789 (2005).

[7] A. F. Bialon, T. Hammerschmidt, and R. Drautz, Physical Review B **87**, 104109 (2013).

[8] J. A. Rayne and B. S. Chandrasekhar, Physical Review **122**, 1714 (1961).

[9] S. Ahlawat, K. Srinivasu, A. Biswas, and N. Choudhury, Computational Materials Science **170**, 109167 (2019).

[10] D. J. Hepburn, E. MacLeod, and G. J. Ackland, Physical Review B **92**, 014110 (2015).

[11] E. Clementi, D. L. Raimondi, and W. P. Reinhardt, The Journal of Chemical Physics **47**, 1300 (1967).

[12] C. Domain, C. S. Becquart, and J. Foct, Physical Review B **69**, 144112 (2004).

[13] S. S. Baik, B. I. Min, S. K. Kwon, and Y. M. Koo, Physical Review B **81**, 144101 (2010).

[14] D. H. R. Fors and G. Wahnström, Physical Review B **77**, 132102 (2008).

[15] C. Barouh, T. Schuler, C.-C. Fu, and M. Nastar, Physical Review B **90**, 054112 (2014).

[16] G. K. Williamson and R. E. Smallman, Acta Crystallographica **6**, 361 (1953).

[17] D. E. Jiang and E. A. Carter, Physical Review B **67**, 214103 (2003).

[18] T. He, Y. Jiang, R. Zhou, and J. Feng, RSC Advances **6**, 45250 (2016).

[19] G. Dubben, M. N. Chandrasekharaiah, and B. H. Kolster, Journal of Materials Science **27**, 3192 (1992).

[20] T. Ohnuma, N. Soneda, and M. Iwasawa, Acta Materialia **57**, 5947 (2009).

[21] R. E. Stoller, MRS Proceedings **540**, 679, 679 (1998).

[22] K. Dawi, C. W. He, M. F. Barthe, P. Desgardin, and A. Volgin, Journal of Physics: Conference Series **505**, 012007 (2014).

Appendix I

Basics of small angle scattering

1. **Guinier Approximation:** For a system of randomly oriented particles of any arbitrary shape, the scattering profile at low-q can be approximated as follows [1]:

   $$I(q) \approx I(0)\, e^{\frac{-q^2 R_g{}^2}{3}}$$

   Where, I(0) is an intensity at zero scattering angle (q=0) and R_g is the radius of gyration of the particle and gives an intuitive measure for the spatial extension of the particle. For monodisperse spherical particles with radius R, $R_g = R\sqrt{\frac{3}{5}}$.

   The plot of log(I(q)) vs q^2, called the Guinier plot, shows a straight line in low-q region. The slope of the linear part of the Guinier plot is then equal to $-R_g{}^2/3$, which gives the radius of gyration of the particle. Therefore, it is possible to determine the mean size from the scattering data at q →0 limit without having information about the shape of the object. The Guinier approximation offers the simplest, most straightforward and fairly reliable approximation to SANS for small enough q values.

2. **Porod approximation:** It states that P(q), the form factor for inhomogeneity with sharp boundary and uniform scattering length density at large value of q can be approximated as [1]

   $$P(q) \sim \frac{2\pi S}{V}\frac{1}{q^4}$$

Where, S and V are surface area and volume of inhomogeneity respectively. I(q) in such a case is represented as follows:

$$\mathrm{Lt}_{\,q\to\infty}\, \mathrm{I(q)} = \frac{K_p}{q^4}$$

Here, K_p is the Porod constant. The plot between $I(q)q^4$ vs. q give flat plateau at higher-q values and that will give information about the Porod constant. Subsequently, it can be used to obtain specific surface area to volume ratio (S/V) of the inhomogeneity using following expression:

$$\frac{S}{V} = \pi \frac{Lt_{q\to\infty} I(q)q^4}{\int_0^\infty I(q)q^2 dq}$$

The term $\int_0^\infty I(q)q^2 dq$ is known as scattering invariant and is related to the inhomogeneity volume fraction φ as

$$\int_0^\infty I(q)q^2 dq = 2\pi^2 \Delta\rho^2 \varphi(1-\varphi)$$

We have estimated volume fraction using the above expression in chapter 4.

3. **Data reduction and analysis:** A number of correction procedures are performed once the scattered signal is collected at the 2D detector. The position of each pixel in the detector corresponds to a scattering angle 2θ or scattering vector *q,* by taking into account the wavelength, pixel size and sample-to-detector distance. If the image obtained at the detector is azimuthally isotropic, radial averaging of the 2D image is performed to obtain 1D scattering profile. The direct beam signal is subtracted from the measured scattered signal from sample. Subsquently, scattered signal from solutionized sample is also subtracted from the signal from thermal aged sample in order to study the effect of thermal aging. The scattered contribution can be written as follows:

$$I_{sample}^{corrected} = I_{sample} - T * I_{direct}$$

here, I_{sample} is scattered signal from sample, T is transmission and I_{direct} is direct beam signal.

$$I_{sample}^{final} = I_{sample}^{corrected} - I_{solutionized}^{corrected}$$

Appendix II

Density functional theory calculations

1. Reason for choosing GGA (PBE) functional: Based on the success of the GGA and PAW-PBE functional and potential in reproducing many properties of the Fe-systems as available in the literature, we have chosen them for our work. In addition, we have verified our calculations and the related results are given in chapter 5. It is shown (see the Table below) that the lattice parameter, cohesive energy, vacancy formation energy and bulk modulus calculated using the combination of the above mentioned functional and potential are in very good agreement with the respective experimental values.

Table A: Influence of different exchange-correlation functional on the properties of bcc-Fe.

	LDA [2]	**PBE [2]**	**PW91 [2]**	**PBEsol [2]**	**revTPSS [2]**	**Experiment**
Lattice parameter (Å)	**2.75**	**2.83**	**2.83**	**2.79**	**2.80**	**2.87 [3]**
Cohesive energy (eV)	**6.53**	**4.87**	**5.20**	**5.88**	**5.49**	**4.28 [4]**
Bulk Modulus (GPa)	**251**	**188**	**188**	**221**	**213**	**170 [5]**
Vacancy formation energy (eV)	**2.3**	**2.2**	**2.14**	**2.47**	**2.64**	**2.0±0.2 [6]**

1. Difference between Bader charge and differential charge density: Differential charge density distribution ($\Delta\rho$) for a system AB can be calculated as

$$\Delta\rho = \rho_{AB} - \rho_A - \rho_B$$

Here, ρ_i (i=A, B, AB) is the charge density profile of the system *i*.

This distribution gives us qualitative information about charge transfer in the studied system as it is obtained from the relative difference in ρ. The relative change in electronic density in a composite AB system relative to pure A and B systems tells us about the more or less accumulation of electrons at a specified site in the AB system relative to the same in the isolated systems.

On the other hand, Bader charge is based on the principle of defining boundary of an atom in a molecule. The boundary is defined by the zero flux surface between any two adjacent atoms in a molecule, where the zero flux surface is defined as the 2-D surface on which the charge density perpendicular to the surface is a minimum. The charge enclosed within the Bader volume (as obtained by integrating the charge density profile within that volume) is a good approximation of the total electronic charge on an atom in a molecule and thereby it can clearly depict the charge transfer from/to that atom. Thus, in some way it is a quantitative measure of the quantity of charge on an atom in a system.

Reference:

1. A. Guinier and G. Fournet, Small angle scattering of X-rays (Wiley, New York, 1955).

2. B. Medasani, M. Haranczyk, A. Canning and M. Asta; Computational Material Science 101 (2015), 96-107

3. N.W. Ashcroft, M.N.D., International Union of Crystallography, Chester, England, 1987.

4. C. Kittel, Introduction to Solid State Physics, eighth ed., John Wiley & Sons, Inc., Hoboken, J, 2005.

5. A. James, M. Lord, Macmillan's Chemical and Physical Data, Macmillan, London, UK, 1992.

6. De Schepper, Physical Review B, **27**(9) (1983), 5257-5269.

Thesis Highlight

Name of Student: Sarita **Enrolment NO.:** PHYS01201604002

Name of the CI/OCC: BARC, Mumbai

Thesis Title: Computational and experimental studies on the damage response of ferritic and austenitic steels under extreme conditions

Discipline: Physical Sciences **Sub-area of discipline:** Radiation Damage in Steels

Date of Viva-Voce: 14/04/2021

Both ferritic and austenitic steels are primarily used as structural material for different components in nuclear reactors. Ferritic steels are mainly used for reactor pressure vessels (RPV) in nuclear reactors owing to their good mechanical properties at elevated reactor operating temperatures. Austenitic stainless steels are used widely in internal structures of pressurized water reactors. Both these materials are subjected to high irradiation and high temperature during reactor operation. Such an exposure to high radiation results in deterioration of mechanical properties of the materials; limiting the service conditions and lifetime of the components.Using both experimental and theoretical techniques, we have studied the damages and microstructural changes produced in ferritic and austenitic steels induced by high temperature and irradiation.

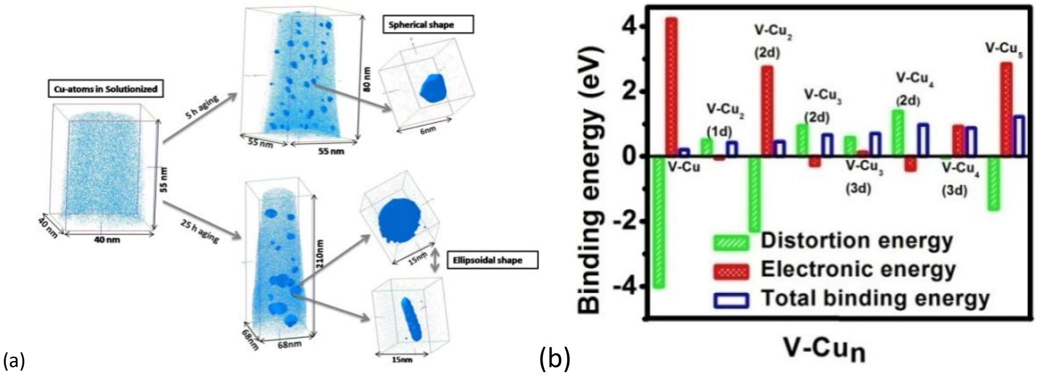

Figure 1: (a) Morphololological transformation of CRPs in thermally aged Fe-Cu alloy (b) Decomposition of binding energy into electronic and distortion energy contributions

The presence of Cu-rich precipitates (CRPs) in binary Fe-Cu alloy is directly observed using atom probe tomography (Fig. 1(a)).The APT analysis has not only shown the formation of CRPs in the irradiated materials, but also has demonstratedthat the CRPs undergo morphological transformation from spherical to ellipsoid with a significant change in its aspect ratio (Fig. 1(a)), an effect known to be associated with the 9R-3R structural transition of the precipitates. The SANS analysis could successfully detect the signature of this morphological transformation in the scattering data, something that has been accomplished for the first time.Moreover, In order to find out the origin of formation of the CRPs in the Fe-Cu alloys, we have usedfirst principle density functional theory (DFT) calculations within the well known PBE-GGA approximation. The attractive interactions in cases of Cu-Cu and V-Cu complexes, as predicted by the DFT calculations, are likely to be the main cause of formation of Cu-clusters in steels. One of the novelties of this investigation is the analysis of the origin of the binding energy (BE) in vacancy-solute complexes by decomposing the BE into electronic and distortion energy contributions (Fig. 1(b)). We have also studied the effect of small solute atoms in both bcc- and fcc-Fe lattices on BE using DFT calculations. Furthermore, the evolution of crystal structure and microstructure in heavy ion (Ag and Au) irradiated SS316 is investigated. Both, the extent of damage as well as the identity of ions are found to affect the nature of radiation-induced phase transformation in this steel.